DTU Fotonik
Department of Photonics Engineering

DTU

Optical Simulations in an Open Geometry Using the Eigenmode Expansion Technique

Bachelor Thesis

Thomas Christensen
Jakob Rosenkrantz de Lasson

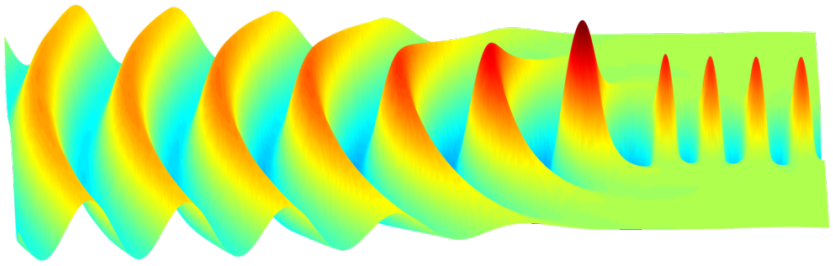

Supervisors:	Niels Gregersen, DTU Fotonik Torben Roland Nielsen, DTU Fotonik
Submission Date:	25 June 2010
Revised Version:	Revised on 16 January 2011

The report was typeset using pdfLaTeX and the memoir class.
Most sketches and illustrations were created using TikZ.
Numerical calculations and graphical plots of data were performed using MATLAB.

Abstract

The field of quantum information technology is receiving significant attention these years, and research concerning the development of single-photon sources plays a central role in this field. These sources may be produced using optical microcavities containing e.g. quantum dots, and knowledge and understanding of these microcavities are hence essential. In that context, accurate and reliable theoretical models for the optical microcavities are requested.

This thesis presents and analyzes two approaches for simulating the electric field in a slab structure, considering only TE-waves. The two methods are used to compute the electric field in different optical environments as well as the normalized spontaneous emission rate. The first and simplest approach is that of a closed geometry where the electric field is assumed to vanish outside a solution domain of finite dimensions. The second and mathematically more challenging approach is an open geometry where the solution domain is given infinite dimensions. For both approaches, the Helmholtz equation for the electric field is solved using a semianalytical approach, and the resulting orthogonal eigenmodes are used to express the electric field throughout the solution domains, using the eigenmode expansion technique. The theoretical results are investigated numerically in MATLAB.

For the closed geometry approach, the electric field is expanded on the eigenmodes using the scattering matrix formalism, and the resulting field profiles are demonstrated to suffer from parasitic reflections. The appertaining calculations of the normalized spontaneous emission rate are shown to be critically dependent on the size of the solution domain, and thus cannot be determined accurately using the closed geometry approach.

An open geometry formalism is established for a uniform layer and a waveguide layer. Through this, the normalized spontaneous emission rate is computed in a single-layer geometry, and contrary to the closed geometry an accurate value is obtained. Further, the formalism is expanded to consider a two-layered open geometry, specifically by considering illumination of the structure with a guided or a radiation mode. In the case of illumination by a guided mode, the field profile is produced and does not suffer from parasitic reflections. For illumination by a radiation mode, the reflection and transmission coefficients do not converge, an no field profile is produced. Finally, an outline for the calculation of the normalized spontaneous emission rate in open geometries of multiple layers is presented.

Preface

This thesis is submitted in partial and final fulfilment of the requirements for a Danish bachelor's degree in Physics and Nanotechnology at the Technical University of Denmark, DTU. The work detailed in this thesis has been carried out in collaboration with DTU Fotonik, under the competent guidance and supervision of Assistant Professor Niels Gregersen and Assistant Professor Torben Roland Nielsen to whom we are indebted for their patience, advice and assistance throughout the project.

The thesis is the result of work conducted in the period from the beginning of February 2010 to the end of June 2010, and constitutes a total of 15 ECTS for each of the authors distributed over the entire period.

Thomas Christensen

Jakob Rosenkrantz de Lasson

Technical University of Denmark, Kgs. Lyngby
25 June 2010

Contents

List of Figures

Chapter 1

Introduction

The research area of optical microcavities is currently receiving significant interest [Vahala], and optical microcavities already diffuse into current applied technology, e.g. in CD, DVD and Blu-ray players. One of the most exciting new prospects introduced by microcavities is the possibility of producing viable and effective single-photon sources. Development of such sources is a prerequisite for practical implementation of quantum information technology [Claudon] and presents a major challenge in integrated optics. In this context, the Purcell effect [Purcell] that describes the decrease or enhancement of the spontaneous emission rate of a quantum emitter [Vahala] is of great importance. Specifically, the Purcell enhancement factor, termed the normalized spontaneous emission rate throughout this report, is of significant interest in the study of micropillar cavities whose basic structure is illustrated in Fig. 1.1(a). A scanning electron microscope image of a micropillar is shown in Fig. 1.1(b).

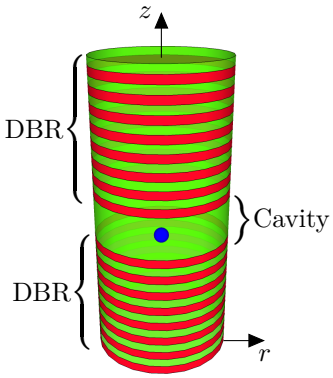

(a) Three dimensional sketch of a micropillar. A quantum dot is embedded in the cavity region and is indicated as a blue sphere. The two distributed bragg reflectors (DBRs) confine the field emitted from the quantum dot to the cavity region. The upper and lower DBRs are adjusted such that light emission is directed primarily along the positive z-direction. Layers of different refractive indices are assigned different colors (red and green).

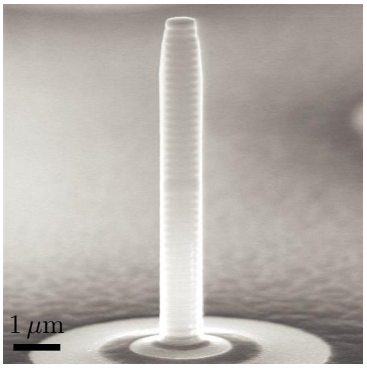

(b) Scanning electron microscope image of a micropillar of diameter $1\,\mu$m [Reithmaier].

Figure 1.1 Micropillar design of a microcavity.

The normalized spontaneous emission rate can conveniently be determined by computation of the normalized power emitted from a current source [Novotny]. This project is concerned with obtaining the normalized spontaneous emission rate by application of this correlation. The power emitted from such a dipole current source depends critically on the electric field due to the dipole and on the surrounding optical environment. By developing accurate modeling tools for determination of the electric field in optical geometries, this allows for determination of the normalized spontaneous emission rate. The specific aim of this thesis is to analyze and compare two different modeling approaches, presented shortly, that allow determination of the optical fields and the normalized spontaneous emission rate.

Different types of electromagnetic waves may exist in the structures to be studied, namely transverse electric and transverse magnetic, and in this thesis only the transverse electric waves are treated. The geometry studied in this project is a that of a slab structure as it represents a mathematically manageable problem and therefore provides a good basis for the development of modeling tools. Specifically, slab structures allow simplification of the otherwise three-dimensional problem to a simpler two-dimensional problem. The reduction to a two-dimensional problem is attained by assuming that the structure is uniform and large of extent along the y-axis, and an example of such a slab structure is depicted in Fig. 1.2. Because the material is assumed uniform along y, the y-eigenmodes of the electric field become orthogonal, and consequently an arbitrary y-eigenmode will not couple to other y-eigenmodes. Hence, the characterization of the electric field in a slab structure can be satisfactorily performed by studying the eigenmodes along the x- and z-directions. Furthermore, the assumption of a large extent in the y-direction induces that the y-propagation constants are negligible, meaning that only the x- and z-propagation constants need be taken into consideration.

From the above discussion, the study of slab structures is essentially a two dimensional problem and hence does not represent most actual physical devices currently under experimental investigation. However, measurements of the spontaneous emission rate in one dimensional Bragg gratings illustrate that slab structures can be used to obtain significant enhancement of the spontaneous emission rate [Tocci]. Furthermore, the slab approach is justified by its usefulness as a frame of reference for a proof of concept: If successful results are obtained for modeling of slab structures, inclusion of more realistic structures, such as cylindrically symmetrical structures, is merely a matter of applying the same principles to a mathematically more extensive problem.

To evaluate the electric field in a given structure, different and well-established modeling techniques exist, including the finite-difference time-domain method, the finite element method and the Green's function method. In this thesis, the electric field is determined using the eigenmode expansion technique in which the eigenmodes along x and z are determined to obtain a basis upon which the full field can be expanded. Specifically, a semi-analytical approach where the eigenmodes are expressed in their analytical form is used. The only approximation in obtaining eigenmodes by use of this approach involves the determination of propagation constants by use of a numerical root finding algorithm and the evaluation of field coefficients by numerical computation of the kernel of a matrix. The use of these semi-analytical eigenmodes prompts a memory-efficient and highly accurate method [Gregersen3, Chapter 3].

Two different approaches, namely that of a closed geometry and that of an open geometry, will be pursued. Calculations in closed geometries are well-studied and their inclusion in this project serves to introduce many of the principles necessary to develop a formalism in the open geometry. Likewise, the closed geometry serves as a comparative

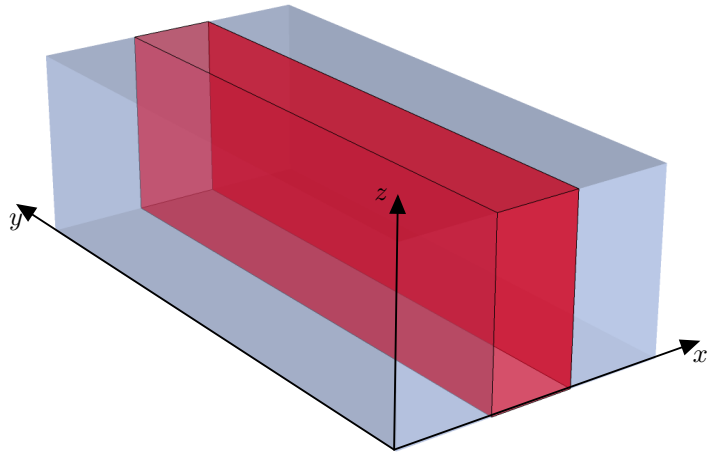

Figure 1.2 Three dimensional slab waveguide. The different refractive indices are indicated by different colors. Specifically, the core region of the waveguide is red, and the cladding region is blue.

foundation for results obtained in the open geometry.

The closed geometry approach assumes that the investigated structure is enclosed inside perfectly conducting walls, and hence that the electric field vanishes at and outside of these boundaries. This provides a set of homogeneous boundary conditions that form a regular Sturm-Liouville problem for the x-eigenmodes. Further calculations benefit immensely from this because a discrete and complete set of orthogonal eigenmodes are determined. Physically, enclosing the structure inside perfectly conducting walls resembles a situation in which the structure is enclosed inside metallic walls. The approach of calculating optical eigenmodes in a closed geometry is highly analogous to the well-studied calculation of wave-functions in an infinite potential-well. The wave-functions in the infinite potential-well are determined from the solutions to the time-independent Schrödinger equation, subject to the same boundary conditions as the closed geometry. In determining optical eigenmodes, the Helmholtz equation is solved, and since the Schrödinger and the Helmholtz equations both involve the Laplace operator, mathematically their respective solutions are identical.

The results obtained in the closed geometry approach serve to illuminate the shortcomings of this method. Due to the perfectly conducting walls, parasitic interference effects perturb the electric field. Even when the size of the closed geometry is increased substantially, interference effects continue to exist, but the region of negligible interference increases. Furthermore, modeling of the spontaneous emission rate is shown to depend heavily on the width of the geometry, and poorly converging and oscillatory results are obtained as the width is increased. A possible solution to diminish the effects of the finite size of the geometry includes the introduction of advanced boundary conditions such as perfectly matched layers [Gregersen3, Chapter 3].

This project, however, seeks to circumvent the problem entirely by removing the boundary conditions at the outer boundaries, and instead study an open geometry. The open geometry may conveniently be thought of as the limiting case of the closed geometry where the width of the closed geometry tends to infinity. Further, the open geometry, as the closed geometry, has an analogous in quantum mechanics, namely solutions to the Schrödinger equation in finite potential domains. Work on waveguide layers in an

open geometry has been carried out in [Tigelis], and the study of the open geometry in this project takes its foundation in this paper. Pursuing the open geometry rather than application of advanced boundary conditions is motivated by the hope of obtaining more accurate results for the normalized spontaneous emission rate. The Q-factor of microcavities relates directly to the normalized spontaneous emission rate [Purcell], and numerical calculations of the Q-factor in micropillar cavities by use of an improved perfectly matched layer technique obtained relative errors on the order of 10%. It is, however, assumed that the physically more realistic approach of an open geometry will yield even better results [Gregersen2].

In Chapter 2, the Maxwell equations and a number of assumptions concerning the structure to be investigated are employed to derive the Helmholtz equations that govern the electric and magnetic fields, respectively. Furthermore, the polarization of the electric field is discussed, and this leads to a scalar Helmholtz equation. This scalar equation is a partial differential equation for which generic solutions are given which concludes the chapter.

Chapter 3 introduces and analyzes the closed geometry approach. Boundary conditions along both x and z are used in connection with the generic solutions to the scalar Helmholtz equation to expand the field everywhere inside the closed geometry. Having determined the electric field, the spontaneous emission rate related to a dipole current source inside the structure is expressed as a function of the width of the geometry, and, as earlier stated, both the field plots and the calculations of the spontaneous emission rate uncover the limitations of the closed geometry approach.

In Chapter 4, the open geometry approach for uniform and waveguide layers is introduced. The different types of x-eigenmodes in these layers that may comprise both a set of discrete eigenmodes as well as a continuum of eigenmodes are derived and discussed. The expansion of the electric field is presented, and this is used to determine the spontaneous emission rate as a function of the degree of discretization of the electric field. Contrary to the closed geometry, these results converge.

Chapter 5 finally presents an open geometry of two layers, and essentially this chapter is concerned with the determination of reflection and transmission at the layer interfaces in two-layered structures. Field plots and plots of reflection and transmission coefficients are presented, and an outline for the determination of the spontaneous emission rate in a three-layer open geometry is given.

Chapter 2

Wave Equations

2.1 Introduction

In this chapter, the Helmholtz equations that govern the propagation of the electromagnetic waves (EWs) are derived. The derivation starts from Maxwell's equations, and a number of assumptions concerning the slab structures are applied. Subsequently, the polarization of the EWs is discussed and in connection with the coupling between the electric and magnetic fields, a scalar Helmholtz equation for the electric field is presented and solved. This general solution is used in the further analysis of both the closed geometry (Chapter 3) and the open geometry (Chapters 4 and 5).

The definitions and derivations in this chapter follow the outline in [Griffiths, Gregersen1].

2.2 Maxwell Equations and Helmholtz Equation

The point of departure for the analysis of the slab structure is Maxwell's equations:

$$\nabla \cdot \mathbf{D} = \rho_f, \tag{2.1a}$$
$$\nabla \cdot \mathbf{B} = 0, \tag{2.1b}$$
$$\nabla \times \mathbf{E} = -\frac{\partial \mathbf{B}}{\partial t}, \tag{2.1c}$$
$$\nabla \times \mathbf{H} = \mathbf{J}_f + \frac{\partial \mathbf{D}}{\partial t}, \tag{2.1d}$$

where $\mathbf{D}, \mathbf{B}, \mathbf{E}$, and $\mathbf{H}$ are the electric displacement field, the magnetic field, the electric field, and the magnetic $\mathbf{H}$-field, respectively, and where ρ_f and $\mathbf{J}_f$ are the free charge density and free current density, respectively. In linear media, which are assumed throughout the report, the electric and magnetic fields, respectively, are related through the following constitutive relations:

$$\mathbf{D} = \epsilon \mathbf{E} \equiv \epsilon_0(1 + \chi_e)\mathbf{E}, \tag{2.2a}$$
$$\mathbf{B} = \mu \mathbf{H} \equiv \mu_0(1 + \chi_m)\mathbf{H}, \tag{2.2b}$$

where $\epsilon, \epsilon_0, \chi_e, \mu, \mu_0$, and χ_m are the permittivity, the vacuum permittivity, the electric susceptibility, the permeability, the vacuum permeability, and the magnetic susceptibility, respectively. These quantities are material parameters and are assumed piecewise constant

in space which will be further elaborated in the treatment of the geometries to be analyzed in the following chapters. In the semiconductors that structures of this project is assumed consisting of, the density of free charges is minuscule and the materials are non-magnetic, and therefore it is assumed that $\rho_f = 0$, $\mathbf{J}_f = \mathbf{0}$, and $\mu = \mu_0$. Similarly, it is assumed that the fields are separable in a spatially dependent and a time-dependent part, where the time-dependence for the fields is assumed harmonic:

$$\mathbf{F}(\boldsymbol{r}, t) = \mathbf{F}_{\mathrm{sp}}(\boldsymbol{r}) \exp(-i\omega t), \qquad \mathbf{F} \in \{\mathbf{E}, \mathbf{D}, \mathbf{B}, \mathbf{H}\}. \tag{2.3}$$

The subscript sp denotes the spatially dependent parts of the fields, and ω denotes the angular frequency of the harmonic time dependence. As given by the time-dependence in Eq. (2.3), complex notation is used to express the fields, and throughout the report the corresponding physical fields are given as the real parts of these.

In the following, all fields are implicitly spatially dependent, that is, $\mathbf{F}(\boldsymbol{r}) \equiv \mathbf{F}_{\mathrm{sp}}(\boldsymbol{r})$, while the time-dependence is explicit. With these assumptions and the constitutive relations in Eqs. (2.2), the Maxwell equations reduce as follows:

$$\begin{aligned} \nabla \cdot \mathbf{D} = \nabla \cdot (\epsilon \mathbf{E}) &= \epsilon \exp(-i\omega t) \nabla \cdot \mathbf{E}(\boldsymbol{r}) = 0 \\ &\Updownarrow \\ \nabla \cdot \mathbf{E}(\boldsymbol{r}) &= 0, \end{aligned} \tag{2.4a}$$

$$\begin{aligned} \nabla \cdot \mathbf{B} = \nabla \cdot (\mu_0 \mathbf{H}) &= \mu_0 \exp(-i\omega t) \nabla \cdot \mathbf{H}(\boldsymbol{r}) = 0 \\ &\Updownarrow \\ \nabla \cdot \mathbf{H}(\boldsymbol{r}) &= 0, \end{aligned} \tag{2.4b}$$

$$\begin{aligned} (\nabla \times \mathbf{E}(\boldsymbol{r})) \exp(-i\omega t) &= -\frac{\partial}{\partial t} \left(\mu_0 \mathbf{H}(\boldsymbol{r}) \exp(-i\omega t)\right) = \mu_0 i\omega \mathbf{H}(\boldsymbol{r}) \exp(-i\omega t) \\ &\Updownarrow \\ \nabla \times \mathbf{E}(\boldsymbol{r}) &= \mu_0 i\omega \mathbf{H}(\boldsymbol{r}), \end{aligned} \tag{2.4c}$$

$$\begin{aligned} (\nabla \times \mathbf{H}(\boldsymbol{r})) \exp(-i\omega t) &= \frac{\partial}{\partial t} \left(\epsilon \mathbf{E}(\boldsymbol{r}) \exp(-i\omega t)\right) = -\epsilon i\omega \mathbf{E}(\boldsymbol{r}) \exp(-i\omega t) \\ &\Updownarrow \\ \nabla \times \mathbf{H}(\boldsymbol{r}) &= -\epsilon i\omega \mathbf{E}(\boldsymbol{r}). \end{aligned} \tag{2.4d}$$

To avoid cumbersome notation, the conventions $\mathbf{E} \equiv \mathbf{E}(\boldsymbol{r})$ and $\mathbf{H} \equiv \mathbf{H}(\boldsymbol{r})$ are used in what follows. Then, by applying the curl operator on both sides in Eqs. (2.4c) and (2.4d), the following identities are obtained:

$$\nabla \times (\nabla \times \mathbf{E}) = \nabla(\nabla \cdot \mathbf{E}) - \nabla^2 \mathbf{E} = \mu_0 i\omega (\nabla \times \mathbf{H}), \tag{2.5a}$$

$$\nabla \times (\nabla \times \mathbf{H}) = \nabla(\nabla \cdot \mathbf{H}) - \nabla^2 \mathbf{H} = -\epsilon i\omega (\nabla \times \mathbf{E}). \tag{2.5b}$$

Eqs. (2.4a) and (2.4b) require that both $\mathbf{E}$ and $\mathbf{H}$ are divergence-free. Using this and the identities for the curls of $\mathbf{E}$ and $\mathbf{H}$ in Eqs. (2.4c) and (2.4d), respectively, finally decouples the equations:

$$-\nabla^2 \mathbf{E} = \mu_0 \epsilon \omega^2 \mathbf{E} \Leftrightarrow \nabla^2 \mathbf{E} + \mu_0 \epsilon \omega^2 \mathbf{E} = \mathbf{0}, \tag{2.6a}$$

$$-\nabla^2 \mathbf{H} = \mu_0 \epsilon \omega^2 \mathbf{H} \Leftrightarrow \nabla^2 \mathbf{H} + \mu_0 \epsilon \omega^2 \mathbf{H} = \mathbf{0}. \tag{2.6b}$$

The wave number – or propagation constant – of free space, k_0, is related to the angular frequency, ω, through $\omega = k_0 c$. Also, since $\mu = \mu_0$, the refractive index, n, is given as $n = \sqrt{\epsilon_r}$. Applying this, the expression $\mu_0 \epsilon \omega^2$ can be rewritten to a form more suitable for the ensuing treatment:

$$\mu_0 \epsilon \omega^2 = \mu_0 \epsilon_r \epsilon_0 k_0^2 c^2 = \mu_0 \epsilon_0 c^2 \epsilon_r k_0^2 = n^2 k_0^2. \tag{2.7}$$

Insertion of this in Eqs. (2.6) finally produces Helmholtz equations for the **E**- and **H**-fields, respectively:

$$\boxed{\nabla^2 \mathbf{E} + n^2 k_0^2 \mathbf{E} = \mathbf{0},} \tag{2.8a}$$

$$\boxed{\nabla^2 \mathbf{H} + n^2 k_0^2 \mathbf{H} = \mathbf{0}.} \tag{2.8b}$$

Eqs. (2.8) are a set of partial differential equations (PDEs) in each of the three Cartesian components of the electric field and of the magnetic field, respectively. All future references to the electric field and the magnetic field will implicitly be to the **E**- and **H**-fields, respectively. In the following sections, the polarization of the EW and the coupling between the electric and magnetic fields will be discussed, which leads to a significant reduction in the number of PDEs to be solved.

2.3 Polarization

This section presents a brief discussion of the possible polarization types. To this end, a few concepts need to be presented, and reference in the following is made to Fig. 1.2. The normal to an interface plane is a direction along which the refractive changes, that is, the xy- and yz-planes are interface planes (in the figure, the structure has no variation along the z-direction, however, structures with variation along z will be treated). The plane of incidence for each of the interface planes is the plane that contains the $\boldsymbol{k}$-vector, defining the propagation direction, and that is perpendicular to the interface plane. In this case, this makes the xz-plane a mutual plane of incidence for the interface planes.

Three different types of polarization exist, namely transverse electric (TE), transverse magnetic (TM), and transverse electromagnetic (TEM).

- TE-waves: The electric field is perpendicular, or transverse, to the plane of incidence, and consequently $E_x = E_z = 0$. The polarization of the magnetic field can be found from the fact that **E**, **H** and $\boldsymbol{k}$ must be mutually orthogonal.

- TM-waves: The magnetic field is transverse to the plane of incidence such that $H_x = H_z = 0$. The polarization of the electric field can be found by application of the orthogonal relationship between **E**, **H** and $\boldsymbol{k}$.

- TEM-waves: The electric and magnetic field are both transverse to the plane of incidence. This is only possible if the $\boldsymbol{k}$-vector points along z, such that two distinct planes of incidence can be defined.

In the types of structures treated in this report, the TEM-waves do not satisfy the Maxwell equations and corresponding boundary conditions, and this type of polarization is therefore not discussed any further [Griffiths, p. 407]. As discussed in the introductory chapter, the treatment of TM-waves is omitted, and thus TE-waves are assumed onward.

Slab structures with regions of different refractive indices, constant within different regions, will be treated in Chapters 3, 4, and 5, and as will be shown, fully analytical solutions of the Helmholtz equations do not exist for these. Therefore, numerical methods

will be applied, and due to computation time and memory limitations this calls for assumptions that will reduce the calculations from the full 3D-problem into a 2D-problem. As argued in the previous chapter, this is obtained by assuming that the geometry is large in extent along y as the electric field then only depends on x and z.

2.4 Coupling of E- and H-Fields

Expressing Eq. (2.4c), by use of $E_x = E_z = 0$, gives:

$$\nabla \times \mathbf{E} = \begin{bmatrix} \dfrac{\partial E_z}{\partial y} - \dfrac{\partial E_y}{\partial z} \\ \dfrac{\partial E_x}{\partial z} - \dfrac{\partial E_z}{\partial x} \\ \dfrac{\partial E_y}{\partial x} - \dfrac{\partial E_x}{\partial y} \end{bmatrix} = \begin{bmatrix} -\dfrac{\partial E_y}{\partial z} \\ 0 \\ \dfrac{\partial E_y}{\partial x} \end{bmatrix} = \mu_0 i\omega \begin{bmatrix} H_x \\ H_y \\ H_z \end{bmatrix}, \tag{2.9}$$

which shows that once the electric field (or more precisely: the only non-zero component of the **E**-field, E_y) is determined, the magnetic field is given. Therefore, throughout the rest of this report, the EWs are described in terms of the electric field. In the following section, the Helmholtz equation in Eq. (2.8a) is solved for the y-component of the electric field, E_y.

2.5 Solution of Scalar Helmholtz Equation

As a result of the discussions in the preceding sections, the vector PDE in Eq. (2.8a) can be reduced to a scalar PDE in E_y:

$$\boxed{\nabla^2 E_y + n^2 k_0^2 E_y = 0.} \tag{2.10}$$

The solutions to the PDE depend on the types of boundary conditions (BCs) that are applied, but before discussing the BCs further, a general solution to the equation is derived. The PDE in Eq. (2.10) is a linear and homogeneous PDE, and therefore it is natural to attempt a product solution. To this end, it is assumed that E_y is separable in an x- and in a z-dependent part:

$$E_y(x, z) = e_x(x)e_z(z) \equiv e_x e_z. \tag{2.11}$$

The assumption of a product solution will be validated when $e_x(x)$ and $e_z(z)$ have been determined. Next, the product solution is inserted in Eq. (2.10):

$$\nabla^2(e_x e_z) + n^2 k_0^2 e_x e_z = 0, \tag{2.12a}$$

$$\Updownarrow$$

$$\frac{\mathrm{d}^2 e_x}{\mathrm{d}x^2} e_z + \frac{\mathrm{d}^2 e_z}{\mathrm{d}z^2} e_x + n^2 k_0^2 e_x e_z = 0 \tag{2.12b}$$

$$\Updownarrow$$

$$\frac{1}{e_z}\frac{\mathrm{d}^2 e_z}{\mathrm{d}z^2} = -\left(\frac{1}{e_x}\frac{\mathrm{d}^2 e_x}{\mathrm{d}x^2} + n^2 k_0^2\right) \equiv -\beta^2. \tag{2.12c}$$

Formally, the second bi-implication is only valid where $e_x e_z \neq 0$. Since the left hand side of Eq. (2.12c) only depends on z, and the right hand side only depends on x, they must both equal the same constant, $-\beta^2$. Then, the PDE may be decoupled into two ordinary differential equations (ODEs):

$$\frac{\mathrm{d}^2 e_x}{\mathrm{d}x^2} = -(n^2 k_0^2 - \beta^2) e_x \equiv -\kappa^2 e_x, \tag{2.13a}$$

$$\frac{\mathrm{d}^2 e_z}{\mathrm{d}z^2} = -\beta^2 e_z. \tag{2.13b}$$

The ODEs in Eqs. (2.13) are on the Sturm-Liouville (SL) form, and if the corresponding BCs also are of SL-form, the ODEs have an infinite number of solutions. Also, the eigenvalues, $-\beta^2$ and $-\kappa^2$, are real and form increasing sequences where each eigenvalue correspond to one eigenmode. In this context, each eigenvalue and corresponding eigenmode may conveniently be labeled by some index, e.g. $j = 1, 2, 3, \ldots$. Finally, the solutions to each of the ODEs form an orthogonal set [Asmar, Chapter 6]. Strictly, these facts only hold for regular SL-problems, but as will be discussed in Section 3.2, the closed geometry forms a regular SL-problem. The solutions to the ODEs are:

$$\boxed{\begin{aligned} e_{x,j}(x) &= a_j \exp(i\kappa_j x) + b_j \exp(-i\kappa_j x), \\ e_{z,j}(z) &= c_{1,j} \exp(i\beta_j z) + c_{2,j} \exp(-i\beta_j z), \end{aligned}} \tag{2.14a, 2.14b}$$

where a_j, b_j, $c_{1,j}$, $c_{2,j}$ and β_j are constants that must be determined for any $j = 1, 2, 3, \ldots$. Once β_j is determined, κ_j is implicitly given. In Appendix B.1, it is verified that the product solution defined by Eqs. (2.11) and (2.14) satisfies the scalar Helmholtz equation in Eq. (2.10) for an arbitrary j.

The open geometry is not a regular SL-problem, but the modes are, nonetheless, still represented by the generic forms in Eqs. (2.14). As discussed in Chapters 4 and 5, the eigenmodes in the open geometry generally comprise a finite number of discrete modes and a continuum of modes, termed guided modes and radiation modes, respectively. These satisfy orthogonality relations presented in the mentioned chapters.

With the harmonic time-dependence in Eq. (2.3), the two terms in the solution for the x-dependent part of E_y may be interpreted as a forward and a backward propagating wave along the x-direction:

- $\exp(i\kappa_j x)$ represents a wave that propagates along the positive x-direction.
- $\exp(-i\kappa_j x)$ represents a wave that propagates along the negative x-direction.

The same holds for the z-dependent part of E_y, that is, the first term in Eq. (2.14b) represents a wave that propagates along the positive z-direction while the second term represents a wave propagating along the negative z-direction.

The solutions in Eqs. (2.14) are valid when β_j and κ_j are constant in space. Therefore, the solutions of the ODEs are only valid when the refractive index, n, is constant which restricts this method to step-profile geometries in which the refractive index is constant in certain regions. The solution must be carried out separately in each region of constant refractive index and then coupled to solutions in adjacent regions by application of BCs. This explains the assumption of piecewise constant material parameters, discussed in Section 2.2.

Over any interface, it is demanded that the parallel component of the electric field is continuous. Hence, by the discussion of the interface planes and the polarization in

Section 2.3, the electric field must be continuous in all points [Griffiths, p. 333]. From the coupling between the **E**- and **H**-fields (presented in Section 2.4) and for the **H**-field to remain finite, it must likewise be demanded that the electric field is differentiable in all points. Thus, the demands for continuity and differentiability determines the BCs. However, the actual formulation and application of these BCs, needed to determine the constants in Eqs. (2.14), depend on the structure under investigation, and furthermore different approaches are used along x and z. The details of these are presented in Chapter 3 for the closed geometry and in Chapters 4 and 5 for the open geometry.

2.6 Summary

In this chapter, vectorial wave equations for the **E**- and **H**-fields, both on the Helmholtz form, have been derived from the Maxwell equations. Considerations of the slab structure, the polarization and the coupling between the electric and magnetic fields led to simplifications that allowed the vectorial PDEs to be reduced into a single scalar PDE in the y-component of the electric field, E_y. By assuming that E_y was separable in x- and z-dependent functions, the PDE was decoupled into ODEs in these functions that were on the Sturm-Liouville form. Following this, generic solutions that did not take into account the BCs were given. Most importantly, these solutions, or eigenmodes, form complete and orthogonal sets. Given this property, the electric field in the structures may be expanded on these eigenmodes, and in brief the task is to determine the corresponding expansion coefficients in the various structures to be analyzed. The determination of the eigenmodes and eigenvalues (propagation constants) and further of the expansion coefficients is of central importance in the following work, and is a dominant topic in the following chapters.

Chapter 3

Closed Geometry

3.1 Introduction

This chapter will introduce a first approach to calculating the electric field in an arbitrary refractive index geometry, due to an incident wave. A closed geometry approach in which the geometry is limited to a finite size along the x-axis will be employed. This approach significantly simplifies the calculations as it ensures an infinite and discrete set of eigenmodes. The chapter also serves to illustrate the principles and theory necessary to accurately determine transmission and reflection effects at boundaries, inter alia via the introduction of a scattering matrix formalism.

As described in Chapter 2, it suffices to determine the y-component of the **E**-field, E_y, when investigating the electric field. The challenge in the determination of E_y is the derivation of the x-dependent part of the field, the eigenmodes, since the z-dependent parts are then implicitly determined from Eq. (2.14b). Firstly, geometries with uniformity along z are considered. Proceeding to include non-uniformity along z prompts the need for a scattering matrix formalism that serves to ensure continuity and differentiability across z-interfaces.

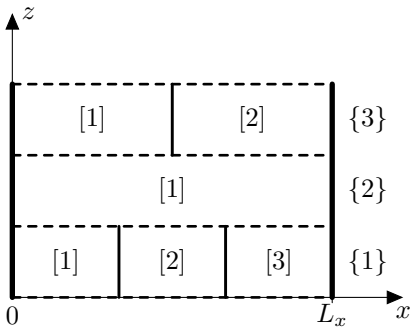

Figure 3.1 Closed geometry of three layers that are divided into three, one and two zones, respectively.

The numerical results from the closed geometry approach will serve to clarify the need for another approach, and specifically parasitic reflections due to the x-boundaries will be discussed. Using the developed closed geometry theory, the spontaneous emission rate due to a dipole will be examined by determining the power emitted from the dipole.

The results of this examination will further clarify the limitations of the closed geometry approach.

Before proceeding, a terminology for the geometries is established. Fig. 3.1 shows a geometry of three *layers* that contain three, one and two *zones*, respectively. A layer denotes a part of the geometry in which the refractive index is constant along z. Each layer may be divided into several zones that are regions of the layer with constant refractive index along x. A layer is denoted by a number in curled brackets, and in each layer the zones are denoted by numbers in edged brackets. From this point, this convention applies to all figures and quantities that are presented. Thus, e.g. the x-propagation constant corresponding to the jth eigenmode, in the qth layer and in the kth zone is $\kappa_j^{\{q\},[k]}$.

3.2 x-Boundary Conditions

Initial Description

A geometry with uniformity of the refractive index along z is shown in the illustrations in Fig. 3.2. In the terminology introduced in the previous section, the illustrations depict a single layer divided into three zones with distinct refractive indices, and this case is that of an asymmetrical waveguide. In the illustrations, the outer x-boundaries at $x = 0$ and $x = L_x$ and the inner boundaries at $x = L_{1,2}$ and $x = L_{2,3}$ are indicated.

In the following, a model to determine eigenmodes for layers with an arbitrary number of zones and arbitrary refractive indices is developed. It should be noted that although the formalism will be able to handle arbitrary variations, the actual numerical implementation will enforce a practical limit on the number of zones and layers, the maximum variations of the refractive indices and the minimum zone and layer widths.

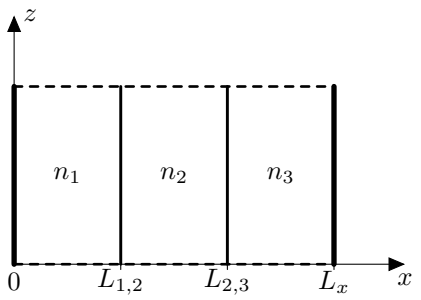

(a) xz-profile in a layer with uniformity of the refractive index along z. The refractive index in each zone is marked.

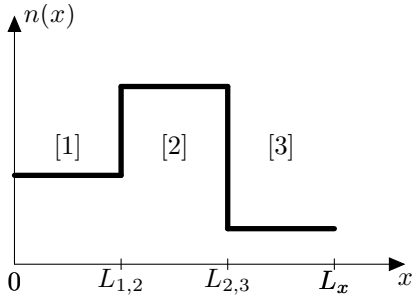

(b) Refractive index profile, $n(x)$, along the x direction. Each zone is denoted by a numeral.

Figure 3.2 Single layer uniform along z.

As mentioned in Section 2.5, the electric field for TE-waves should be continuous and differentiable in all points. Referring to the solutions of the Helmholtz equation, given in Eq. (2.14a), it is apparent that the solutions inside each zone fulfill these criteria. However, it must be ensured that the criteria are also fulfilled at each zone boundary, that is, an allowed mode profile should be continuous and differentiable across any zone boundary. Considering a certain $e_{x,j}(x)$ in an arbitrary zone, p, and denoting it by $e_{x,j}^{[p]}(x)$,

the *inner* BCs can be written as:

$$e_{x,j}^{[p]}(L_{p,p+1}) = e_{x,j}^{[p+1]}(L_{p,p+1}), \tag{3.1a}$$

$$\left.\frac{\mathrm{d}e_{x,j}^{[p]}}{\mathrm{d}x}\right|_{x=L_{p,p+1}} = \left.\frac{\mathrm{d}e_{x,j}^{[p+1]}}{\mathrm{d}x}\right|_{x=L_{p,p+1}}, \tag{3.1b}$$

for all $p = 1, 2, \ldots, P-1$, where P equals the total number of zones in the layer. This is a general result that holds for both the closed and the open geometry approaches. However, the *outer* BCs differ in the two approaches. For the closed geometry, it is assumed that each layer is bordered by perfectly conducting walls at $x = 0$ and at $x = L_x$. As a result of this, the electric field must vanish at $x = 0$ and at $x = L_x$:

$$e_{x,j}^{[1]}(0) = 0, \tag{3.2a}$$

$$e_{x,j}^{[P]}(L_x) = 0. \tag{3.2b}$$

By combining the inner BCs from Eqs. (3.1) with the outer BCs from Eqs. (3.2), a total of $2P$ BCs are obtained. It is noticed that the outer BCs are homogeneous Dirichlet BCs whereby the homogeneous ODEs in Eq. (2.13a) constitute regular Sturm-Liouville problems. As a consequence of this, the corresponding eigenmodes form an orthogonal basis for all functions in $L^2(0, L_x)$ [Christensen2, Theorem 10.1.6]. This implies that any closed geometry wave profile may be expanded on these eigenmodes, and the determination of the eigenmodes is discussed in the following section.

Eigenvalues and Eigenmodes

The jth eigenmode in a layer of P regions is determined when the corresponding eigenmode coefficients $(a_j^{[1]}, b_j^{[1]}, a_j^{[2]}, b_j^{[2]}, \ldots, a_j^{[P]}, b_j^{[P]})$ and propagation constants $(\kappa_j^{[1]}, \kappa_j^{[2]}, \ldots, \kappa_j^{[P]})$ have been determined. The determination of these is enabled by coupling the general solutions from Eq. (2.14a) with the BCs given in Eqs. (3.1) and (3.2). In Appendix C.1, a homogeneous matrix equation, $\mathbf{A}_j \boldsymbol{c}_j = \mathbf{0}$, is derived, where $\boldsymbol{c}_j$ contains the eigenmode coefficients:

$$\boldsymbol{c}_j = \left[a_j^{[1]}, \quad b_j^{[1]}, \quad a_j^{[2]}, \quad b_j^{[2]}, \quad \ldots, \quad a_j^{[P]}, \quad b_j^{[P]}\right]^T. \tag{3.3}$$

The matrix $\boldsymbol{A}_j$ is presented in Appendix C.1 along with the corresponding zone-solution form, see Eq. (C.2).

The homogeneous matrix equation $\mathbf{A}_j \boldsymbol{c}_j = \mathbf{0}$ is directly dependent on the values of $\kappa_j^{[p]}$, and these values are given through $\kappa_j^{[p]} = \sqrt{n_{[p]}^2 k_0^2 - \beta_j^2}$, cf. Eq. (2.13a), where it should be noted that $n_{[p]}$ and k_0 are known constants, whereas β_j is unknown. Since trivial solutions are of no interest, values of β^2 for which the matrix equation has non-trivial solutions are sought for, and these are denoted β_j^2. In order to obtain non-trivial solutions, the $P \times P$ matrix, $\mathbf{A}_j$, must be singular which is obtained when the determinant of $\mathbf{A}_j$ vanishes. According to SL theory, there exists only one eigenmode for each eigenvalue, and therefore the rank of the matrix must equal $P - 1$. The matrix $\mathbf{A}_j$ is, as previously mentioned, implicitly a function of the squared z-propagation constant, β^2. The largest allowable value of β^2 equals $n_{\max}^2 k_0^2$, where $n_{\max}$ is the maximum of the step-profile, $n(x)$. No modes can exist above this limit, since $\kappa_j^{[p]}$ would then take on imaginary values in

all zones. This would result in exponentially in- or decreasing zone-solutions in all zones which would violate the BCs. As a consequence of this, an infinity of eigenmodes must exist in the interval:

$$-\infty < \beta^2 < n_{\max}^2 k_0^2. \tag{3.4}$$

Since $-\beta_j^2$ constitute an increasing sequence, it is natural to apply a numerical solver to scan through the possible β^2-values from $n_{\max}^2 k_0^2$ and downwards. Each $\boldsymbol{c}_j$ is then given as the solution to the homogeneous matrix equation for each value of β_j^2. Determining the solution is the equivalent of determining the kernel, or null-space, of $\mathbf{A}_j(\beta_j^2)$. This implies that the solutions can be scaled by any complex factor since the kernel is the span of a vector.

To illustrate the oscillations of the determinant, the real and imaginary parts of $\det(\boldsymbol{A})$ for a specific layer are plotted in Fig. 3.3 illustrating the determination of the first five values of β^2. These fulfill that $\mathrm{Re}(\det(\mathbf{A})) = \mathrm{Im}(\det(\mathbf{A})) = 0$, and numerical solving of the problem must consequently take care to ensure that both requirements are met simultaneously.

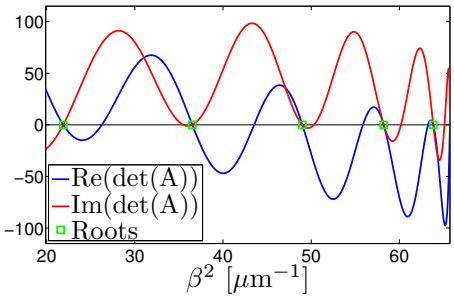

Figure 3.3 Real and imaginary part of $\det(\mathbf{A})$. The layer is a waveguide layer of width $L_x = 10\,\mu$m with core-width $2\,\mu$m and refractive indices 1 and 2 in the cladding and core, respectively.

This method is termed the *semi-analytical approach* as the solutions consist of fully analytical expressions with the exception that the propagation constants β_j and κ_j and coefficients in $\boldsymbol{c}_j$ are determined numerically.

3.3 Normalization

In order for the sequence of semi-analytical eigenmodes, $\{e_{x,j}(x)\}_{j=1}^{\infty}$, to constitute not only an orthogonal basis, but an orthonormal basis, each eigenmode is normalized with respect to the Power inner product, $\langle \cdot, \cdot \rangle_{\mathrm{P}}$, given its name due to its similarity with the Poynting vector [Snyder, Chapter 11-4]:

$$\langle \boldsymbol{e}_j, \boldsymbol{e}_i \rangle_{\mathrm{P}} = \frac{1}{2} \int_{xy-\mathrm{plane}} (\boldsymbol{e}_j(x,y) \times \boldsymbol{h}_i^*(x,y)) \cdot \hat{\boldsymbol{z}} \, \mathrm{d}A. \tag{3.5}$$

$\boldsymbol{e}_j$ and $\boldsymbol{e}_i$ are vectorial eigenmodes in the xy-plane, that is, the x-dependent parts of the $\mathbf{E}$-fields. Similarly, $\boldsymbol{h}_i$ is a vectorial magnetic eigenmode in the xy-plane, and $\hat{\boldsymbol{z}}$ is a unit vector along z. The mathematical definitions of $\boldsymbol{e}_j$ and $\boldsymbol{h}_i$ are given in Appendix C.2. Finally, the integration is across the entire xy-plane which reduces to integration along x

since the y-integration is neglected. Using this, the coupling between the **E**- and **H**-fields (Eq. (2.9)), and the fact that the only non-zero component of **E** is E_y, an expression for the inner product is derived in Appendix C.2, and this expression is:

$$\langle \boldsymbol{e}_j, \boldsymbol{e}_i \rangle_{\mathrm{P}} = \frac{\beta_i^*}{2\mu_0\omega} \int_0^{L_x} e_{x,j}(x) e_{x,i}^*(x)\, \mathrm{d}x. \tag{3.6}$$

It is profitable to define $\mu_0\omega \equiv 1$, as it ensures clarity of the inner product. The choice of $\mu_0\omega \equiv 1$ introduces a scaling of the electric field, and consequently this field is given in arbitrary units henceforth. The Power inner product rather than other, simpler inner products is chosen since it facilitates a calculation of the spontaneous emission rate, see Section 3.8. It is noticed that the choice of μ_0 effectively scales all calculations of the spontaneous emission rate, but since only sponatenous emission rate ratios are of interest, this choice will have no impact on the results.

A normalized eigenmode, which from now is denoted $\boldsymbol{e}_j$, relates to a non-normalized eigenmode, $\check{\boldsymbol{e}}_j$, through the following expression:

$$\boldsymbol{e}_j = \frac{1}{\sqrt{\mathcal{N}_j}} \check{\boldsymbol{e}}_j, \tag{3.7}$$

where $\mathcal{N}_j$ is the normalization constant. The normalization constant is connected to the inner product of two equal eigenmodes, $\mathcal{N}_j'$, through:

$$\mathcal{N}_j' \equiv \langle \check{\boldsymbol{e}}_j, \check{\boldsymbol{e}}_j \rangle_{\mathrm{P}} \equiv \frac{\beta_j^*}{|\beta_j|} \mathcal{N}_j, \tag{3.8}$$

where the prefactor $\beta_j^*/|\beta_j|$ ensures that $\mathcal{N}_j$ is a positive real constant. The orthonormality condition for the eigenmodes is defined as:

$$\langle \boldsymbol{e}_j, \boldsymbol{e}_i \rangle_{\mathrm{P}} = \frac{\beta_j^*}{|\beta_j|} \delta_{ij}, \tag{3.9}$$

where δ_{ij} is the Kronecker delta. In other words, the normalization constant of a normalized mode is $\mathcal{N}_j = 1$, which explains the need for $\mathcal{N}_j$ to be positive and real.

The computation of the inner product, and thereby also of the normalization constants, can be carried out analytically since the eigenmodes are given as analytical functions. In the general case of a layer with more than one zone the expression in Eq. (3.6) must be rewritten into a sum of integrals, one for each zone. The fact that the inner products can be computed analytically has large advantages compared to a numerical integration approach, in the form of speed and precision. Finally, it is noted that the inner product between eigenmodes of different layers takes on a central role in the calculation of transmission and reflection matrices in Section 3.6.

3.4 Eigenmodes

Different types of eigenmodes, $e_{x,j}(x)$, may exist in different regions of constant refractive index. In this context, the x-propagation constant in the pth zone, $\kappa_j^{[p]}$, that is defined in Eq. (2.13a) as:

$$\kappa_j^{[p]} = \sqrt{n_{[p]}^2 k_0^2 - \beta_j^2}, \tag{3.10}$$

plays an important role:

- When $\kappa_j^{[p]}$ is real, the eigenmode is oscillatory in the pth zone.
- When $\kappa_j^{[p]}$ is imaginary, the eigenmode is exponentially in- or decreasing in the pth zone.

Whether $\kappa_j^{[p]}$ is real or imaginary, is decided by the refractive index of the zone, $n_{[p]}$, and by the value of β_j:

- $\kappa_j^{[p]}$ is real when $\beta_j^2 \leq n_{[p]}^2 k_0^2$.
- $\kappa_j^{[p]}$ is imaginary when $\beta_j^2 > n_{[p]}^2 k_0^2$.

The case where $\beta_j^2 = n_{[p]}^2 k_0^2$, or in other words where $\kappa_j^{[p]} = 0$, represents a field profile that is constant along x. Since the BCs at $x = 0$ and at $x = L_x$ demand that the field equals zero at these points (Eqs. (3.2)), the total field is equal to zero, and it therefore does not contribute to the set of orthogonal eigenfunctions. It is worth stressing that the values of β_j are identical for all zones in a layer, and since the refractive index varies between zones, different mode-types can exist in different zones in a layer, cf. Eq. (3.10).

In Fig. 3.2(b), a general three-zone layer with a step-index profile was presented. Now, to introduce the main characteristics of different modes, the simpler symmetric layer with $n_1 = n_3 < n_2$ is investigated. The $n(x)k_0$-profile for such a layer can be seen in Fig. 3.4. As discussed in Section 3.2 and expressed in Eq. (3.4), all values of β_j are smaller than $n_2 k_0$. This is tantamount to ensure that the values of κ_j in zone 2 are always real, and hence that the mode profiles in the high refractive index zone are always oscillatory. Therefore, the following discussion serves to determine when the mode profiles in zones 1 and 3 are exponentially decaying and when they are oscillatory. These different types of eigenmodes are termed guided modes and semi-radiating modes, respectively.

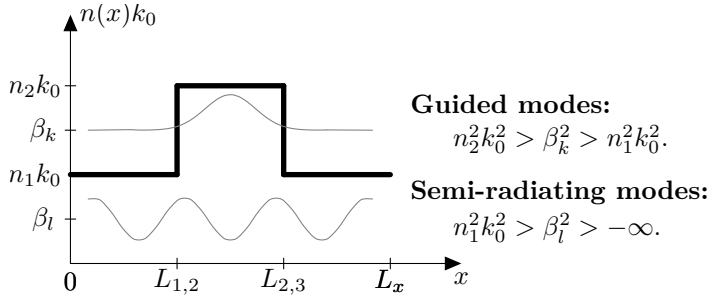

Figure 3.4 Plot of $n(x)k_0$ as function of x for a symmetric layer in a closed geometry. The refractive indices fulfill $n_1 = n_3 < n_2$. The condition for guided and semi-radiating modes are summarized and indicated schematically, and a guided and a semi-radiating mode are sketched.

Fig. 3.4 also defines two different values of β_j: β_k and β_l with $k < l$. For β_k the value of the square of the x-propagation constant in zones 1 and 3, $\kappa_k^{[1,3]}$, is:

$$\left(\kappa_k^{[1,3]}\right)^2 = n_1^2 k_0^2 - \beta_k^2 < 0, \tag{3.11}$$

and therefore $\kappa_k^{[1,3]}$ is imaginary: The mode profiles in zones 1 and 3 are exponentially in- or decreasing. For β_l, the square of the propagation constant is:

$$\left(\kappa_l^{[1,3]}\right)^2 = n_1^2 k_0^2 - \beta_l^2 > 0, \tag{3.12}$$

and $\kappa_l^{[1,3]}$ is real: The mode profiles in zones 1 and 3 are oscillatory. Obviously, the transition from guided modes to semi-radiating modes occurs when the value of β_j decreases below $n_1 k_0$.

Moving on to display eigenmode profiles, the used wavelength must first be defined: Throughout the report, the wavelength $\lambda = 1.55\,\mu$m is used in all numerical simulations, unless otherwise stated. The wavelength $1.55\,\mu$m is chosen because it is commonly used in optical communication.

Initially, examples of eigenmodes in a symmetric waveguide are presented in Figs. 3.5. The fourth mode which is a guided mode can be seen in Fig. 3.5(a). In zone 2, the mode is oscillatory, and in zones 1 and 3 it is exponentially decaying. That it is in fact the fourth mode, is verified by noting that the oscillatory part of the field fits two wavelengths in the layer. Fig. 3.5(b) displays the twentieth mode which is a semi-radiating mode, and the mode is oscillatory in all zones. The behaviors for both modes are as expected, cf. the above discussion of the different values of β_j.

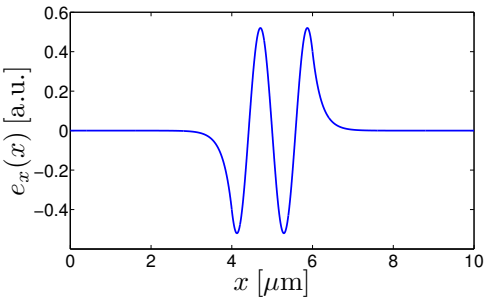

(a) Guided mode. Fourth mode, $e_{x,4}(x)$.

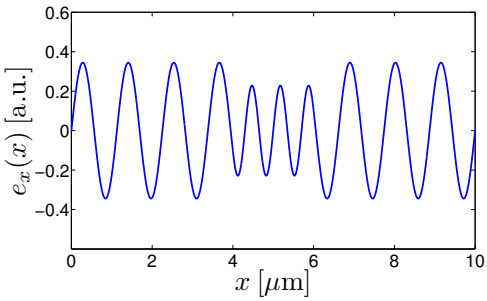

(b) Semi-radiating mode. Twentieth mode, $e_{x,20}(x)$.

Figure 3.5 Mode profiles of x-dependent part of electric field, $e_{x,j}(x)$, in a symmetric waveguide layer of three zones in a closed geometry. The parameters of the geometry are: $L_{1,2} = 4\,\mu$m, $L_{2,3} = 6\,\mu$m, $L_x = 10\,\mu$m, $n_1 = n_3 = 1$ and $n_2 = 2$.

To further illustrate the influence of the geometry and corresponding refractive index profiles on the eigenmodes, two additional layer-types are investigated. The refractive index profiles of these layers are defined in subfigures (a) of Figs. 3.6 and 3.7, and selected, corresponding mode profiles can be found in subfigures (b).

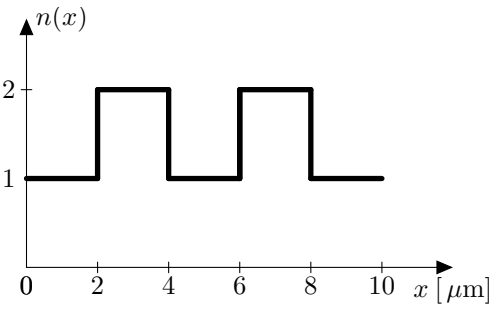

(a) Refractive index profile: $n(x)$ as function of x.

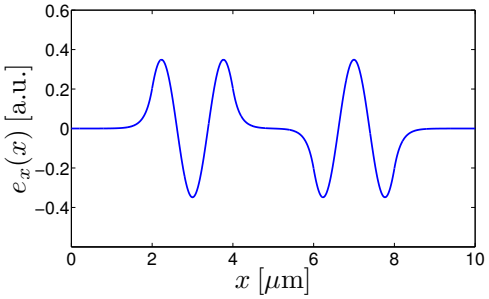

(b) Sixth mode profile, $e_{x,6}(x)$.

Figure 3.6 Symmetric layer with five zones in a closed geometry.

In Fig. 3.6(a), a symmetric geometry with two zones of refractive index $n = 2$ and three zones of refractive index $n = 1$ has been defined, and the sixth mode profile, $e_{x,6}(x)$, is plotted in Fig. 3.6(b). In the zones of highest refractive index, the mode oscillates, and in the three zones of lower refractive index the mode is exponentially decaying which thus makes it a guided mode. The geometry could represent two fibers in close vicinity where the zones of $n = 2$ and $n = 1$ represent the fiber cores and claddings, respectively.

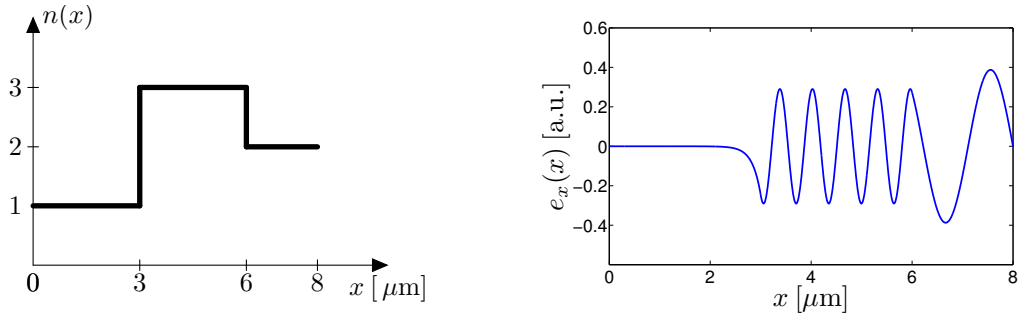

(a) Refractive index profile: $n(x)$ as function of x.

(b) Twelfth mode profile, $e_{x,12}(x)$.

Figure 3.7 Asymmetric layer with three zones in a closed geometry.

In Fig. 3.7(a), an asymmetric waveguide with three zones of refractive indices $n = 1, 3, 2$, respectively, has been defined, and in Fig. 3.7(b) the twelfth mode profile, $e_{x,12}(x)$, is plotted. The mode oscillates in the zones of refractive indices $n = 2, 3$ and is exponentially decaying in the zone with $n = 1$, which, by extending the previous naming convention, makes it a 'semi-guided' or 'semi-semi-radiating' mode.

Finally, the significance of the β_j-values in relation with the z-dependent part of the field is discussed briefly. The sign of β_j^2 clearly determines if β_j is real (zero or positive sign) or imaginary (negative sign). Referring to the solutions in Eq. (2.14b), it is concluded that real β_j represent fields oscillating along z, that is, propagating waves, whereas imaginary β_j represent exponentially decaying fields along z, that is, evanescent waves.

In Section 3.6, the case of multiple layers is investigated by introducing the BCs that ensure continuity and differentiability of the field along z. Next, Section 3.7 presents 2D field profiles in structures of multiple layers and zones based on the BCs developed in the preceding section. However, before the z-BCs and field profiles can be derived and presented, a representation of the field as an expansion on the eigenmodes is given in the following section.

3.5 Eigenmode Expansion

As discussed in Chapter 2, the x-dependent eigenmodes, $e_{x,j}, j = 1, 2, \ldots$, form an orthogonal set, and with the normalization described in Section 3.3 also an orthonormal set, of eigenmodes. Hence, the electric field, $E_y(x, z) \equiv E(x, z)$, may be expanded on these eigenmodes in the following manner:

$$\boxed{E(x,z) = \sum_{j=1}^{\infty} A_j \exp(i\beta_j z) e_{x,j} + \sum_{j=1}^{\infty} B_j \exp(-i\beta_j z) e_{x,j},} \tag{3.13}$$

where A_j and B_j are constants that will be determined using the boundary conditions along z. The first sum-term represents the forward propagating part of the field, and the second sum-term represents the backward propagating part, both along z. For the definition in Eq. (3.13) to be applicable in numerical computations, the infinite sums must be uniformly convergent. Assuming this, for any $\epsilon > 0$ there exists an $N_0 \in \mathbb{N}$ such that [Christensen1, Definition 5.27]:

$$\left| E(x,z) - \left(\sum_{j=1}^{N} A_j \exp(i\beta_j z) e_{x,j} + \sum_{j=1}^{N} B_j \exp(-i\beta_j z) e_{x,j} \right) \right| < \epsilon, \tag{3.14}$$

valid $\forall N \geq N_0$, $\forall x \in [0, L_x]$. Therefore, in practice a finite number of eigenmodes, N, will be used to expand the electric field.

3.6 z-Boundary Conditions

This section treats the situation of two and more layers. Specifically, the BCs along z will be employed to evaluate the electric field in all zones and all layers. The BCs along z remain identical to the inner BCs along x, namely that the electric field is continuous and differentiable in all points and in particular at all interfaces along z. Using these conditions and the previously determined eigenmodes, a matrix approach that handles the reflections and transmissions across layers will be developed. Although the z-BCs are identical to the x-BCs, the application of these BCs will differ significantly from the application of the x-BCs that were treated in Section 3.2.

The theory presented largely follows the outline in [Gregersen1].

Reflection and Transmission Between Layers

Two layers will be treated in this section, and an illustration of two such layers, each consisting of three zones, is shown in Fig. 3.8(a). Fig. 3.8(b) illustrates the reflections and transmissions schematically: The electric field on either side of the interface, situated at $z = z_{1,2}$, is represented by a forward and a backward propagating part (blue arrows) that correspond to the two linearly independent solutions in Eq. (2.14b). At the interface

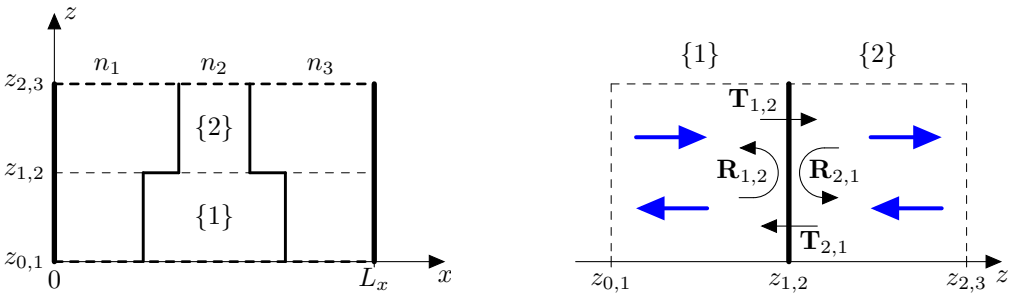

(a) Two-layer structure.

(b) Reflection and transmission at a layer-interface.

Figure 3.8 Two-layer structure.

and in both layers, part of the field is transmitted and part of the field is reflected which

is represented by the transmission and reflection matrices, $\mathbf{T}_{1,2}$, $\mathbf{T}_{2,1}$, $\mathbf{R}_{1,2}$, $\mathbf{R}_{2,1}$. With reference to the representation of the electric field, $E(x,z)$, in Eq. (3.13), the electric fields on either side of the interface may be expressed as:

$$E_1(x,z) = \sum_{j=1}^{N} A_j^{\{1\}} \exp(i\beta_j^{\{1\}}(z - z_{0,1}))e_{x,j}^{\{1\}} + \sum_{j=1}^{N} B_j^{\{1\}} \exp(i\beta_j^{\{1\}}(z_{1,2} - z))e_{x,j}^{\{1\}}, \tag{3.15a}$$

$$E_2(x,z) = \sum_{j=1}^{N} A_j^{\{2\}} \exp(i\beta_j^{\{2\}}(z - z_{1,2}))e_{x,j}^{\{2\}} + \sum_{j=1}^{N} B_j^{\{2\}} \exp(i\beta_j^{\{2\}}(z_{2,3} - z))e_{x,j}^{\{2\}}, \tag{3.15b}$$

where a superscript $\{p\}$ indicates the pth layer. Compared to the expression in Eq. (3.13), where the coefficients are defined relative to $z = 0$, the coefficients for each layer in Eqs. (3.15) have been defined relative to the interfaces that enclose the layer, respectively. Evidently, these definitions do not alter any physical properties, but are merely related to the numerical implementation.

In words, the elements in the four matrices represent how much each mode in each of the layers transmits and reflects to the modes in the other layer and in the same layer, respectively. For simplicity, it may be assumed that the structure is illuminated by a single forward propagating mode, m, in layer 1. The expansion coefficients, $A_j^{\{1\}}$ and $B_j^{\{2\}}$, from Eqs. (3.15) then reduce to:

$$A_j^{\{1\}} = \delta_{jm}, \tag{3.16a}$$

$$B_j^{\{2\}} = 0. \tag{3.16b}$$

Another consequence of the assumption is that the matrices $\mathbf{T}_{2,1}$ and $\mathbf{R}_{2,1}$ become unimportant as the backward propagating part of the field in layer 2 vanishes. The matrices $\mathbf{T}_{1,2}$ and $\mathbf{R}_{1,2}$, however, determine the remaining the expansion coefficients via:

$$B_k^{\{1\}} = \sum_{j=1}^{N} R_{1,2;k,j} A_j^{\{1\}} \exp\left(i\beta_j^{\{1\}}\left(z_{1,2} - z_{0,1}\right)\right), \tag{3.17a}$$

$$A_k^{\{2\}} = \sum_{j=1}^{N} T_{1,2;k,j} A_j^{\{1\}} \exp\left(i\beta_j^{\{1\}}\left(z_{1,2} - z_{0,1}\right)\right), \tag{3.17b}$$

where the subscript k,j indicates the element in the kth row and in the jth column. Since all $A_j^{\{1\}}$ are given by Eq. (3.16a), the task is to determine the elements in $\mathbf{T}_{1,2}$ and $\mathbf{R}_{1,2}$. When these are known, Eqs. (3.17) give the remaining expansion coefficients, $B_k^{\{1\}}$ and $A_k^{\{2\}}$, and by the expressions in Eqs. (3.15) the electric field is determined on both sides of the interface.

To determine the elements in the matrices, the BCs along z must be applied, and these are:

$$E_1(x, z_{1,2}) = E_2(x, z_{1,2}), \tag{3.18a}$$

$$\left.\frac{\partial E_1(x,z)}{\partial z}\right|_{z=z_{1,2}} = \left.\frac{\partial E_2(x,z)}{\partial z}\right|_{z=z_{1,2}}. \tag{3.18b}$$

Using the BCs and the orthonormality properties of the eigenmodes (Eq. (3.9)), the following equations in $\mathbf{T}_{1,2}$ and $\mathbf{R}_{1,2}$ may be obtained:

$$\tilde{\mathbf{I}} + \tilde{\mathbf{I}}\mathbf{R}_{1,2}^T = \langle \mathbf{e}_{\mathbf{x}}^{\{2\}} | \mathbf{e}_{\mathbf{x}}^{\{1\}} \rangle_{\mathrm{P}} \mathbf{T}_{1,2}^T, \tag{3.19a}$$

$$\tilde{\boldsymbol{\beta}}^{\{1\}} - \tilde{\boldsymbol{\beta}}^{\{1\}}\mathbf{R}_{1,2}^T = \langle \mathbf{e}_{\mathbf{x}}^{\{2\}} | \mathbf{e}_{\mathbf{x}}^{\{1\}} \rangle_{\mathrm{P}} \boldsymbol{\beta}^{\{2\}} \mathbf{T}_{1,2}^T. \tag{3.19b}$$

where the following definitions have been applied:

$$\tilde{\mathbf{I}} = \begin{bmatrix} \beta_1^{\{1\}}/|\beta_1^{\{1\}}| & 0 & \dots & 0 \\ 0 & \beta_2^{\{1\}}/|\beta_2^{\{1\}}| & \dots & 0 \\ \vdots & \ddots & \ddots & \vdots \\ 0 & 0 & \dots & \beta_N^{\{1\}}/|\beta_N^{\{1\}}| \end{bmatrix}, \tag{3.20a}$$

$$\langle \mathbf{e}_{\mathbf{x}}^{\{2\}} | \mathbf{e}_{\mathbf{x}}^{\{1\}} \rangle_{\mathrm{P}} = \begin{bmatrix} \langle e_{x,1}^{\{2\}} | e_{x,1}^{\{1\}} \rangle_{\mathrm{P}} & \langle e_{x,2}^{\{2\}} | e_{x,1}^{\{1\}} \rangle_{\mathrm{P}} & \dots & \langle e_{x,N}^{\{2\}} | e_{x,1}^{\{1\}} \rangle_{\mathrm{P}} \\ \langle e_{x,1}^{\{2\}} | e_{x,2}^{\{1\}} \rangle_{\mathrm{P}} & \langle e_{x,2}^{\{2\}} | e_{x,2}^{\{1\}} \rangle_{\mathrm{P}} & \dots & \langle e_{x,N}^{\{2\}} | e_{2,x}^{\{1\}} \rangle_{\mathrm{P}} \\ \vdots & \vdots & \ddots & \vdots \\ \langle e_{x,1}^{\{2\}} | e_{x,N}^{\{1\}} \rangle_{\mathrm{P}} & \langle e_{x,2}^{\{2\}} | e_{x,N}^{\{1\}} \rangle_{\mathrm{P}} & \dots & \langle e_{x,N}^{\{2\}} | e_{x,N}^{\{1\}} \rangle_{\mathrm{P}} \end{bmatrix}, \tag{3.20b}$$

$$\boldsymbol{\beta}^{\{p\}} = \begin{bmatrix} \beta_1^{\{p\}} & 0 & \dots & 0 \\ 0 & \beta_2^{\{p\}} & \dots & 0 \\ \vdots & \ddots & \ddots & \vdots \\ 0 & 0 & \dots & \beta_N^{\{p\}} \end{bmatrix}, \quad p = 1, 2, \tag{3.20c}$$

$$\tilde{\boldsymbol{\beta}}^{\{1\}} = \boldsymbol{\beta}^{\{1\}} \tilde{\mathbf{I}}. \tag{3.20d}$$

Simple manipulations of Eqs. (3.19) give the following equations that allow explicit determination of $\mathbf{T}_{1,2}^T$ and $\mathbf{R}_{1,2}^T$:

$$2\tilde{\boldsymbol{\beta}}^{\{1\}} = \left(\langle \mathbf{e}_{\mathbf{x},\mathbf{j}}^{\{2\}} | \mathbf{e}_{\mathbf{x},\mathbf{j}}^{\{1\}} \rangle_{\mathrm{P}} \boldsymbol{\beta}^{\{2\}} + \tilde{\boldsymbol{\beta}}^{\{1\}} \tilde{\mathbf{I}}^{-1} \langle \mathbf{e}_{\mathbf{x},\mathbf{j}}^{\{2\}} | \mathbf{e}_{\mathbf{x},\mathbf{j}}^{\{1\}} \rangle_{\mathrm{P}} \right) \mathbf{T}_{1,2}^T, \tag{3.21a}$$

$$\mathbf{R}_{1,2}^T = \tilde{\mathbf{I}}^{-1} \left(\langle \mathbf{e}_{\mathbf{x},\mathbf{j}}^{\{2\}} | \mathbf{e}_{\mathbf{x},\mathbf{j}}^{\{1\}} \rangle_{\mathrm{P}} \mathbf{T}_{1,2}^T - \tilde{\mathbf{I}} \right). \tag{3.21b}$$

Eq. (3.21a) is a linear matrix equation that can be solved for $\mathbf{T}_{1,2}^T$, whereupon $\mathbf{R}_{1,2}^T$ is given directly by Eq. (3.21b).

From Eqs. (3.21), it is seen that the reflections and transmissions at an interface essentially depend on the overlap integral between the eigenmodes of each layer. As previously mentioned, the electric field in both layers is determined from $\mathbf{R}_{1,2}$ and $\mathbf{T}_{1,2}$, and Eqs. (3.21) thus allow computation of the electric field across two layers. Expressions for the reflection and transmission matrices $\mathbf{R}_{2,1}$ and $\mathbf{T}_{2,1}$ are given by cyclic permutations of indices in Eqs. (3.21).

It should be mentioned that transfer and reflection matrices can be extended to any general interface, q, by simply substituting $\{1\} \curvearrowright \{q\}$ and $\{2\} \curvearrowright \{q+1\}$. Furthermore, at a general interface, all four reflection and transmission matrices must be considered which is discussed in the following section.

Three-Layer Structure

When considering a structure with three layers, such as the geometry in Fig. 3.9(a), the formalism just introduced will not suffice on its own. As illustrated in Fig. 3.9(b), the

field in the second layer consists of back- and forward propagating fields, resulting from the multiple reflections of the field at interfaces $z_{1,2}$ and $z_{2,3}$. A three layer formalism must account for these multiple reflections.

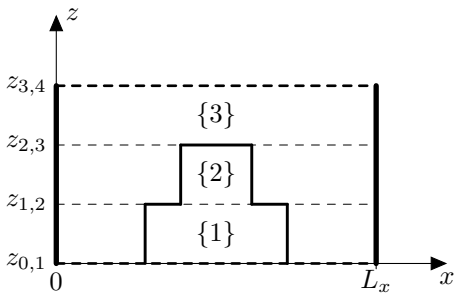

(a) Three-layer structure.

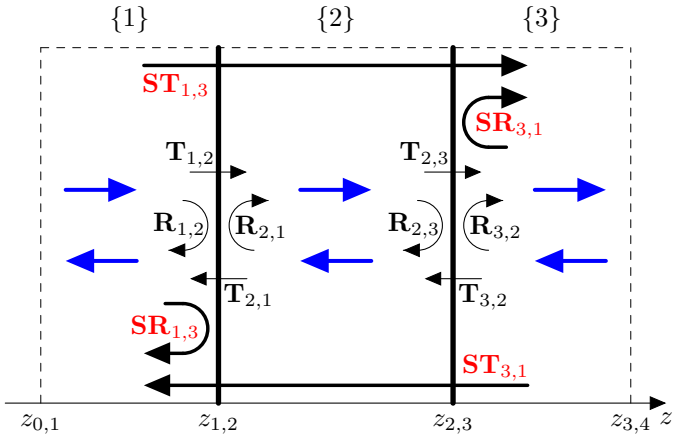

(b) The various reflections and transmissions in a three-layer structure. The illustration introduces the scattering reflection matrices, **SR**, and the scattering transmission matrices, **ST**.

Figure 3.9

For instance, the total reflection at interface $z_{1,2}$ must take into account both the initial reflection of an incoming wave, described by $\mathbf{R}_{1,2}$, and the contribution from the transmission of the left-propagating reflections in layer 2. This total or effective reflection matrix is denoted as the scattering reflection matrix, $\mathbf{SR}_{1,3}$, because it takes into account the structural setup from layer 1 to 3. Similarly, the scattering transmission matrices $\mathbf{ST}_{1,3}$ and $\mathbf{ST}_{3,1}$, illustrated in Fig. 3.9(b), describe transmissions that take into account the setup from layer 1 to 3. Maintaining the form of the electric field in Eqs. (3.15), the definitions of the scattering matrices, $\mathbf{SR}_{1,3}$ and $\mathbf{ST}_{1,3}$, are:

$$B_k^{\{1\}} = \sum_{j=1}^{N} SR_{1,3;k,j} A_j^{\{1\}} \exp\left(i\beta_j^{\{1\}} \left(z_{1,2} - z_{0,1}\right)\right), \tag{3.22a}$$

$$A_k^{\{3\}} = \sum_{j=1}^{N} ST_{1,3;k,j} A_j^{\{1\}} \exp\left(i\beta_j^{\{1\}} \left(z_{1,2} - z_{0,1}\right)\right), \tag{3.22b}$$

where subscript k, j indicates the matrix element in the kth row and in the jth column. The reversed scattering matrices, $\mathbf{SR}_{3,1}$ and $\mathbf{ST}_{3,1}$ have similar definitions, that incorporate the reversed propagation direction.

By imposing the z-BCs, the scattering matrices, $\mathbf{SR}_{1,3}$ and $\mathbf{ST}_{1,3}$, may be expressed in terms of the previously introduced reflection and transmission matrices. The derivations are carried out in Appendix C.3, and the resulting expressions are:

$$\mathbf{SR}_{1,3} = \mathbf{R}_{1,2} + \mathbf{T}_{2,1}\mathbf{P}_2\mathbf{R}_{2,3}\mathbf{P}_2 \left(\mathbf{I} - \mathbf{R}_{2,1}\mathbf{P}_2\mathbf{R}_{2,3}\mathbf{P}_2\right)^{-1} \mathbf{T}_{1,2}, \tag{3.23a}$$

$$\mathbf{ST}_{1,3} = \mathbf{T}_{2,3}\mathbf{P}_2 \left(\mathbf{I} - \mathbf{R}_{2,1}\mathbf{P}_2\mathbf{R}_{2,3}\mathbf{P}_2\right)^{-1} \mathbf{T}_{1,2}, \tag{3.23b}$$

where $\mathbf{P}_2$ is a propagation matrix, introduced to handle the phase-change related to the propagation of a wave. The propagation matrix is a diagonal matrix, and has the following elements in a general layer q:

$$P_{q;j,k} = \delta_{jk} \exp\left(i\beta_j^{\{q\}} \left(z_{q+1,q} - z_{q,q-1}\right)\right). \tag{3.24}$$

Expressions for $\mathbf{SR}_{3,1}$ and $\mathbf{ST}_{3,1}$ can be found in Appendix C.3.

The field coefficients in layer 2 can be expressed explicitly by using the original reflection and transmission matrices. Letting $\boldsymbol{A}^{\{2\}}$ and $\boldsymbol{B}^{\{2\}}$ denote vectors containing the coefficients $A_j^{\{2\}}$ and $B_j^{\{2\}}$, respectively, for $j = 1, 2, \ldots, N$, the following relations, that are derived in Appendix C.4, hold:

$$\boldsymbol{A}^{\{2\}} = \left(\mathbf{I} - \mathbf{R}_{2,1}\mathbf{P}_2\mathbf{R}_{2,3}\mathbf{P}_2\right)^{-1} \left(\mathbf{T}_{1,2}\tilde{\boldsymbol{A}}^{\{1\}} + \mathbf{R}_{2,1}\mathbf{P}_2\mathbf{T}_{3,2}\tilde{\boldsymbol{B}}^{\{3\}}\right), \tag{3.25a}$$

$$\boldsymbol{B}^{\{2\}} = \left(\mathbf{I} - \mathbf{R}_{2,3}\mathbf{P}_2\mathbf{R}_{2,1}\mathbf{P}_2\right)^{-1} \left(\mathbf{R}_{2,3}\mathbf{P}_2\mathbf{T}_{1,2}\tilde{\boldsymbol{A}}^{\{1\}} + \mathbf{T}_{3,2}\tilde{\boldsymbol{B}}^{\{3\}}\right), \tag{3.25b}$$

where $\tilde{\boldsymbol{A}}^{\{1\}}$ and $\tilde{\boldsymbol{B}}^{\{3\}}$ denote propagated versions of the corresponding coefficient vectors $\boldsymbol{A}^{\{1\}}$ and $\boldsymbol{B}^{\{3\}}$, such that the elements of $\tilde{\boldsymbol{A}}^{\{1\}}$ and $\tilde{\boldsymbol{B}}^{\{3\}}$ are:

$$\tilde{A}_j^{\{1\}} = A_j^{\{1\}} \exp\left(i\beta_j^{\{1\}} \left(z_{1,2} - z_{0,1}\right)\right), \tag{3.26a}$$

$$\tilde{B}_j^{\{3\}} = B_j^{\{3\}} \exp\left(i\beta_j^{\{3\}} \left(z_{3,4} - z_{2,3}\right)\right), \tag{3.26b}$$

for $j = 1, 2, \ldots, N$.

Multi-Layer Structure

This section will introduce the final step necessary to describe a general multi-layer structure with a total of $Q \geq 4$ layers. The initial and primary aim is to determine scattering matrices between the first layer and the last layer. To obtain these matrices, an iterative scheme whose fundamental idea is summarized below and in Fig. 3.10 is employed:

1. Compute the transmission and reflection matrices between all layers, such that $\mathbf{R}_{q,q+1}$, $\mathbf{R}_{q+1,q}$, $\mathbf{T}_{q,q+1}$ and $\mathbf{T}_{q+1,q}$ are obtained $\forall q \in [1, Q-1]$, that is, for all interfaces.

2. Reduce the multi-layer structure to its first three layers. Compute scattering matrices $\mathbf{SR}_{1,3}$, $\mathbf{SR}_{3,1}$, $\mathbf{ST}_{1,3}$ and $\mathbf{ST}_{3,1}$ for this system.

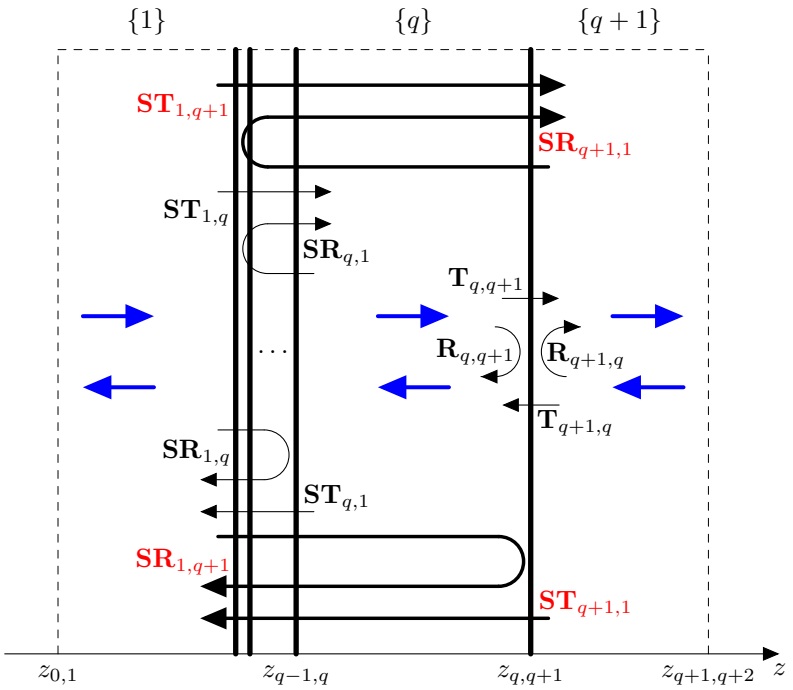

Figure 3.10 Iterative scheme in which scattering matrices to and from the $q+1$th layer are determined. The layers between the first and the qth interface are collapsed such that a reduced three-layer structure can be considered. Any layer after the $q+1$th layer is ignored.

3. Consider the fourth layer. By using the previously computed scattering matrices as a starting point for an iteration, and by following the idea outlined in Fig. 3.10, it is possible to determine the matrices $\mathbf{SR}_{1,4}$, $\mathbf{SR}_{4,1}$, $\mathbf{ST}_{1,4}$ and $\mathbf{ST}_{4,1}$.

4. Repeat step 3 by once again reducing the system to a three-layer system. Continuing in this manner, the scattering matrices $\mathbf{SR}_{1,q}$, $\mathbf{SR}_{q,1}$, $\mathbf{ST}_{1,q}$ and $\mathbf{ST}_{q,1}$ can be obtained for $q+1=4$ to $q+1=Q$.

The final iteration determines the reflection and transmission through the entire multi-layer structure, that is, the scattering matrices $\mathbf{SR}_{1,Q}$, $\mathbf{SR}_{Q,1}$, $\mathbf{ST}_{1,Q}$ and $\mathbf{ST}_{Q,1}$ are determined. The expressions needed to compute the $q+1$th scattering matrices are derived in Appendix C.4 and given below:

$$\mathbf{SR}_{1,q+1} = \mathbf{SR}_{1,q} + \mathbf{ST}_{q,1}\mathbf{P}_q\mathbf{R}_{q,q+1}\mathbf{P}_q \left(\mathbf{I} - \mathbf{SR}_{q,1}\mathbf{P}_q\mathbf{R}_{q,q+1}\mathbf{P}_q\right)^{-1} \mathbf{ST}_{1,q}, \tag{3.27a}$$

$$\mathbf{SR}_{q+1,1} = \mathbf{R}_{q+1,q} + \mathbf{T}_{q,q+1}\mathbf{P}_q\mathbf{SR}_{q,1}\mathbf{P}_q \left(\mathbf{I} - \mathbf{R}_{q,q+1}\mathbf{P}_q\mathbf{SR}_{q,1}\mathbf{P}_q\right)^{-1} \mathbf{T}_{q+1,q}, \tag{3.27b}$$

$$\mathbf{ST}_{1,q+1} = \mathbf{T}_{q,q+1}\mathbf{P}_q \left(\mathbf{I} - \mathbf{SR}_{q,1}\mathbf{P}_q\mathbf{R}_{q,1+1}\mathbf{P}_q\right)^{-1} \mathbf{ST}_{1,q}, \tag{3.27c}$$

$$\mathbf{ST}_{q+1,1} = \mathbf{ST}_{q,1}\mathbf{P}_q \left(\mathbf{I} - \mathbf{R}_{q,q+1}\mathbf{P}_q\mathbf{SR}_{q,1}\mathbf{P}_q\right)^{-1} \mathbf{T}_{q+1,q}. \tag{3.27d}$$

At this point, when comparing the above expressions with those for the scattering matrices $\mathbf{SR}_{1,3}$, $\mathbf{SR}_{3,1}$, $\mathbf{ST}_{1,3}$ and $\mathbf{ST}_{3,1}$ (Eqs. (3.23) and Eqs. (C.16) in Appendix C.3), it is seen that step 2 can be included in step 3 in the iterative scheme. One must then use the starting point of the pseudo-scattering matrices $\mathbf{SR}_{1,2} \equiv \mathbf{R}_{1,2}$, $\mathbf{SR}_{2,1} \equiv \mathbf{R}_{2,1}$,

$\mathbf{ST}_{1,2} \equiv \mathbf{T}_{1,2}$ and $\mathbf{ST}_{2,1} \equiv \mathbf{T}_{2,1}$. The derivations of Eqs. (3.27) follow the same procedure as the derivations of the scattering matrices of a three-layer system, see Appendix C.4, with the exception that the reflection and transmission matrices of the collapsed layers are scattering matrices.

In order to obtain the full field profile in all layers, it is necessary to express the field coefficients $\boldsymbol{A}^{\{q\}}$ and $\boldsymbol{B}^{\{q\}}$ for $q = 1, 2, \ldots, Q$. The coefficients for the outer layers, that is, $q = 1$ and $q = N$, are given directly from the knowledge of the scattering matrices from layer 1 to Q. The remaining coefficients for the inner layers ($q = 2, 3, \ldots, Q-1$) can be determined from the intermediate scattering matrices via:

$$\boldsymbol{A}^{\{q\}} = \left(\mathbf{I} - \mathbf{SR}_{q,1}\mathbf{P}_q\mathbf{SR}_{q,Q}\mathbf{P}_q\right)^{-1}\left(\mathbf{ST}_{1,q}\tilde{\boldsymbol{A}}^{\{1\}} + \mathbf{SR}_{q,1}\mathbf{P}_q\mathbf{ST}_{Q,q}\tilde{\boldsymbol{B}}^{\{Q\}}\right), \tag{3.28a}$$

$$\boldsymbol{B}^{\{q\}} = \left(\mathbf{I} - \mathbf{SR}_{q,Q}\mathbf{P}_q\mathbf{SR}_{1,q}\mathbf{P}_q\right)^{-1}\left(\mathbf{SR}_{q,Q}\mathbf{P}_q\mathbf{ST}_{1,q}\tilde{\boldsymbol{A}}^{\{1\}} + \mathbf{ST}_{Q,q}\tilde{\boldsymbol{B}}^{\{Q\}}\right), \tag{3.28b}$$

where $\tilde{\boldsymbol{A}}^{\{1\}}$ and $\tilde{\boldsymbol{B}}^{\{Q\}}$ denote propagated versions of the corresponding coefficient vectors, $\boldsymbol{A}^{\{1\}}$ and $\boldsymbol{B}^{\{Q\}}$, in a manner similar to that indicated in Eqs. (3.26). The derivation of these formulae can be seen in Appendix C.5. Observing the expressions for the field coefficients, it is apparent that a second iterative scheme must be employed to compute the scattering matrices from the last layer, Q, and inwards to $q-1$. The scheme is essentially identical to that described on p. 23, and the expressions for $\mathbf{SR}_{q-1,Q}$, $\mathbf{SR}_{Q,q-1}$, $\mathbf{ST}_{q-1,Q}$ and $\mathbf{ST}_{Q,q-1}$ can be seen in Appendix C.6.

In Sections 3.2-3.6, the formalism that determines the eigenmodes from the x-BCs, expands the entire 2D-field on these eigenmodes and couples the fields in different layers has been established. The sum of these efforts allows determination of the field profiles in a variety of geometries, including Bragg-gratings and micro-cavities, that are presented and discussed in the following section.

3.7 Field Profiles

Implementing the theory of the preceding sections in MATLAB allows determination of the field profile of any multi-layered structure. A general implementation requires some care and consideration, but yields a powerful tool that allows calculation of the electric field in a wide variety of structures in a closed geometry. This section demonstrates the functionality of such a general implementation by presenting a range of field profiles for different and increasingly complex structures.

The field profile of a certain geometry depends critically on the choice of incident fields at the first and the last z-interface. To display the field profiles, it is hence required to fix these initial conditions. For convenience, it is chosen that the first layer is illuminated by the fundamental mode of that layer. Other and more advanced initial condition are also possible: For instance, the illuminating wave could be a square wave along x. Constructing such a square wave can be achieved by expanding the square wave on the set of eigenmodes of the first layer, in a manner similar to that applied in Fourier series.

The field $E(x, z)$ represents a surface in a three dimensional space. It is beneficial to present such fields as two dimensional color-plots where the value of $E(x, z)$ is plotted on a color-scale. This allows for a precise and less cluttered representation of the fields, compared to a surface-plot. The arbitrary color-scale employed for the field plots is illustrated below:

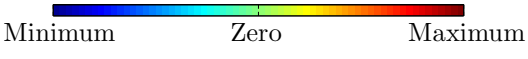

The values of the field are of no significance as these values scale with the normalization, and therefore only the relationship between values are of interest.

The structures to be studied are chosen as structures with refractive indices in the range $1 \leq n(x) \leq 2$, where it is noted that the numerical implementation is able to handle higher refractive indices. For illustrations of the refractive index profile, the following discrete gray color-scale is employed:

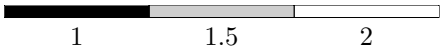

Finally, all field profiles in this section are computed with the inclusion of $N = 100$ eigenmodes as it is estimated that the field plots converge acceptably at this number of eigenmodes. Increasing the number of eigenmodes results in increased computing time, but minuscule changes in the field profiles.

The first subsection considers simple structures with few layers and simple x-variations. The second subsection considers an example of a multi-layered structure, specifically a Bragg grating, and briefly discusses how the step-index profiles can be applied to approximate oblique index profiles by use of a staircase approximation.

Simple structures

The first and most basic structure is that of a waveguide in a single layer. The index profile for the structure is illustrated in Fig. 3.11(a). No z-interfaces are present, and as a consequence a plot of the electric field, displayed in Fig. 3.11(b), shows nothing but the undisturbed fundamental mode propagating along a uniform waveguide, as dictated by its harmonic z-dependence.

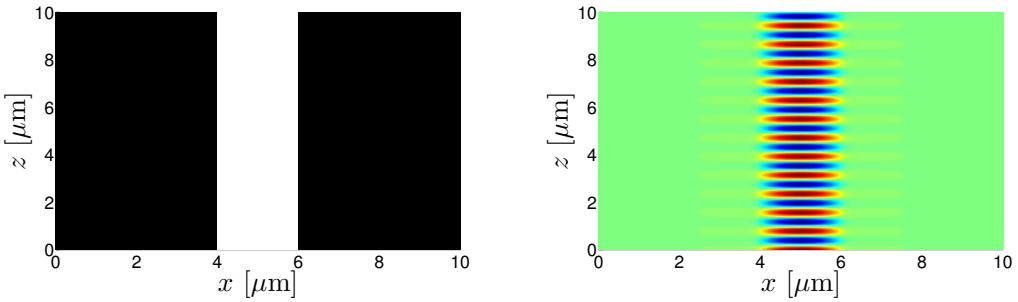

(a) Refractive index profile.

(b) Field Profile.

Figure 3.11 Electric field in waveguide: The waveguide is placed in vacuum, and the refractive index of the core is $n = 2$. The width of the core is $D_g = 2\,\mu$m, and the width of the closed geometry is $L_x = 10\,\mu$m.

An abruptly terminated waveguide can be considered by introducing a single z-interface. An example of such an abruptly terminated waveguide is displayed in Fig. 3.12(a), and the resulting field is shown in Fig. 3.12(b). The plot clearly displays a spreading of the guided mode upon exiting the waveguide into vacuum which is as expected. However, interference effects are also observed, contrary to what would be expected for such a structure. This effect is a direct consequence of the closed geometry approach: The x-boundaries of the closed geometry act as perfectly conducting walls that reflect the light light. Several

distinct interference patterns are observed in Fig. 3.12(b). This undesirable effect, referred to as parasitic reflections, is a fundamental limitation of the closed geometry approach.

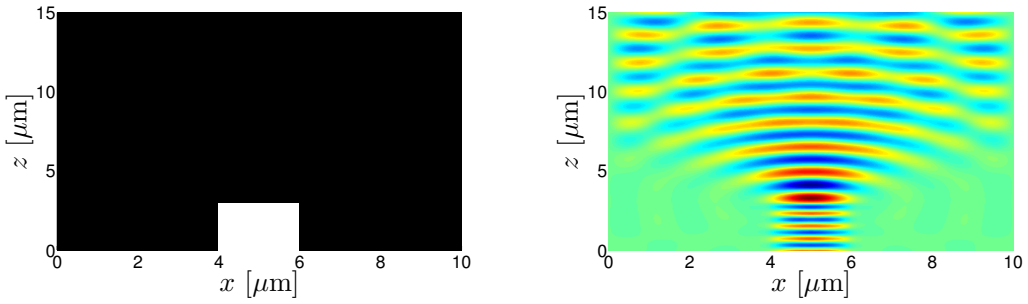

(a) Refractive index profile. (b) Field Profile.

Figure 3.12 Electric field in an abruptly terminated waveguide: The waveguide is placed in vacuum and emits light into vacuum. The refractive index of the core is $n = 2$. The width of the core is $D_g = 2\,\mu$m and $L_x = 10\,\mu$m.

The impact from the parasitic reflections scales directly with the size of the closed geometry, L_x. Figs. 3.13 display the results of two calculations of the electric field, both with refractive index profiles as in Fig. 3.12(a) and with a core width of $D_g = 2\,\mu$m, but with different values of L_x. The field profile in Fig. 3.13(a), with $L_x = 5\,\mu$m, is almost entirely dominated by the effects of parasitic reflections. Increasing the value of L_x to $20\,\mu$m, Fig. 3.13(b), results in a significant reduction of the effects in the observed z-range. From these results, it is reasonable to assume that the closed geometry would emulate an open geometry without x-boundaries for large values of L_x. Strictly, the effects of parasitic reflections remain when L_x is increased, but the region in which they dominate is displaced along the z-axis such that interference effects are not significant until at large z-values. Also, it should be noted that in the vicinity of the x-boundaries the parasitic reflections remain, but the relative impact from this throughout the structure has diminished.

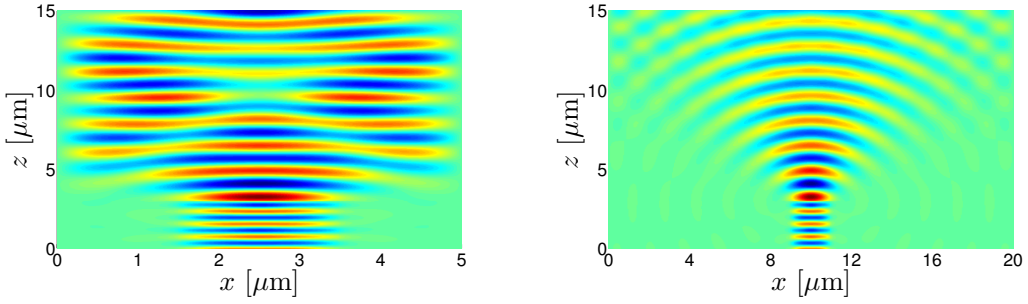

(a) $L_x = 5\,\mu$m. (b) $L_x = 20\,\mu$m.

Figure 3.13 Parasitic effects in an abruptly terminated waveguide. Both field plots represent abruptly terminated waveguides, similar to that in Fig. 3.12(a), but with different values of L_x.

Multi-layered structures

The multi-layer formalism is ideal for handling computations on constructions such as Bragg gratings in which multiple layers of alternating refractive index, n_1 and n_2, are positioned in succession. Such structures can exhibit high reflection for specific wavelengths. The optical path distance in each layer is defined as $\delta_1 = n_1 d_1$ and $\delta_2 = n_2 d_2$ where d_1 and d_2 denote the z-length of each layer. Designing the structure such that δ_1 and δ_2 both equal $\lambda/4$ yields a highly reflective grating [Pedrotti, Chapter 22-2]. Such an engineered structure is displayed in Fig. 3.14(a).

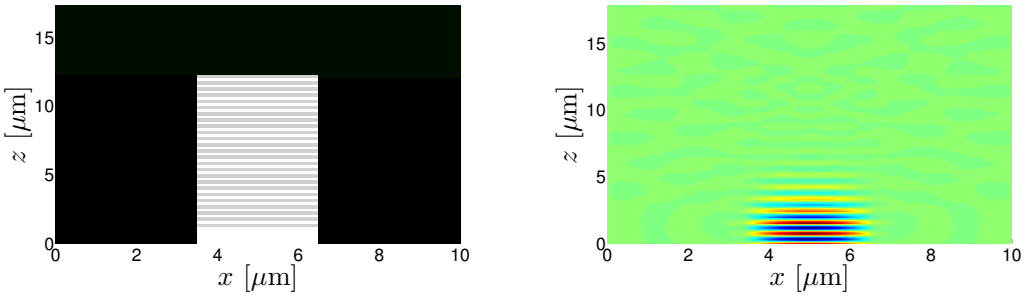

(a) Refractive index profile.

(b) Field Profile.

Figure 3.14 Electric field in a fiber in which a Bragg grating with the refractive indices $n_1 = 1.5$ and $n_2 = 2$ is inscribed. The thickness of each layer is determined such that $\delta_1 = \delta_2 = \lambda/4$ which yields $d_1 = 0.258\,\mu$m and $d_2 = 0.194\,\mu$m. The width of the fiber is set to $D_g = 3\,\mu$m. A total of 52 layers is included.

The field profile of the structure is shown in Fig. 3.14(b). That the structure is highly reflective is apparent from the strong attenuation of the field across the initial layers. As an example of the uses of Bragg gratings, micropillar cavities can be mentioned. Such cavities employ Bragg gratings as highly reflective and thin cavity mirrors. To illustrate that the reflective effect of a Bragg grating is strongly dependent on the wavelength, the structure in Fig. 3.14(a) is illuminated by the fundamental mode with a wavelength of $\lambda = 1.10\,\mu$m, differing from the previously used $\lambda = 1.55\,\mu$m. The resulting field profile is displayed in Fig. 3.15. The change in the profile, as compared to that in Fig. 3.14(b), is obvious as no attenuation of the field is visible.

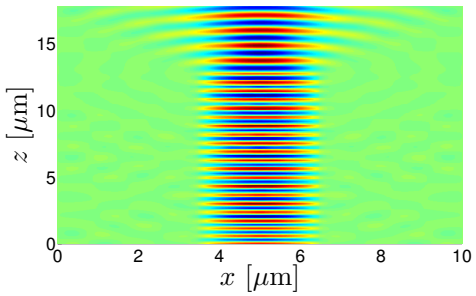

Figure 3.15 Field profile. Wavelength-dependence in Bragg gratings: Illumination of the Bragg grating, illustrated in Fig. 3.14(a), with the fundamental mode and with $\lambda = 1.10\,\mu$m. No attenuation is observed, in contrast to the results in Fig. 3.14(b).

Finally, simulation of oblique interface boundaries is discussed. Since the developed formalism can only handle square zones and layers, a staircase approximation can be used to simulate structures with oblique interfaces. As an example, the oblique interface between the core and vacuum of a narrowing fiber can be well approximated by dividing the oblique interface into a series of square staircase steps. The quality of the approximation is improved by increasing the number of staircase steps. An example of such a simulation is not shown as it is outside the focus of this report, but the description of the staircase approximation illustrates the versatility of the formalism.

3.8 Spontaneous Emission Rate

The spontaneous emission rate (SER), γ, is the rate of spontaneous emissions in a two-level system, such as a quantum emitter. Further discussion of the SER and the two-level system is out of the scope of this report, but instead reference is made to [Pedrotti, Chapter 6] and [Novotny, Chapter 8.4]. However, to obtain a quantitative measure that allows comparison of the closed and open geometry approaches, the SER will implicitly be determined through a calculation of the normalized SER, defined in the following.

The normalized SER, α, is defined as the the SER, γ, of some material in some structure relative to the SER in a uniform structure of the same material, γ_0:

$$\alpha \equiv \frac{\gamma}{\gamma_0}. \tag{3.29}$$

In words, α measures how much the SER has been increased or decreased for a given environment, relative to the SER in the bulk material. The normalized SER is interchangeable with the Purcell enhancement factor, used in the studies of microcavities [Purcell]. It can be shown that α is also given as the ratio of the power emitted from a current source in the optical environment, P, and the power emitted from the same current source in a uniform material, P_0 [Novotny, Eq. (8.138)]:

$$\alpha = \frac{P}{P_0}. \tag{3.30}$$

Hence, rather than calculating the SER, γ, and its corresponding reference value, γ_0, the power, P, and its reference value, P_0, may equally well be used to obtain α. Therefore, in the following sections the power resulting from a current source inside the structure is derived. The reference power, P_0, is that of a uniform material in an open geometry. The value is derived in Section 4.6, and the result in arbitrary units is:

$$P_0 = \frac{1}{8}. \tag{3.31}$$

It is noted that the reference power is independent of the choice of refractive index in the bulk material.

Modeling

The power radiated from a current source with harmonic time-dependence is given by [Novotny, Eq. (8.73)]:

$$P \equiv -\frac{1}{2}\int_V \mathrm{Re}(\mathbf{J}(\boldsymbol{r})^* \cdot \mathbf{E}(\boldsymbol{r}))\,\mathrm{d}\Omega, \tag{3.32}$$

where $\mathbf{J}(\boldsymbol{r})$ is the current density of an arbitrary current source, $\mathbf{E}(\boldsymbol{r})$ is the electric field resulting from this current source, and the integral is taken over a volume, V, that bounds the current source. For both the closed and open geometries, the current source is assumed harmonic in time and chosen as a dipole that can be modeled as a Dirac delta function positioned in the point $(x, z) = (x_c, 0)$, pointing along the y-direction and with magnitude J_0:

$$\mathbf{J}(\boldsymbol{r}) = J_0\delta(z)\delta(x - x_c)\,\hat{\boldsymbol{y}}. \tag{3.33}$$

For simplicity, the magnitude of the dipole is chosen as $J_0 = 1$ A/ m^2, and to maintain a simple notation the units are omitted in the following. Using this and assuming that the electric field due to the dipole is polarized along the y-direction, $\mathbf{E} = E(x, z)\,\hat{\boldsymbol{y}}$, the expression for the power reduces to:

$$\boxed{P = -\frac{1}{2}\int_V \mathrm{Re}(\delta(z)\delta(x - x_c)E(x, z))\,\mathrm{d}\Omega = -\frac{1}{2}\mathrm{Re}(E(x_c, 0)).} \tag{3.34}$$

Hence, the power is directly determined by computing the strength of the electric field in the point of the dipole. Consequently, to determine the power the electric field generated by the current source must first be evaluated.

Power in Single Layer Geometry

In this section, the electric field generated by the dipole current in a uniform layer will be derived, and the appertaining power will be expressed from this. The geometry is schematically illustrated in an xz-plane in Fig. 3.16. The current source, $\mathbf{J}$, is positioned at $z = 0$ pointing along the y-axis, and the volume that bounds the current source, V, is illustrated by the horizontal, dashed lines. Since the current source is modeled as a dipole of infinitesimal extent, this volume tends to zero which is not justified by the schematic representation. The parts of the field that propagate along the positive and negative z-directions, respectively, are indicated by the blue arrows.

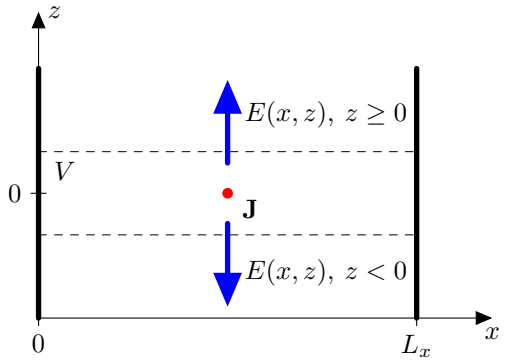

Figure 3.16 Schematic representation of dipole current, $\mathbf{J}$, in uniform layer. The volume that bounds the current source, V, and the parts of the electric field that propagate along the positive and negative z-directions, respectively, are indicated.

As discussed in Section 3.5, the electric field, $E(x, z)$, can be expanded on the

eigenmodes $e_{x,j}(x)$ and $\exp(\pm i\beta_j z)$ as follows:

$$E(x,z) = \begin{cases} \sum_{j=1}^{\infty} \mathcal{A}_j e_{x,j}(x) \exp(i\beta_j z), & z \geq 0, \\ \sum_{j=1}^{\infty} \mathcal{A}_j e_{x,j}(x) \exp(-i\beta_j z), & z < 0. \end{cases} \tag{3.35}$$

Since the source of the electric field is placed in $z = 0$, the field for $z \geq 0$ and $z < 0$ may only have z-dependent contributions that propagate along the positive and negative z-directions, respectively, as there are no interfaces to reflect the field. The electric field is determined once the modal amplitudes, $\mathcal{A}_j$, are obtained, and by the result in Eq. (3.34) this yields the emitted power. Qualitatively, any value of $\mathcal{A}_j$ is given as the projection of the jth eigenmode, $e_{x,j}$, on the current density, $\mathbf{J}$. The modal amplitudes are given as [Snyder, Eq. (31-35c)]:

$$\mathcal{A}_j = -\frac{1}{4N_j'} \int_{\mathcal{V}} \boldsymbol{e}_j(x)^* \cdot \mathbf{J}(\boldsymbol{r}) \exp(-i\beta_j z)\, \mathrm{d}\Omega, \tag{3.36}$$

where $\boldsymbol{e}_j = e_{x,j}\, \hat{\boldsymbol{y}}$, and where the integral is taken over the volume, $\mathcal{V}$, that bounds the dot product of the (vectorial) eigenmode, $\boldsymbol{e}_j$, and the current source, $\mathbf{J}$. The expression in Eq. (3.36) is valid when the eigenmodes satisfy the orthonormality relation in Eq. (3.9) which accounts for the use of the Power inner product. Also, it must be noted that at this point the eigenmodes are assumed normalized which by Eq. (3.8) gives $N_j' = \beta_j^*/|\beta_j|$. Given the dipole nature of the current source in Eq. (3.33), the modal amplitudes are evaluated as:

$$\mathcal{A}_j = -\frac{|\beta_j|}{4\beta_j^*} e_{x,j}(x_c)^*. \tag{3.37}$$

Introducing these coefficients in Eq. (3.35), the fields on either side of the dipole position at $z = 0$ become:

$$E(x,z) = -\sum_{j=1}^{\infty} \frac{|\beta_j|}{4\beta_j^*} e_{x,j}(x_c)^* e_{x,j}(x) \begin{cases} \exp(i\beta_j z), & z \geq 0, \\ \exp(-i\beta_j z), & z < 0. \end{cases} \tag{3.38}$$

Having expressed the field resulting from the dipole current, the power can be written out explicitly by use of Eq. (3.34):

$$P = \frac{1}{8} \sum_{j=1}^{\infty} |e_{x,j}(x_c)|^2 \,\mathrm{Re}\left(\frac{|\beta_j|}{\beta_j^*}\right). \tag{3.39}$$

When $\beta_j^2 < 0$, the term $\mathrm{Re}\left(|\beta_j|/\beta_j^*\right)$ equals zero, and therefore the infinite sum reduces to a finite sum over the eigenmodes with real β_j-values. This means that only propagating waves contribute to the emitted power, and with no approximation the sum can be truncated to yield:

$$\boxed{P = \frac{1}{8} \sum_{j=1}^{M} |e_{x,j}(x_c)|^2,} \tag{3.40}$$

where M denotes the last eigenmode with a real z-propagation constant, such that $\beta_M^2 > 0$ and $\beta_{M+1}^2 < 0$.

Power in Three-Layer Geometry

In this section, the dipole is assumed positioned in a layer that is surrounded by two arbitrary layers. The resulting field must then comprise contributions from the multiple reflections of the field that take place at the layer interfaces between the center layer and the surrounding layers. The setup is schematically illustrated in an xz-plane in Fig. 3.17. The layer containing the dipole is not depicted as any specific layer because the following derivations hold for an arbitrary dipole layer as well as arbitrary surrounding layers.

The derivations in this section are inspired by the outline in [Bienstman, Chapter 7].

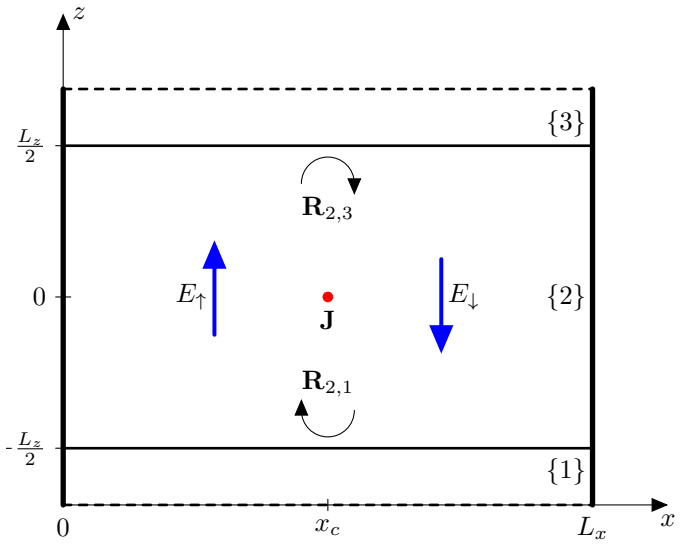

Figure 3.17 Schematic representation of a dipole current, $\mathbf{J}$, in a layer that is surrounded by two arbitrary layers. At the respective z-boundaries the reflection matrices are $\mathbf{R}_{2,1}$ and $\mathbf{R}_{2,3}$, and the parts of the field that propagate along the positive and negative z-direction, $E_\uparrow$ and $E_\downarrow$, respectively, are represented by the blue arrows.

By the general result in Eq. (3.34), the field must be determined as a function of x in $z = 0$. As in the case of a uniform layer, the dipole initially generates contributions to the field that propagate along the positive and negative z-direction, respectively. At the interfaces each of these contributions are partially transmitted and partially reflected, and the parts that are reflected return to the $z = 0$ plane and contribute to the total field. Next, they propagate to the opposite interfaces, are partially transmitted and partially reflected, and the reflected parts again contribute to the total field. These reflections, in principle, continue indefinitely. Terming the parts of the field that propagate along the positive and negative z-direction, at $z = 0$, $E^\uparrow(x, 0)$ and $E^\downarrow(x, 0)$, respectively, the total field, $E(x, 0)$, is:

$$E(x, 0) = E^\uparrow(x, 0) + E^\downarrow(x, 0). \tag{3.41}$$

The contributions to $E^\uparrow$ and $E^\downarrow$, respectively, are the sums of the contributions from each of the modes, and using the property of uniform convergence from Eq. (3.14) the infinite

series are truncated at N, the number of modes included in the numerical computations:

$$E_{\uparrow}(x,0) = \sum_{j=1}^{\infty} \epsilon_j^{\uparrow} e_{x,j}(x) \simeq \sum_{j=1}^{N} \epsilon_j^{\uparrow} e_{x,j}(x), \tag{3.42a}$$

$$E_{\downarrow}(x,0) = \sum_{j=1}^{\infty} \epsilon_j^{\downarrow} e_{x,j}(x) \simeq \sum_{j=1}^{N} \epsilon_j^{\downarrow} e_{x,j}(x). \tag{3.42b}$$

This truncation allows representation of the contribution coefficients as vectors via: $\boldsymbol{\epsilon}^{\uparrow} = [\epsilon_1^{\uparrow}\, \epsilon_2^{\uparrow} \ldots \epsilon_N^{\uparrow}]^T$ and $\boldsymbol{\epsilon}^{\downarrow} = [\epsilon_1^{\downarrow}\, \epsilon_2^{\downarrow} \ldots \epsilon_N^{\downarrow}]^T$. These are termed contribution vectors and are determined in Appendix C.7. To keep a simple notation, the approximate equality signs in Eqs. (3.42) are replaced by equality signs in the following.

Applying the definitions in Eqs. (3.41) and (3.42), allows representation of the field at $z = 0$ in the following manner:

$$E(x,0) = \sum_{j=1}^{N} (\epsilon_j^{\uparrow} + \epsilon_j^{\downarrow}) e_{x,j}(x). \tag{3.43}$$

Before writing down the final expression, the sum of $\boldsymbol{\epsilon}^{\uparrow}$ and $\boldsymbol{\epsilon}^{\downarrow}$ is expressed from the results in Appendix C.7, Eqs. (C.24) and (C.25):

$$\begin{aligned} \boldsymbol{\epsilon}^{\uparrow} + \boldsymbol{\epsilon}^{\downarrow} &= (\mathbf{I} - \mathbf{R}_{\mathrm{bot}}\mathbf{R}_{\mathrm{top}})^{-1}(\mathbf{I} + \mathbf{R}_{\mathrm{bot}})\boldsymbol{\mathcal{A}} + (\mathbf{I} - \mathbf{R}_{\mathrm{top}}\mathbf{R}_{\mathrm{bot}})^{-1}\mathbf{R}_{\mathrm{top}}(\mathbf{I} + \mathbf{R}_{\mathrm{bot}})\boldsymbol{\mathcal{A}} \\ &= \left[(\mathbf{I} - \mathbf{R}_{\mathrm{bot}}\mathbf{R}_{\mathrm{top}})^{-1} + (\mathbf{I} - \mathbf{R}_{\mathrm{top}}\mathbf{R}_{\mathrm{bot}})^{-1}\mathbf{R}_{\mathrm{top}}\right](\mathbf{I} + \mathbf{R}_{\mathrm{bot}})\boldsymbol{\mathcal{A}} \\ &\equiv \mathbf{S}\boldsymbol{\mathcal{A}}. \end{aligned} \tag{3.44}$$

where $\boldsymbol{\mathcal{A}} = [\mathcal{A}_1, \mathcal{A}_2, \ldots, \mathcal{A}_N]^T$, with $\mathcal{A}_j$ given as in Eq. (3.37), and the matrices $\mathbf{R}_{\mathrm{top}}$ and $\mathbf{R}_{\mathrm{bot}}$, which handle the effects of propagation to and reflection from the top and bottom interfaces, respectively, are given in Eqs. (C.21). The matrix $\mathbf{S}$, introduced to ensure a concise and brief notation, describes the action of the surrounding layers on the field in the center layer.

Combining Eqs. (3.43) and (3.44) finally gives the field:

$$E(x,0) = \sum_{k=1}^{N} \sum_{j=1}^{N} S_{k,j} \mathcal{A}_j e_{x,j}, \tag{3.45}$$

where $S_{k,j}$ is the element in the kth row and jth column of the matrix $\mathbf{S}$. Having expressed the field in the $z = 0$ plane, the emitted power may be expressed by using the result in Eq. (3.34) and the expression for the modal amplitudes, $\mathcal{A}_j$, in Eq. (3.37):

$$\boxed{P = \frac{1}{8} \sum_{k=1}^{N} \sum_{j=1}^{N} |e_{x,j}(x_c)|^2 \mathrm{Re}\left(S_{k,j} \frac{|\beta_j|}{\beta_j^*} \right).} \tag{3.46}$$

Contrary to the result for the single-layer geometry, evanescent modes may now contribute to the emitted power through the action of the elements of the matrix $\mathbf{S}$. This is a consequence of the introduction of interfaces that allow an emitted evanescent mode to couple to propagating modes at the interface, and thus to contribute to the total emitted power. Due to this, all modes must in principle be included in the calculation of P. Consequently, it is not obvious how the number of modes, N, must be chosen to

ensure a specific and small truncation error. Hence, before computing the power ratios in the three-layer geometries, convergence studies that determine the number of modes to include are carried out, see Appendix C.8.

The expression for the power can easily be generalized to the case where the dipole layer is surrounded by multiple layers on both sides. This can be done by replacing the reflection matrices by the scattering matrices, **SR**, that were introduced in Section 3.6. Fundamentally, these scattering matrices describe the amount of reflection from all of the layers above and below the dipole layer, respectively, and the transitions from the reflection matrices to the scattering matrices in the derivations are therefore straightforward.

Computational Results

Using the expressions derived in the preceding sections, the power will be determined for different single-layer and three-layer geometries. In all cases, the power is computed for different values of the width of the geometry along the x-direction, L_x, and the range of values for this parameter will be:

$$L_x \in [6.00\,\mu\text{m}, 6.05\,\mu\text{m}, 6.10\,\mu\text{m}, \ldots, 30.0\,\mu\text{m}]. \tag{3.47}$$

Having chosen the values in Eq. (3.47), a total of 481 data points will be obtained for each geometry. The range in Eq. (3.47) could be extended, but since larger values of L_x require inclusion of more modes, this increases the computation time. Obviously, in this 2D-problem additional modes could be included at no unreasonable increase in computation time. However, investigations of more realistic and complicated structures that require a full 3D-treatment would likely suffer an unacceptable increase in computation time, in order to attain acceptably convergent results. Thus, to evaluate the convergence speed in a range of L_x-values viable for realistic structures, a maximum value of $L_x = 30\,\mu$m is chosen. At this width, the normalized SER should have converged acceptably to deem the procedure successful.

Single-Layer Geometry

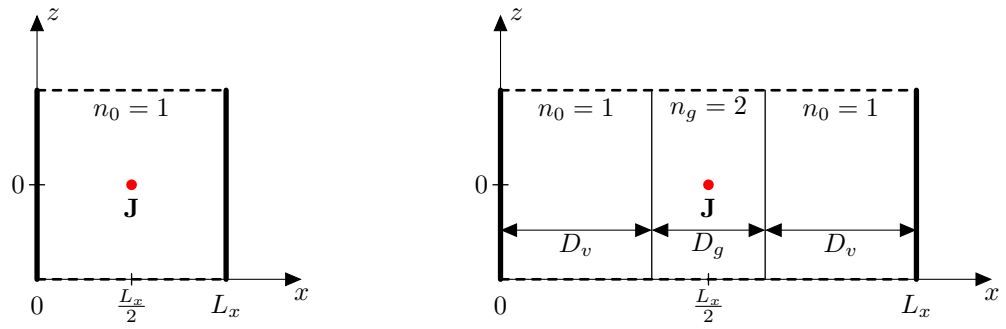

(a) Vacuum layer.

(b) Symmetric waveguide layer.

Figure 3.18 Dipole current, **J**, in single-layer, closed geometries for which the power ratio, α, is calculated as function of the width of the layer, L_x.

The power is in this section calculated for geometries where the dipole is situated in geometries with uniformity along z, that is, in single-layers. Specifically, a uniform

vacuum layer and a symmetric waveguide layer will be investigated. Obviously, in the vacuum layer the refractive index is everywhere $n = n_0 = 1$, and therefore the only variable parameter in describing this system is the width of the layer, L_x. In the guide layer, a guide region of fixed width, $D_g = 2\,\mu$m, is positioned symmetrically between two vacuum regions, the cladding regions, each of width $D_v = (L_x - D_g)/2$. The refractive index in the core of the waveguide is chosen as $n_g = 2$. Finally, the dipole is placed in the middle of the core, $x_c = L_x/2$. The vacuum layer and the waveguide layer geometries are illustrated in Figs. 3.18(a) and 3.18(b), respectively. The thick, vertical lines indicate the outer x-boundaries, whereas the thin, vertical lines indicate the separation of different regions. The horizontal dashed lines indicate the z-boundaries that are of no significance in the case of a single-layer, but included for consistency.

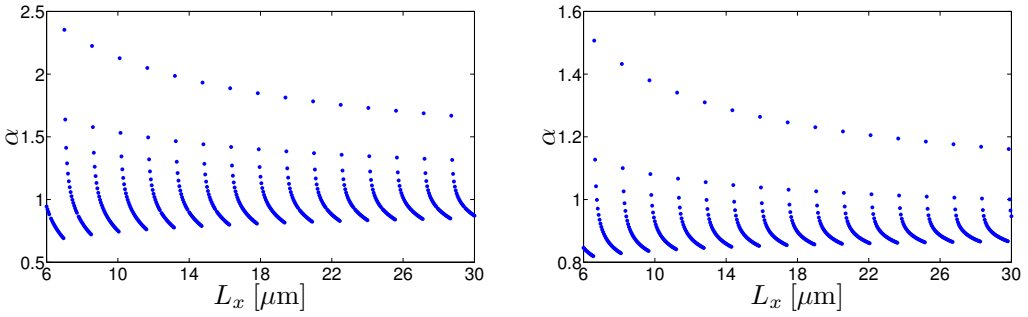

(a) Vacuum layer.

(b) Symmetric waveguide layer.

Figure 3.19 Power ratio, $\alpha = P/P_0$, as function of the width of the geometry along x, L_x, for closed, single-layer geometries.

Fig. 3.19(a) displays the power ratio, $\alpha = P/P_0$, for a vacuum layer of width L_x. The ratio ranges approximately from 0.7 to 2.5, but the density of data points in the range from $\alpha \approx 0.7$ to $\alpha \approx 1.2$ is much larger than for higher values of α. Estimating an average value in this range as $\alpha_{\text{av}} = 0.95$, the relative fluctuations of the points are approximately $\delta\alpha = (1.2 - 0.95)/0.95 = 0.26$. Generally, the power ratio is periodic with L_x, repeating itself for approximately every $\delta L_x = 1.5\,\mu$m. However, the largest and the smallest values in each cycle decreases and increases, respectively, indicating a decrease in the variation of α as L_x increases.

In Fig. 3.19(b), the power ratio as function of L_x for the symmetric waveguide layer is shown. Qualitatively, these data points are identical to the vacuum layer results, but the range of values for α is smaller: approximately from 0.8 to 1.5. The largest density of data points is found for values of α that are equal to or smaller than unity which differs slightly from the results for the vacuum layer. Estimating again an average value as $\alpha_{av} = 0.90$, the relative fluctuations of the points are approximately $\delta\alpha = (1.0 - 0.90)/0.90 = 0.11$. This smaller deviation compared to the vacuum layer can be accounted for by the inclusion of guided modes in the waveguide layer. As will be discussed in the following paragraph and in Chapter 4, the fluctuating pattern is largely the result of contributions from the semi-radiating modes, and thus inclusion of guided modes is expected to diminish the fluctuations. The repetition length is again approximately $\delta L_x = 1.5\,\mu$m, and the variation of the power ratio decreases as L_x is increased.

In the following, the oscillating pattern in the SER plots is examined and explained. Firstly, it is noticed that the repetition length equals the applied wavelength, namely

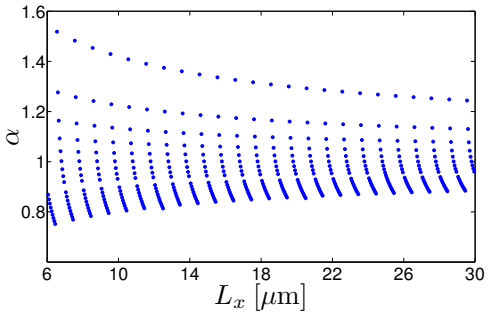

(a) Vacuum layer. $\lambda = 1.00\,\mu$m.

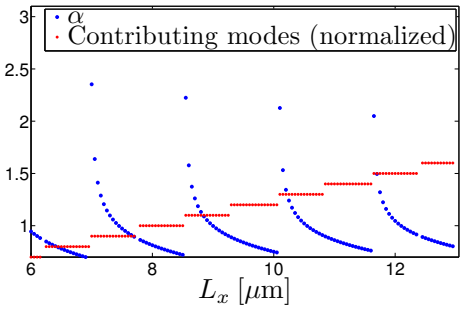

(b) Vacuum layer. $\lambda = 1.55\,\mu$m. Power ratio (blue) and normalized number of contributing modes, both as functions of L_x.

Figure 3.20 Plots used in analyzing the (L_x, α)-plots.

$\delta L_x \approx \lambda$, which can be verified by computing the power ratios for a different wavelength. This has been carried out for the vacuum layer with $\lambda = 1.00\,\mu$m, and the results can be seen in Fig. 3.20(a). It is registered that the repetition length, as expected, is $\delta L_x \approx 1.0\,\mu$m. That the repetition length is in fact the wavelength can be explained in terms of the contributing semi-radiating modes. At a specific width, L_x, a number of semi-radiating modes contributes to the power ratio, c.f. Eq. (3.40), that is, a number of semi-radiating modes have real z-propagation constants. As the width is increased, the normalization of the eigenmodes decreases the contribution from each semi-radiating mode which explains the decrease of α. However, when L_x is increased by one wavelength, two additional modes, one odd and one even mode, are included in the real β_j-range, and thus two additional semi-radiating modes are included in the sum in Eq. (3.40). The contribution from each mode is proportional to the absolute square of the mode evaluated in the point where the dipole is positioned. Since the dipole is situated exactly in the middle of the layer, the odd modes consequently do not contribute, and this explains why the periodic increases of α occur once for every wavelength: Inclusion of additional even modes increases the power ratio while inclusion of additional odd modes does not contribute. This is illustrated in Fig. 3.20(b) where the power ratio for the vacuum layer with $\lambda = 1.55\,\mu$m (blue) and the number of contributing modes (red), normalized so that the values approximately equal the values of the power ratios (in this case: divided by 10), are plotted. As expected, the number of contributing modes increases twice for every cycle of the power ratio. Obviously, the guided modes also contribute to α, but their contribution to the power ratio is roughly independent of L_x.

One way of describing the data points for both of the single layer geometries is as damped oscillators. However, the damping is small, and the overall picture is that the power ratios do not converge in any of the geometries due to the critical dependence on L_x. This consequently illustrates the limitations of the closed geometry.

Three-Layer Geometry

The waveguide layer that was examined in the single layer geometry in the preceding section is now assumed surrounded by two vacuums layers, and two core refractive indices are considered, namely $n_g = 1.1$ and $n_g = 2.0$. The thickness of the guide layer, relevant for the propagation matrix, $\mathbf{P}$, used in the general result in Eq. (3.46), is $L_z = 2\,\mu$m. The

geometry is illustrated in Fig. 3.21.

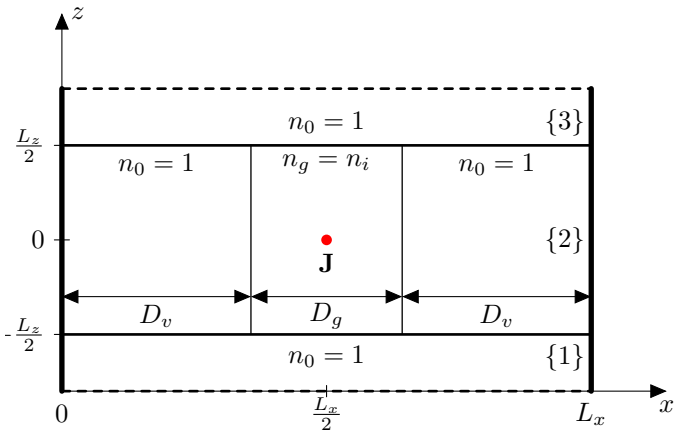

Figure 3.21 Dipole current, **J**, in three-layer closed geometry for which the power ratio, α, is calculated as function of the width of the layers, L_x. The refractive index of the core region is denoted n_g.

As earlier discussed, the number of modes to be included must be determined such that the truncation error for any n_g is smaller than a tolerance. A convergence study of the N-dependence is carried out in Appendix C.8, and the required number of modes to obtain a deviation of less than 1 permille is estimated as $N \geq 85$.

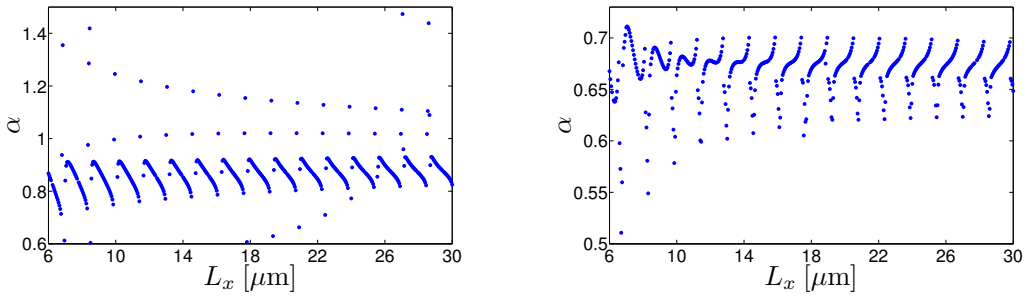

(a) $n_g = 1.1$. (b) $n_g = 2$.

Figure 3.22 Power ratios, α, as function of width of geometry along x, L_x, for a closed, three-layer geometry for two values of the refractive index in the core, n_g.

In Fig. 3.22(a), the power ratio as function of L_x for $n_g = 1.1$ can be seen. The results exhibit the same periodicity with the wavelength, $\delta L_x \approx \lambda$, as for the single-layer geometries. However, the shape of the data points is slightly different, and also more noise is observed, as compared to the single-layer geometries: More data points fall out of the general oscillating pattern. The majority of the points have values of α between 0.7 and 1, and the damping of the range of values of α for increasing L_x is observed, but the value of the power ratio does not converge. Estimating an average value as $\alpha_{av} = 0.85$, the relative fluctuations are then approximately $\delta\alpha = (1.0 - 0.85)/0.85 = 0.18$. For $n_g = 1.1$, the three-layer geometry is only slightly perturbed compared to the single-layer vacuum

geometry, and therefore a more clear resemblance between the results in Figs. 3.20(a) and 3.22(a) could have been expected. It should be noted that to focus on the main features of the data points, the points with $\alpha > 1.5$ have been ignored since they are considered as numerical noise.

In Fig. 3.22(b), the power ratios as functions of L_x for $n_g = 2.0$ can be seen. The periodicity with $\delta L_x \approx \lambda$ is observed, but the pattern of the data points differs in a significant way as compared to the previously obtained results: the power ratio increases during one cycle and then discontinuously decreases. This is exactly the opposite of what was observed in Fig. 3.20(b), where the power ratio, due to the normalization, decreased during one cycle and then increased discontinuously when an even mode was added. The range of values for α is smaller than what has previously been observed, being for the largest part in the range from 0.6 to 0.7. Estimating the average value as $\alpha_{av} = 0.65$, the relative fluctuations are then approximately $\delta\alpha = (0.7 - 0.65)/0.65 = 0.08$. This smaller deviation must again be accounted for by the presence and contributions from guided modes in the structure. The damping of the range of values for α for increasing L_x is less pronounced as compared to the previous results, but the power ratio does not converge. Again, it is noted that a few data points with $\alpha > 0.75$ have been omitted as they are considered noise.

As was the case for the single-layer geometries in the previous section, the power emitted from the dipole in the three-layer geometries does not converge in the examined L_x range and does not promise convergence at higher values of L_x. This accentuates the conclusion that the closed geometry approach is critically dependent on the width of the geometry which exposes the limitations of this method.

3.9 Summary

This chapter has presented a first and relatively simple approach to simulating the electric field in a slab structure. The main characteristic of this approach is that the geometry is given a finite width along x outside which the field is forced to vanish. This condition and the demand for continuity and differentiability of the field in all x inside the geometry define the x-BCs from which the eigenmodes were determined using the semi-analytical approach. Having determined the eigenmodes, these were normalized with respect to the Power inner product which later in the chapter proved to facilitate the calculation of the power emitted from a dipole situated inside the geometry. The requirement of continuity and differentiability of the field along z was treated by the scattering matrix formalism. In brief, this formalism relates the field expansion coefficients, that are used when the electric field is expanded on the x-dependent eigenmodes, in different layers along z.

With the above implemented in MATLAB, field profiles can be determined for arbitrary step-index profiles consisting of multiple layers. To demonstrate this, different geometries were defined and the corresponding field profiles were presented and discussed. These field profiles uncovered the first and primary limitation of the closed geometry approach: Parasitic reflections, caused by the perfectly conducting walls at the outer x-boundaries. Widening the geometry along x diminished the relative effect from these parasitic reflections, and this therefore provided the first argument for the open geometry approach, treated in the following chapters. The open geometry approach is essentially the limiting case of the closed geometry when the width along x approaches infinity. Despite the parasitic reflections, plots of the field profiles in the closed geometry provided qualitatively good representations of the field propagation in the examined geometries.

Finally, the normalized SER was implicitly determined by calculating the corresponding

normalized power emitted from a dipole in the geometries. The normalized SER provides a quantitative measure for comparison of the closed and open geometry approaches. In the closed geometry approach, it was calculated as function of the width of the geometry, and the results from multiple single- and three-layer geometries all yielded the same conclusion: The value of the normalized SER was critically dependent on the width of the geometry. The relative fluctuation of the normalized SER was in the range from 8% to 26%, and hence no reliable values could be obtained with the closed geometry approach. This and the parasitic reflections in the field profiles proved that another approach that more precisely models the actual slab structure is needed: The open geometry approach, treated in the following chapters.

Chapter 4

Open Geometry: Single-Layer

4.1 Introduction

In the preceding chapter, theory and results for the closed geometry approach were presented, and the results, namely the field profiles and the power ratios as functions of the width of the geometry, made the limitations of this approach clear. Therefore, in this and the following chapters the open geometry approach will be discussed and analyzed, and specifically the results from this approach will be compared with the corresponding results from the closed geometry approach.

The defining difference between the closed and open geometry approaches is that in the open geometry approach the geometry is assumed to extend along the entire x-axis, that is, from $x \to -\infty$ to $x \to \infty$, whereas the closed geometry spans only a finite interval of the x-axis. Thus, in the open geometry approach the solution domain is of infinite extent. Obviously, this alters the BCs as the field in this approach is nowhere forced to vanish, and this consequently calls for a new procedure for normalizing the modes. Furthermore, when the width of the closed geometry tends to infinity, the separation between the propagation constants of allowed semi-radiating modes approaches zero. The discrete set of eigenmodes that was found in the closed geometry approach consequently transforms into a continuum of eigenmodes in the open geometry approach. As will be seen in the treatment of open waveguide layers, there may in fact exist both a finite number of discrete modes and a continuum of modes. In the new approach, the entire field will also be expanded on the eigenmodes, and due to the change in nature of the eigenmodes this procedure is slightly altered, compared to that in the closed geometry approach. Finally, the SER is implicitly determined through the power emitted from a dipole in the open geometry, and the results are compared with the results in the closed geometry approach.

In this chapter, the open geometry approach is presented in detail for single layers, specifically for a uniform layer and a waveguide layer. In the following chapter, the geometry is extended to comprise two layers. Since the open geometry approach introduces several new concepts, this division into two chapters has been chosen for clarity.

In the previous chapters, the time dependence has been assumed harmonic and on the form $\exp(-i\omega t)$. In following chapters, another harmonic time dependence, namely $\exp(i\omega t)$, is assumed, consistent with the convention in [Tigelis]. This change means that the first term in the expression for the x-eigenmodes in the generic solution in Eq. (2.14a) now represents a backward propagating wave while the second term represents a forward propagating wave. For the sake of recognizability, the a field coefficients will still be

related to the forward propagating part of the field while the b field coefficients will be related to the backward propagating part of the field. This is merely a matter of convention, and the generic x-dependent part of the field is then given by:

$$e_x(x) = a\exp(-i\kappa x) + b\exp(i\kappa x), \tag{4.1}$$

where κ is the propagation constant, and where the field coefficients are assumed to be chosen such that the mode is normalized. The subscript j has been omitted.

4.2 Eigenmodes

As for the closed geometry, two types of modes, guided modes and radiating modes, may exist. The guided modes may exist when the geometry comprises a region of higher refractive index, and the number of guided modes and the corresponding propagation constants depend on the width of the core region and refractive index contrast between core and cladding regions. The guided modes are, qualitatively, similar to those obtained in the closed geometry. However, a significant difference between the two approaches lies in the treatment of radiation modes that are oscillatory throughout the entire layer. Since no outer x boundaries are imposed in this approach, see Eqs. (3.2), no discretization, but rather a continuum of these modes exists.

Since the differences between the two kinds of modes are more pronounced than in the closed geometry, distinct names for mode types and corresponding propagation constants are introduced in the following sections. The notation to be introduced follows the conventions in [Tigelis] and is summarized in Table 1 at the end of this section.

Uniform Layer

A uniform layer of refractive index n is sketched in Fig. 4.1(a) where the dashed lines represent the z-boundaries, and where the arrows represent the forward and backward propagating parts of the field, respectively. The corresponding refractive index profile is shown in Fig. 4.1(b).

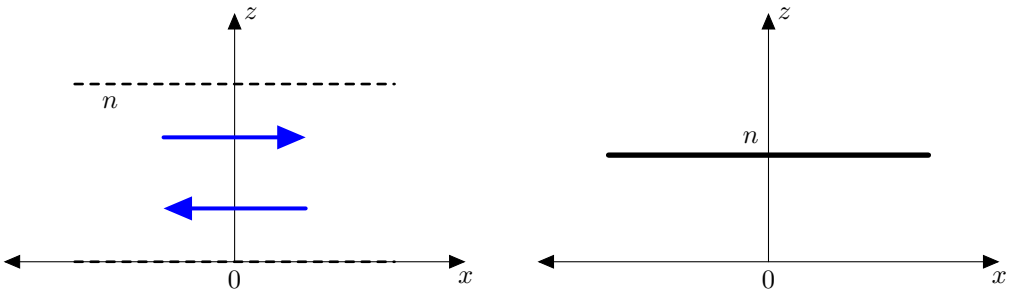

(a) xz-profile. The forward and backward propagating parts of the field are represented by blue arrows.

(b) Refractive index profile, $n(x)$.

Figure 4.1 Single-layer uniform along x and z.

As earlier discussed and as illustrated by the figures, the geometry has no outer x-boundaries, thus no outer BCs exist. Since the geometry is uniform along x, no inner BCs, see Eqs. (3.1), exist either, and hence no BCs exist for the uniform layer in the

open geometry. Therefore, two unknowns and no BCs exist. The resulting linearly independent solutions represent illumination from the left and from the right, respectively, and generally the mode is given as a linear combination of the following waves:

$$\boxed{\begin{aligned}\phi_1(x,s) &= a\exp(-isx), \\ \phi_2(x,s) &= b\exp(isx),\end{aligned}} \tag{4.2a}$$ (4.2b)

where s is the x-propagation constant, and a and b are arbitrary amplitudes. Concerning this propagation constant, the absence of BCs means that no constraints are put on the allowed propagation constants that therefore form a continuum in the range:

$$s \in]0, \infty[. \tag{4.3}$$

If s could be imaginary, the field would in- or decrease exponentially for propagation along the x-direction, and in the limit $|x| \to \infty$ the mode would diverge which must be rejected. Therefore, only (positive) real values are considered. This also means that the x-dependence of the field is purely oscillatory, that is, the modes in any uniform layer are solely radiation modes.

It should be emphasized that the waves in Eqs. (4.2) are assumed normalized, and that the field coefficients, a and b, are chosen to satisfy a normalization condition in Section 4.3. Upon normalization it is found that $a = b$.

By the definition in Eq. (2.13a), the sum of the square of the x- and z-propagation constants equals $n^2k_0^2$, and the z-propagation constant in the open and uniform layer, termed γ, is therefore given as function of s in the following way:

$$\gamma(s) = \sqrt{n^2k_0^2 - s^2}. \tag{4.4}$$

It is noted that $\mathrm{Re}(\gamma(s)) > 0$ while $\mathrm{Im}(\gamma(s)) < 0$. The latter is enforced to ensure that the electric field is exponentially decreasing along the respective z-propagation directions.

Waveguide Layer

A symmetric waveguide layer is illustrated in Fig. 4.2(a). The refractive index in the core region $-D/2 < x < D/2$ is denoted n_2, and everywhere else, the cladding region, the refractive index equals n_1, with $n_1 < n_2$. Fig. 4.2(b) displays $n(x)k_0$ as function of x for the same waveguide layer. In general, this geometry supports both guided and radiation modes. The guided modes have real propagation constants in region 2, and imaginary propagation constants in regions 1 and 3, while the radiation modes have real propagation constants in all regions.

Before discussing any further the modes that may exist in this layer, the two different propagation constants appertaining to the guided and radiation modes are introduced. For the guided modes, the x-propagation constants are termed $h_j^{[p]}$ where j refers to the jth guided mode and where p refers to region p, with $p = 1, 2, 3$, and $h_j^{[1]} = h_j^{[3]} \equiv h_j^{[1,3]}$. The corresponding z-propagation constants for the guided modes, independent of the zone-position, are termed β_j, and as for the closed geometry the x-propagation constants are implicitly functions of this through:

$$h_j^{[p]} = \sqrt{n_{[p]}^2k_0^2 - \beta_j^2}. \tag{4.5}$$

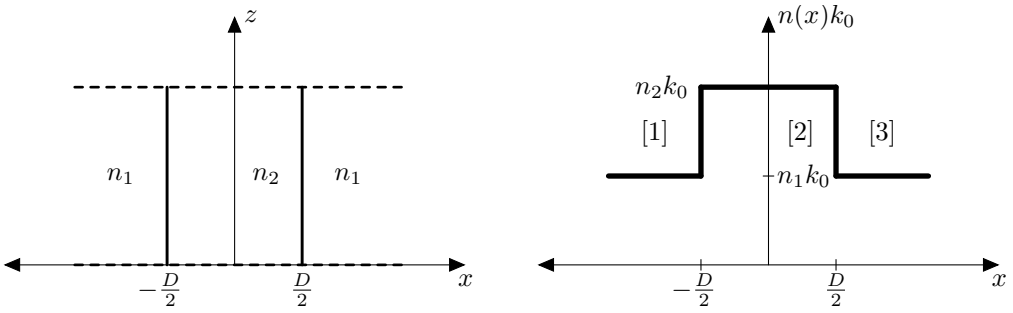

(a) xz-profile. The refractive indices are n_1 and n_2, respectively.

(b) $n(x)k_0$-profile.

Figure 4.2 Waveguide layer uniform along z.

For the radiation modes, the x-propagation constant in the core region is termed ρ_{co}, while in the cladding regions it is termed ρ. ρ_{co} is a function of ρ through:

$$\rho_{\text{co}} = \sqrt{k_0^2(n_2^2 - n_1^2) + \rho^2}. \tag{4.6}$$

The corresponding z-propagation constant which is a function of ρ is defined as:

$$\beta^2(\rho) = n_1^2 k_0^2 - \rho^2, \tag{4.7}$$

where, similar to $\gamma(s)$, the z-propagation constant has $\text{Re}(\beta(\rho)) > 0$ and $\text{Im}(\beta(\rho)) < 0$.

The x-propagation constants in regions 1 and 3 are imaginary ($h_j^{[1,3]}$) when $n_1^2 k_0^2 < \beta_j^2$ and real (ρ) when $n_1^2 k_0^2 > \beta^2(\rho)$. That is:

$$\text{Guided modes:} \qquad n_1^2 k_0^2 < \beta_j^2 < n_2^2 k_0^2,$$

$$\text{Radiation modes:} \qquad -\infty < \beta^2(\rho) < n_1^2 k_0^2.$$

Guided Modes

In principle, the guide mode propagation constants are determined using the same procedure as in the closed geometry. At the boundaries between zones of different refractive indices, it is demanded that the mode, $U_j(x)$, is continuous and differentiable which for the the waveguide geometry in Fig. 4.2 reads:

$$U_j^{[p]}(L_{p,p+1}) = U_j^{[p+1]}(L_{p,p+1}), \tag{4.8a}$$

$$\left.\frac{\mathrm{d}U_j^{[p]}}{\mathrm{d}x}\right|_{x=L_{p,p+1}} = \left.\frac{\mathrm{d}U_j^{[p+1]}}{\mathrm{d}x}\right|_{x=L_{p,p+1}}, \tag{4.8b}$$

where $p = 1, 2$, $L_{1,2} \equiv -D/2$ and $L_{2,3} \equiv D/2$. However, Eqs. (4.8) yield only four linearly independent equations in β_j and the six field field coefficients that are generally needed to express the guide modes in three different regions. Therefore, further equations or a reduction in the number of unknowns is needed, and the latter can be achieved from

the following arguments: In regions 1 and 3, the field must be exponentially decreasing for $|x| \to \infty$. From the fact that $h_j^{[1,3]} \in \mathbb{I}$ with $\mathrm{Im}(h_j^{[1,3]}) \in \mathbb{R}^+$, the second term in the generic solution in Eq. (4.1) diverges for $x \to -\infty$, and the first term diverges for $x \to \infty$. Since this would lead to unphysical modes, the corresponding field coefficients, namely $b_j^{[1]}$ and $a_j^{[3]}$, must equal zero. Defining the fields relative to the correct boundaries, the jth guided mode is then given by the following piecewise definition:

$$U_j(x) = \begin{cases} a_j^{[1]} \exp\left(-ih_j^{[1]}\left(x + \frac{D}{2}\right)\right), & -\infty < x \leq -\frac{D}{2}, \\ a_j^{[2]} \exp\left(-ih_j^{[2]}\left(x - \frac{D}{2}\right)\right) + b_j^{[2]} \exp\left(ih_j^{[2]}\left(x + \frac{D}{2}\right)\right), & -\frac{D}{2} \leq x \leq \frac{D}{2}, \\ b_j^{[3]} \exp\left(ih_j^{[3]}\left(x - \frac{D}{2}\right)\right), & \frac{D}{2} \leq x < \infty, \end{cases} \tag{4.9}$$

where the field coefficients are chosen such that the mode is normalized. The details of this normalization are given in Section 4.3.

Combining Eqs. (4.8) and (4.9) yields a matrix equation $\mathbf{A}_j \boldsymbol{c}_j = \mathbf{0}$ where $\mathbf{A}_j$ is a 4×4-matrix, given in Appendix D.1, and where $\boldsymbol{c}_j = [a_j^{[1]}\ a_j^{[2]}\ b_j^{[2]}\ b_j^{[3]}]^T$. Using the same procedure as in Section 3.2, the matrix equation is solved for the values of β_j for which $\mathrm{Det}(\mathbf{A}_j) = 0$. Through this, the discrete values of β_j and the appertaining four field coefficients are determined, which concludes the determination of the guided modes.

The number of guided modes is critically dependent on the refractive index contrast, $\Delta n \equiv n_2 - n_1$, and the width of the core region, D. Increasing either Δn or D potentially allows a waveguide to support additional guided modes.

Radiation Modes

For values of the z-propagation constant, $\beta(\rho)$, that are smaller than $n_1 k_0$, a continuum of allowed x-propagation constants, ρ and ρ_{co}, exist. For the radiation modes, the mode is in all zones oscillatory, and they may then, as for the uniform layer, without any numerical problems, be defined relative to $x = 0$. Since no parts of the mode are exponentially in- or decreasing, none of the field coefficients can immediately be set equal to zero, and as the point of departure the radiation mode is defined as follows:

$$e_{\mathrm{rad}}(x, \rho) = \begin{cases} a^{[1]} \exp(-i\rho x) + b^{[1]} \exp(i\rho x), & -\infty < x \leq -\frac{D}{2}, \\ a^{[2]} \exp(-i\rho_{\mathrm{co}} x) + b^{[2]} \exp(i\rho_{\mathrm{co}} x), & -\frac{D}{2} \leq x \leq \frac{D}{2}, \\ a^{[3]} \exp(-i\rho x) + b^{[3]} \exp(i\rho x), & \frac{D}{2} \leq x < \infty, \end{cases} \tag{4.10}$$

where again it is assumed that the field coefficients are chosen to normalize the radiation mode. The field coefficients are functions of the x-propagation constant, ρ, but to maintain a simple notation this dependence is not given explicitly in the above definition, and is generally suppressed.

Applying again the demands of continuity and differentiability at $x = -D/2$ and $x = D/2$ gives the matrix equation:

$$\mathbf{A}(\rho)\boldsymbol{c}(\rho) = \mathbf{0}, \tag{4.11}$$

Layer	Guided Modes			Radiation Modes		
	x-Mode	x-PC	z-PC	x-Mode	x-PC	z-PC
Uniform		(none)		$\phi_l(x,s)$	s	$\gamma(s)$
Waveguide	$U_j(x)$	$h_j^{[1,3]}, h_j^{[2]}$	β_j	$\psi_m(x,\rho)$	ρ, ρ_{co}	$\beta(\rho)$

Table 1 Summary of the guided modes and radiation modes that have been defined and discussed in Section 4.2. For the uniform and waveguide layers, both in an open geometry, the x-dependent eigenmodes and the corresponding x- and z-propagation constants (PC) are given.

where $\mathbf{A}(\rho)$ is a 4×6-matrix, defined in Appendix D.1, and $\boldsymbol{c}(\rho) = [a^{[1]}\, b^{[1]}\, a^{[2]}\, b^{[2]}\, a^{[3]}\, b^{[3]}]^T$.

The matrix equation in Eq. (4.11) can be solved for any $\rho > 0$, and therefore the propagation constant is, contrary to the closed geometry approach and the approach for determining the guided modes in the open geometry, not an unknown, but rather a parameter. However, the matrix equation contains six unknowns, the field coefficients in the three regions, and only four equations. Hence, the solutions are given as the span of two eigenvectors, that is, in terms of two free parameters. These free parameters can be chosen at will, but since illumination from the left and right are described by $a^{[1]}$ and $b^{[3]}$, respectively, these are conveniently chosen as the free parameters.

By setting $a^{[1]} \neq 0$, $b^{[3]} = 0$, this represents a field that is illuminated from the left. The matrix equation in Eq. (4.11) then contains five unknowns and four equations, and the solution to this is the span of one eigenvector. Carrying out the same procedure for $a^{[1]} = 0$, $b^{[3]} \neq 0$, which represents illumination from the right, another eigenvector is obtained, and the superposition of these two eigenvectors that are functions of $a^{[1]}$ and $b^{[3]}$ then determines the radiation mode for an arbitrary ρ. To follow the convention in [Tigelis], the contribution to the eigenmode with $b^{[3]} = 0$ is termed $\psi_1(x)$, and the contribution with $a^{[1]} = 0$ is termed $\psi_2(x)$:

$$\boxed{\psi_m(x,\rho) = \begin{cases} e_{\text{rad}}(x,\rho)|_{b^{[3]}=0}, & m=1, \\ e_{\text{rad}}(x,\rho)|_{a^{[1]}=0}, & m=2, \end{cases}} \tag{4.12}$$

where $e_{\text{rad}}(x,\rho)$ is defined in Eq. (4.10).

Overview

The various eigenmodes and propagation constants that have been introduced in this section are summarized in Table 1.

4.3 Normalization

This section will discuss the normalization of the eigenmodes, $\phi_l(x,s)$, $U_j(x)$ and $\psi_m(x,\rho)$, that were introduced in the preceding section. As opposed to the normalization for the closed geometry (Section 3.3), the Power inner product will not be applied, but rather the simpler $L^2(\mathbb{R})$:

$$\langle f, g\rangle_{L^2} = \int_{-\infty}^{\infty} f(x)g(x)^*\,\mathrm{d}x. \tag{4.13}$$

From the result in Eq. (3.6), conversion to the Power inner product is obtained by multiplying the above integral with a factor of $\beta^*/2$ where β represents either of the z-propagation constants, $\gamma(s)$, β_j or $\beta(\rho)$, depending on the mode type under investigation. That is:

$$\langle f, g\rangle_{\text{P}} = \frac{\beta^*}{2}\langle f, g\rangle_{L^2}. \tag{4.14}$$

In Section 4.6, the Power inner product will be applied in the normalization process in order to calculate the SER. However, in Chapter 5 the $L^2(\mathbb{R})$ product will be applied to be consistent with the choice of inner product in [Tigelis].

Uniform Layer

A key difference between the closed and open geometry approaches is the orthogonality and normalization properties of the radiation modes. Since the radiation modes in the open geometry are continuously oscillating and never vanish, the normalization integrals are unbounded. However, by use of the Dirac delta function, a new criterion for a normalized mode is established via [Tigelis, Snyder, Chapter 25-4]:

$$\int_{-\infty}^{\infty} \check{\phi}_k(x,s)\check{\phi}_l(x,s')^* \,\mathrm{d}x = \mathcal{N}\delta_{kl}\delta(s-s'), \tag{4.15}$$

for $k, l = 1, 2$ and $s, s' \in]0, \infty[$. $\check{\phi}$ denotes a non-normalized radiation mode in a uniform layer. $\mathcal{N}$ denotes the normalization constant and defines the normalized radiation modes via $\phi_l(x,s) = \check{\phi}_l(x,s)/\sqrt{\mathcal{N}}$. Finally, $\delta(s-s')$ is the Dirac delta function that, to be mathematically consistent, is not a function, but a distribution. The Dirac delta function is only meaningful if evaluated under an integral and is defined by the following property:

$$\int_a^b \delta(x-x_0)f(x)\,\mathrm{d}x = \begin{cases} f(x_0), & x_0 \in]a,b[, \\ 0, & x_0 \notin [a,b], \end{cases} \tag{4.16}$$

for some $a, b, x_0 \in \mathbb{R}$, where $a < b$. A useful representation of $\delta(x-x_0)$ is [Bransden, Appendix A.2]:

$$\int_a^b \delta(x-x_0)f(x)\,\mathrm{d}x = \lim_{\epsilon\to\infty}\int_a^b \left[\frac{1}{2\pi}\int_{-\epsilon}^{\epsilon} \exp\left(ik(x-x_0)\right)\,\mathrm{d}k\right] f(x)\,\mathrm{d}x. \tag{4.17}$$

Rather than using this somewhat cumbersome definition, a weaker definition of the Dirac delta function is introduced as:

$$\delta(x-x_0) = \frac{1}{2\pi}\int_{-\infty}^{\infty} \exp\left(ik(x-x_0)\right)\,\mathrm{d}k, \tag{4.18}$$

The integral in Eq. (4.18) does not converge, and hence it should implicitly be understood that this weak definition only applies in the sense of a short hand form of Eq. (4.17).

The normalization constant is derived in Appendix D.2 where a validation of the orthogonality relation in Eq. (4.15) is also given. The resulting normalized radiation modes in a uniform layer are given as:

$$\phi_l(x,s) = \frac{1}{\sqrt{2\pi}}\begin{cases} \exp\left(-isx\right), & l = 1, \\ \exp\left(isx\right), & l = 2. \end{cases} \tag{4.19}$$

Waveguide Layer

Guided Modes

The normalization of the guided modes is simpler than that of the radiation modes because these modes decrease exponentially for $|x| \to \infty$. It is consequently possible to scale the field coefficients such that:

$$\int_{-\infty}^{\infty} |U_j(x)|^2 \, \mathrm{d}x = 1. \tag{4.20}$$

The normalization constant, $\mathcal{N}_j \equiv \int_{-\infty}^{\infty} |\breve{U}_j(x)|^2 \, \mathrm{d}x$, for a non-normalized guided mode, $\breve{U}_j(x)$, is given in Appendix D.3, and the normalized modes are once again given through the relation $U_j(x) = \breve{U}_j(x)/\sqrt{\mathcal{N}_j}$.

Radiation Modes

The normalization of the waveguide radiation modes, $\breve{\psi}_m(x,\rho)$, can in principle be carried out by direct computation of the normalization integral. However, an alternative and more graceful procedure exists, and this is presented in the following. Initially, it is noticed that the waveguide radiation modes, $\breve{\psi}_m(x,\rho)$, must reduce to the uniform layer radiation modes, $\breve{\phi}_m(x,\rho)$, when the refractive index difference, Δn, tends to zero. The radiation modes $\breve{\psi}_m(x,\rho)$ may then conveniently be written as the sum of a uniform layer radiation mode, $\breve{\phi}_m(x,\rho)$, and a scattering contribution, $\breve{\xi}_m(x,\rho)$, which is due to the waveguide profile:

$$\breve{\psi}_m(x,\rho) = \breve{\phi}_m(x,\rho) + \breve{\xi}_m(x,\rho). \tag{4.21}$$

The uniform layer term, $\breve{\phi}_m(x,\rho)$, represents the illumination of the waveguide from either the left, $m = 1$, or from the right, $m = 2$. To clarify: If the coefficient in $\breve{\psi}_1(x,\rho)$ that represents illumination from the left is denoted $\breve{a}^{[1]}$, then the uniform layer term, $\breve{\phi}_1(x,\rho)$, is described by the same field coefficient, such that $\breve{\phi}_1(x,\rho) = \breve{a}^{[1]} \exp(-i\rho x)$. Similarly, $\breve{\psi}_2(x,\rho)$ is illuminated from the right by the coefficient $\breve{b}^{[3]}$, and the corresponding corresponding uniform layer term is forced to take the form $\breve{\phi}_2(x,\rho) = \breve{b}^{[3]} \exp(i\rho x)$. [Sammut] proves that the Power inner product of $\breve{\psi}_m(x,\rho)$ reduces to the Power inner product of $\breve{\phi}_m(x,\rho)$, that is, that the contributions from the scattering term vanishes. Consequently, the $L^2(\mathbb{R})$ inner product of $\breve{\psi}_m(x,\rho)$ must also reduce to the $L^2(\mathbb{R})$ inner product of $\breve{\phi}_m(x,\rho)$, because the two inner products only differ by the constant factor $\beta(\rho)^*/2$. Using this, the normalization integral of a waveguide radiation mode can be rewritten as:

$$\int_{-\infty}^{\infty} \breve{\psi}_k(x,\rho)\breve{\psi}_m(x,\rho')^* \, \mathrm{d}x = \int_{-\infty}^{\infty} \breve{\phi}_k(x,\rho)\breve{\phi}_m(x,\rho')^* \, \mathrm{d}x = \mathcal{N}\delta_{km}\delta(\rho-\rho'). \tag{4.22}$$

Assuming that the illumination terms in $\breve{\psi}_k(x,\rho)$ and $\breve{\psi}_m(x,\rho')$, that is $\breve{\phi}_k(x,\rho)$ and $\breve{\phi}_m(x,\rho')$, respectively, are given such that their field coefficients equal unity, the resulting normalization constant equals $\mathcal{N} = 2\pi$, cf. Appendix D.2. The resulting normalized waveguide radiation modes can then be rewritten by use of Eq. (4.12):

$$\psi_m(x,\rho) = \frac{1}{\sqrt{2\pi}} \begin{cases} e_{\mathrm{rad}}(x,\rho)|_{a^{[1]}=1,\, b^{[3]}=0}, & m = 1, \\ e_{\mathrm{rad}}(x,\rho)|_{b^{[3]}=1,\, a^{[1]}=0}, & m = 2, \end{cases} \tag{4.23}$$

4.4 Orthogonality and Completeness

This section presents a number of orthogonality and completeness relations that relate the different kinds of modes introduced in Section 4.2. Throughout, it is assumed that all modes are normalized with respect to the $L^2(\mathbb{R})$ inner product, as described in the preceding section. Some of the relations have been presented in the previous section, and some are given in [Tigelis]. In [Tigelis], the modes are expressed in terms of real functions, and consequently the real $L^2(\mathbb{R})$ inner product, $\langle f, g\rangle_{L^2} = \int_{-\infty}^{\infty} f(x)g(x)\,\mathrm{d}x$, is used. In the following, these relations are assumed to hold for the modes presented in Section 4.2 when the complex $L^2(\mathbb{R})$ inner product, introduced in Eq. (4.13) ,is applied. The relations are stated below:

$$\int_{-\infty}^{\infty} U_j(x)U_k(x)^*\,\mathrm{d}x = \delta_{jk}, \qquad j,k = 1,2,\ldots,N, \tag{4.24a}$$

$$\int_{-\infty}^{\infty} \psi_m(x,\rho)\psi_k(x,\rho')^*\,\mathrm{d}x = \delta_{mk}\,\delta(\rho-\rho'), \qquad m,k = 1,2, \tag{4.24b}$$

$$\int_{-\infty}^{\infty} \phi_l(x,s)\phi_k(x,s')^*\,\mathrm{d}x = \delta_{lk}\,\delta(s-s'), \qquad l,k = 1,2, \tag{4.24c}$$

$$\int_{-\infty}^{\infty} U_j(x)\psi_m(x,\rho)^*\,\mathrm{d}x = 0, \qquad j = 1,2,\ldots,N,\ m = 1,2, \tag{4.24d}$$

$$\sum_{j=1}^{N} U_j(x)U_j(x')^* + \sum_{m=1}^{2}\int_0^{\infty} \psi_m(x,\rho)\psi_m(x',\rho)^*\,\mathrm{d}\rho = \delta(x-x'), \tag{4.24e}$$

$$\sum_{l=1}^{2}\int_0^{\infty} \phi_l(x,s)\phi_l(x',s)^*\,\mathrm{d}s = \delta(x-x'), \tag{4.24f}$$

where N denotes the number of guided modes within the waveguide. The conjugated versions of the above relations also hold since $\delta(x-x')^* = \delta(x-x')$.

The relations in Eqs. (4.24) play an important role when two layers in the open geometry are considered and analyzed in Chapter 5, in particular in the derivations of transmission and reflection coefficients and of an integral equation for the field at the interface between the two layers.

4.5 Eigenmode Expansion

This section serves to express the electric field in a layer in terms of the eigenmodes, discussed and analyzed in the previous sections. Especially, the treatment of the radiation modes differ compared to the closed geometry because a continuum of radiation modes exist. First, the electric field in a uniform layer is discussed, and secondly the field in a waveguide layer.

Uniform Layer

The field in a uniform layer consists solely of contributions from radiation modes. Because a radiation mode does not tend to zero as $|x| \to \infty$, it cannot be given physical substance in itself: For instance, to excite any specific radiation mode, $\phi(x,s)$, an infinite amount of energy would be required. However, if an infinite number of radiation modes are excited, the resulting superposition of these radiation modes may constitute a wave of

finite energy [Sammut]. Consequently, the field, $E(x,z)$, in a uniform layer is constructed as the superposition of all allowed uniform layer radiation modes [Snyder, Chapter 25-3]. For some layer with uniformity along both x and z, illuminated from either the top or the bottom, the field may be written as:

$$E(x,z) = \sum_{l=1}^{2} \int_0^\infty A_l(s)\phi_l(x,s) \exp(\pm i\gamma(s)z)\, \mathrm{d}s, \tag{4.25}$$

where $A_l(s)$ denote the modal amplitudes. The exponential term in z accounts for the z-dependence in the layer, as defined by Eq. (2.14b). Specifically, $\exp(-i\gamma(s)z)$ represents a forward propagating field, while $\exp(i\gamma(s)z)$ represents a backward propagating field.

In a general layer in which there may exist both forward and backward propagating components along z, one must include additional terms, such that:

$$\boxed{E(x,z) = \sum_{l=1}^{2} \int_0^\infty \phi_l(x,s)\Big[A_l(s)\exp(-i\gamma(s)z) + B_l(s)\exp(i\gamma(s)z)\Big]\, \mathrm{d}s,} \tag{4.26}$$

where the coefficients $A_l(s)$ and $B_l(s)$ are modal amplitudes.

Waveguide Layer

The field in a waveguide layer, contrary to the field in a uniform layer, consists of contributions from both guided modes and radiation modes. Including again all radiation modes, and now also the discrete set of guided modes, the field in a general waveguide layer consisting of both forward and backward propagating parts becomes:

$$\boxed{\begin{aligned} E(x,z) = &\sum_{j=1}^{N} U_j(x)\Big[A_j\exp(-i\beta_j z) + B_j\exp(i\beta_j z)\Big] \\ &+ \sum_{m=1}^{2} \int_0^\infty \psi_m(x,\rho)\Big[C_m(\rho)\exp(-i\beta(\rho)z) + D_m(\rho)\exp(i\beta(\rho)z)\Big]\, \mathrm{d}\rho, \end{aligned}} \tag{4.27}$$

where N denotes the number of guided modes. The Coefficients A_j, B_j, $C_m(\rho)$ and $D_m(\rho)$ are modal amplitudes.

4.6 Spontaneous Emission Rate

This section will investigate the normalized SER, α, in an open uniform layer and in an open waveguide layer. As for the closed geometry (Section 3.8), the normalized SER can equally well be calculated as the power ratio, P/P_0, where P is the power emitted from the current source in a given optical environment and P_0 is the power emitted from the same current source, but in a uniform layer. From this convention, the power ratio, and hence the normalized SER, in a uniform layer equals unity. The following section consequently serves to derive a value for the reference power, P_0. The ensuing section derives the power emitted from the current source inside a waveguide layer. For the waveguide layer, the continuous description of the contributing radiation modes must, due to the numerical implementation, be abandoned in favor of a discrete sampling of the continuum of radiation modes. Hence, as in the closed geometry, the calculation of the SER is again discretized, and dependent on the number of included modes.

Modeling

The current source, $\mathbf{J}(\boldsymbol{r})$, is assumed to be of the same dipole type as in the closed geometry, namely:

$$\mathbf{J}(\boldsymbol{r}) = \delta(z)\delta(x - x_c)\,\hat{\boldsymbol{y}}, \tag{4.28}$$

which leads to the same general expression for the power as for the closed geometry (see Eq. (3.34)):

$$P = -\frac{1}{2}\mathrm{Re}(E(x_c, 0)). \tag{4.29}$$

Thus, to determine the power, P, the electric field that the dipole excites must be expressed. To follow the convention in [Snyder], all modes are in this section assumed normalized with respect to the Power inner product.

Uniform Layer

In a uniform and open layer, the electric field can generally be expressed as in Eq. (4.26). In this context, it should be noted that the dipole current is placed in $z = 0$, and since the geometry has uniformity along z, the field for $z > 0$ and for $z < 0$ consists solely of z-dependent parts that propagate along the positive and negative z-directions, respectively:

$$E(x, z) = \sum_{l=1}^{2} \begin{cases} \int_0^\infty \mathcal{A}_l(s)\phi_l(x, s)\exp(-i\gamma(s)z)\,\mathrm{d}s, & z \geq 0, \\ \int_0^\infty \mathcal{A}_l(s)\phi_l(x, s)\exp(i\gamma(s)z)\,\mathrm{d}s, & z < 0. \end{cases} \tag{4.30}$$

Due to symmetry, the modal amplitudes, $\mathcal{A}_l(s)$, for propagation along the positive and negative z-directions, respectively, must be equal. The modal amplitudes are given as [Snyder, Eq. (31-37a)]:

$$\mathcal{A}_l(s) = -\frac{1}{4\mathcal{N}'(s)} \int_{\mathcal{V}} \boldsymbol{\phi}_l(x, s)^* \cdot \mathbf{J}(\boldsymbol{r})\exp(-i\gamma(s)z)\,\mathrm{d}\Omega, \tag{4.31}$$

where $\mathcal{N}'(s)$ is given by use of the Power inner product normalization (Eq. (3.8)): $\mathcal{N}'(s) = \gamma(s)^*/|\gamma(s)|\mathcal{N}(s)$, with $\mathcal{N}(s) = 1$. The vectorial mode, $\boldsymbol{\phi}(x, s)$, is given as $\boldsymbol{\phi}_l(x, s) = \phi_l(x, s)\,\hat{\boldsymbol{y}}$, and the integral is taken over a volume, $\mathcal{V}$, that bounds the current source. Using this and the form of the current source given in Eq. (4.28) gives the following expression for the modal amplitudes:

$$\mathcal{A}_l(s) = -\frac{|\gamma(s)|}{4\gamma(s)^*}\phi_l(x_c, s)^*. \tag{4.32}$$

Combining Eqs. (4.29), (4.30) and (4.32) gives an explicit expression for the power:

$$P = \sum_{l=1}^{2} \frac{1}{8} \int_0^\infty |\phi_l(x_c, s)|^2\,\mathrm{Re}\left(\frac{|\gamma(s)|}{\gamma(s)^*}\right)\,\mathrm{d}s. \tag{4.33}$$

By its definition in Eq. (4.4), $\gamma(s)$ is only real when $s \leq nk_0$ which truncates the integral at $s = nk_0$. As earlier stated, the modes are normalized with respect to the Power inner

product which, when applying the relation between the Power inner product and the $L^2(\mathbb{R})$ inner product in Eq. (4.14), gives:

$$\begin{aligned}|\phi_l(x_c,s)|^2 = \left|\sqrt{\frac{1}{\mathcal{N}_\text{P}}}\exp(\mp isx_c)\right|^2 &\equiv \left|\sqrt{\frac{2}{\gamma(s)^*}\frac{1}{\mathcal{N}_{L^2}}}\exp(\mp isx_c)\right|^2 \\ &= \left|\frac{2}{\mathcal{N}_{L^2}\gamma(s)^*}\right||\exp(\mp isx_c)|^2 \\ &= \left|\frac{2}{2\pi\gamma(s)^*}\right| \\ &= \frac{1}{\pi\gamma(s)}, \end{aligned} \tag{4.34}$$

where $\mathcal{N}_\text{P}$ is the normalization constant related to modes normalized with respect to the Power inner product, and $\mathcal{N}_{L^2}$ is the normalization constant that was derived with the $L^2(\mathbb{R})$ inner product in Appendix D.2. In the last step, it has been used that $\gamma(s)$ is real and positive in the range $0 \leq s \leq nk_0$, such that $\gamma(s)^* = \gamma(s)$. Insertion in Eq. (4.33) then finally gives the reference power, P_0:

$$P_0 \equiv P = \sum_{l=1}^{2}\frac{1}{8\pi}\int_0^{nk_0}\frac{1}{\sqrt{n^2k_0^2-s^2}}\,\mathrm{d}s \tag{4.35a}$$

$$= \frac{1}{4\pi}\left[\arcsin\left(\frac{s}{nk_0}\right)\right]_0^{nk_0}$$

$$\Updownarrow$$

$$\boxed{P_0 = \frac{1}{8}.} \tag{4.35b}$$

The value of P_0 is given in arbitrary units and serves both in the closed and open geometry calculations as the reference power that all powers are normalized with respect to.

Waveguide Layer

By the general result in Eq. (4.29), the power emitted from the dipole current in the waveguide layer is given by the value of the field at the origin of the dipole current. The field is generally given by an expansion on the allowed eigenmodes in the waveguide layer, as described in Eq. (4.27). As for the uniform layer, the field for $z > 0$ and $z < 0$ contains only z-dependent parts that propagate along the positive and negative z-directions, respectively:

$$E(x,z) = \begin{cases}\displaystyle\sum_{j=1}^{N}\mathcal{A}_jU_j(x)\exp(-i\beta_jz) + \sum_{m=1}^{2}\int_0^\infty \mathcal{B}_m(\rho)\psi_m(x,\rho)\exp(-i\beta(\rho)z)\,\mathrm{d}\rho, & z \geq 0, \\ \displaystyle\sum_{j=1}^{N}\mathcal{A}_jU_j(x)\exp(i\beta_jz) + \sum_{m=1}^{2}\int_0^\infty \mathcal{B}_m(\rho)\psi_m(x,\rho)\exp(i\beta(\rho)z)\,\mathrm{d}\rho, & z < 0, \end{cases} \tag{4.36}$$

where the modal amplitudes, $\mathcal{A}_j$ and $\mathcal{B}_m(\rho)$, as for the uniform layer, due to symmetry must be equal for propagation along either of the two z-directions. The power may

conveniently be defined as the sum of a guided mode contribution, P_{g}, and a radiation mode contribution, P_{r}:

$$P = P_{\mathrm{g}} + P_{\mathrm{r}}. \tag{4.37}$$

In the following paragraphs, expressions for P_{g} and P_{r} are derived.

The contribution from the guided modes can be derived in the same way as the power emitted from a dipole in a closed geometry waveguide layer, and the result, in terms of the guided modes in the open geometry, $U_j(x)$, is therefore given by Eq. (3.40):

$$P_{\mathrm{g}} = \frac{1}{8}\sum_{j=1}^{N} |U_j(x_c)|^2, \tag{4.38}$$

where N is the number of guided modes. From the scheme on p. 44, all β_j are real, and therefore all guided modes contribute to the power.

Concerning the contribution from the radiation modes, the expression in Eq. (4.33), derived for the radiation modes in the vacuum layer, is valid for the radiation modes in the waveguide layer, with the change from ϕ_l to ψ_m, s to ρ, and $\gamma(s)$ to $\beta(\rho)$:

$$P_{\mathrm{r}} = \frac{1}{8}\sum_{m=1}^{2}\int_0^{\infty} |\psi_m(x_c,\rho)|^2 \,\mathrm{Re}\left(\frac{|\beta(\rho)|}{\beta(\rho)^*}\right)\,\mathrm{d}\rho = \frac{1}{8}\sum_{m=1}^{2}\int_0^{n_1k_0} |\psi_m(x_c,\rho)|^2\,\mathrm{d}\rho, \tag{4.39}$$

where the last equal sign follows from the definition of $\beta(\rho)$ in Eq. (4.7). The total power emitted is then found by combining Eqs. (4.37), (4.38) and (4.39):

$$\boxed{P = \frac{1}{8}\left(\sum_{j=1}^{N}|U_j(x_c)|^2 + \sum_{m=1}^{2}\int_0^{n_1k_0}|\psi_m(x_c,\rho)|^2\,\mathrm{d}\rho\right).} \tag{4.40}$$

In principle, the above expression can be applied to evaluate the power for a dipole placed at an arbitrary x in the waveguide layer. However, the numerical implementation of the P_{r} integral-term makes it beneficial to express this term more explicitly. To this end, it is assumed that the dipole is situated in the core region of the waveguide (the region with refractive index n_2 in Fig. 4.2(b)), and using the definition of $\psi_m(x,\rho)$ from Eq. (4.10) insertion in Eq. (4.39) gives:

$$\begin{aligned}
P_{\mathrm{r}} &= \frac{1}{8}\sum_{m=1}^{2}\int_0^{n_1k_0}\left|a_m^{[2]}\exp(-i\rho_{\mathrm{co}}x_c) + b_m^{[2]}\exp(i\rho_{\mathrm{co}}x_c)\right|^2\,\mathrm{d}\rho \\
&= \frac{1}{8}\sum_{m=1}^{2}\int_0^{n_1k_0}\left|a_m^{[2]}\right|^2 + \left|b_m^{[2]}\right|^2 + a_m^{[2]}b_m^{[2]*}\exp(-2i\rho_{\mathrm{co}}x_c) + a_m^{[2]*}b_m^{[2]}\exp(2i\rho_{\mathrm{co}}x_c)\,\mathrm{d}\rho \\
&= \frac{1}{8}\sum_{m=1}^{2}\int_0^{n_1k_0}\left|a_m^{[2]}\right|^2 + \left|b_m^{[2]}\right|^2 + 2\mathrm{Re}\left(a_m^{[2]}b_m^{[2]*}\exp(-2\rho_{\mathrm{co}}x_c)\right)\,\mathrm{d}\rho.
\end{aligned} \tag{4.41}$$

It is worth stressing that the field coefficients, $a_m^{[2]}$ and $b_m^{[2]}$, and the x-propagation constant in the waveguide, ρ_{co}, are all functions of the x-propagation constant in the cladding regions, ρ. Since no analytical expressions for the dependence of the field coefficients on ρ are available, the expression in Eq. (4.41) cannot be reduced any further. The total

power emitted from the dipole, placed in the core region, is then given by insertion of the new expression for P_r into Eq. (4.40):

$$P = \frac{1}{8}\left(\sum_{j=1}^{N} |U_j(x_c)|^2 + \sum_{m=1}^{2} \int_0^{n_1 k_0} \left|a_m^{[2]}\right|^2 + \left|b_m^{[2]}\right|^2 + 2\mathrm{Re}\left(a_m^{[2]} b_m^{[2]*} \exp(-2\rho_\mathrm{co} x_c)\right) \, \mathrm{d}\rho \right). \tag{4.42}$$

Comparing the expressions for the waveguide layer power in the closed and open geometries, Eqs. (3.40) and (4.42), respectively, the contributions from the guided modes are qualitatively the same in the two approaches, namely sums over these discrete modes. The contributions from the semi-radiating and radiating modes, in turn, differ as these are sums over discrete modes and integrals over continuous modes in the closed and open geometries, respectively. Therefore, the essential difference in the determination of the power in the two approaches is the treatment of the semi-radiating/radiating modes. The treatment of these in the open geometry approach is the subject of the following sections where the integral is approximated numerically in different ways.

Computational Results

The power emitted from a dipole in a waveguide layer was expressed in the previous section, and as therein mentioned, the integral component of the expression must be evaluated numerically. Therefore, determination of the power is essentially a matter of approximating the integral in Eq. (4.42), and in the following sections it is approximated in two different ways. The approximation of the integral is carried out by introducing a discretization of the continuous propagation constants, and this discretization can, in principle, be chosen at will. Compared to the closed geometry where the power is given as a sum over the discrete eigenmodes and where the discretization is dictated by the geometry (dimensions of solution domain and refractive indices), this free choice of discretization in the open geometry represents a parameter that, if chosen correctly, can be exploited to obtain rapid convergence.

First, a Riemann sum is used to approximate the integral, and the resulting approximate power is presented as a function of the repetition length, L_rep, that will be introduced in the following section. Afterwards, an alternative approach using a non-equidistant discrete sampling of the integrand is presented, leading to significantly faster convergence. Since the power in the uniform layer has an analytical value, these procedures are also applied to the integral in Eq. (4.35a) as this allows assessments of the convergence of the applied procedures.

Riemann Sum

Even though the integral in determining the power emitted from the dipole in a uniform layer, P_0, is analytically solvable, it is instructive to apply the Riemann sum procedure to this as well as to the power in the waveguide layer. The integrand for the uniform layer power is $1/\gamma(s)$ (Eq. (4.35a)), and for the waveguide layer power it is (Eq. (4.42)):

$$\Gamma_m(\rho) \equiv \left|a_m^{[2]}\right|^2 + \left|b_m^{[2]}\right|^2 + 2\cos(2\rho_\mathrm{co} x_c)\mathrm{Re}\left(a_m^{[2]} b_m^{[2]*}\right), \tag{4.43}$$

and these are plotted as functions of s and ρ, respectively, in Figs. 4.3(a) and 4.3(b). The two plots have been obtained with $n = n_1 = 1$, $n_2 = 2$, and $\lambda = 1.55\,\mu$m. With these

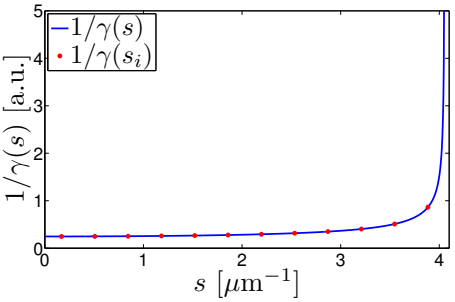

(a) Uniform layer. The integrand is $1/\gamma(s)$.

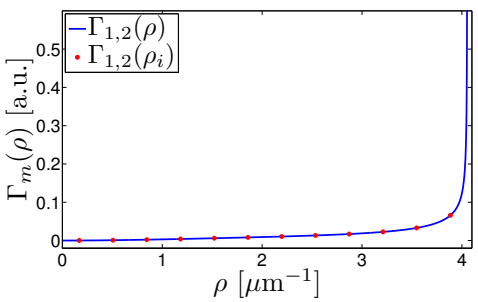

(b) Waveguide layer. The integrand is $\Gamma_m(\rho)$ with $\Gamma_1(\rho) = \Gamma_2(\rho)$, defined in Eq. (4.43).

Figure 4.3 Integrands in expressions for P, see Eqs. (4.35a) and (4.43), in open geometry. The plots display the integrands as well as the discrete, equidistant sampling points used in the Riemann sum.

values $nk_0 = n_1 k_0 = 2\pi/1.55\,\mu\text{m} = 4.05\,\mu\text{m}^{-1}$. The width of the core in the waveguide layer is chosen as $D_g = 2.0\,\mu$m. Due to symmetry, $\Gamma_1(\rho) = \Gamma_2(\rho)$.

The integrals that define the contributions to the power emitted from the dipole in the uniform and waveguide layers, respectively, may, as a first approach, be approximated by a Riemann sum. That is, the integration interval is divided into a number of subintervals, #, each of the same width, and these intervals then define a series of rectangles that are used to approximate the integral. Besides the different values, the two integrands exhibit the same behavior: They are both almost constant for $s, \rho \in [0, 3.5\,\mu\text{m}^{-1}]$, and as s and ρ approach nk_0 and $n_1 k_0$, respectively, the integrands diverge. In the plots, $\# = 12$ subintervals have been defined by their middle points, and these points are used to approximate the integrals using the Riemann sum procedure.

In order to compare the results with those for the closed geometry, for which the power ratio was determined as a function of the x-width of the geometry, L_x, it is desirable to present the power ratio in the open geometry as a function of a characteristic length. This length, called the repetition length, L_{rep}, is introduced in the following.

The repetition length is the length along x over which the field repeats itself. In Appendix D.4, a relation between the repetition length and the number of subintervals is derived, and this is:

$$L_{\text{rep}} = \frac{2\pi\#}{nk_0}. \tag{4.44}$$

Hence, the repetition length is proportional to the number of subintervals. Derivation of the repetition length for the waveguide layer is less apparent than for a uniform layer, but qualitatively L_{rep} can be assumed to remain proportional to #, and plotting the power ratio for the waveguide as a function of L_{rep} is consequently still instructive. The numbers of subintervals in the Riemann sums will be chosen such that L_{rep} has values in the same range as L_x in Eq. (3.47):

$$\# \in [4, 5, \ldots, 19] \Leftrightarrow L_{\text{rep}} \in [6.20\,\mu\text{m}, 7.75\,\mu\text{m}, \ldots, 29.45\,\mu\text{m}]. \tag{4.45}$$

Using this range of subintervals, the power ratios for the uniform layer and for the waveguide layer have been determined using the Riemann sum approach as functions of # and L_{rep}. The results can be seen in Figs. 4.4(a) and 4.4(b), respectively.

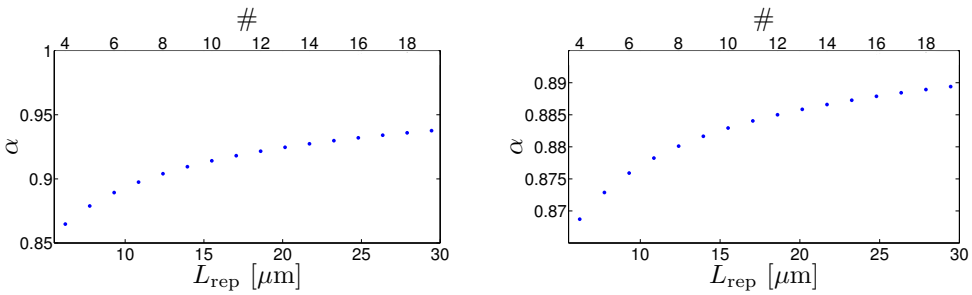

(a) Uniform layer.

(b) Waveguide layer.

Figure 4.4 Power ratio as function of repetition length, L_{rep}. The power ratios have been calculated using the Riemann sum procedure to evaluate the integrals. The upper axes indicate the number of subintervals, #.

Since the power ratio for the uniform layer should equal unity, the plot in Fig. 4.4(a) can be used to judge the Riemann sum procedure. Fig. 4.4(a) shows that α converges uniformly to unity, as expected, but that the convergence is slow: The power ratio evaluated with the Riemann procedure is concave with L_{rep}. To facilitate a comparison of the Riemann integration procedure with the procedure to be presented in the following section, the value of # and thereby also L_{rep} at which the power ratio deviates less than one percent from the analytical value is determined as $\# = 742$ or equivalently $L_{\text{rep}} = 1.15\,\text{mm}$.

Concerning the power ratio for the waveguide layer, the analytical value is not known, but by determining the power ratio with $\# = 10000$ sampling points an approximate "true" value can be obtained as $\alpha_{\text{g,tr}} = 0.906$. Using this "true" value, the number of intervals and the corresponding repetition length that yield a deviation of less than one percent may be calculated as $\# = 63$ and $L_{\text{rep}} = 97.7\,\mu\text{m}$.

By inspection of the integrands, namely the relatively slow variations for small values of s and ρ and the divergence near $s = nk_0$ and $\rho = n_1 k_0$, respectively, it can be concluded that an equidistant sampling of the integrand is not optimal. Rather, the sampling points should be positioned increasingly dense as s and ρ approach their respective singularities. Such a procedure is presented in the following section.

Compared to the results obtained for the closed geometry (Section 3.8) where no convergence was obtained the above results exhibit a convergence which evidently presents a great improvement. However, incentivized by the slow convergence, a more intelligent procedure for positioning the sampling points is presented in the following section, and the resulting convergence speed is compared to that obtained by use of the Riemann sum.

Non-Equidistant Points

Referring to the plots of the integrands in Fig. 4.3, it is seen that the sampling points should be placed increasingly dense as the singularities are approached. Such a non-equidistant spacing of the points could be carried out in several ways, but the symmetry-properties of the uniform layer presents a solution that both physically and mathematically provides an intuitive procedure for the choice of sampling points. In the following, this procedure is firstly described, and next it is applied to calculate the power ratios in the uniform and waveguide layers, respectively.

In the uniform layer, the dipole current source experiences an environment that is

completely symmetric in the xz-plane, that is, no direction in this plane can be preferred. Consequently, equal amounts of light are emitted in all directions in the xz-plane, and therefore any weighting between the contributions from the x- and z-propagation constants, s and γ, to the total propagation constant:

$$nk_0 = \sqrt{s^2 + \gamma^2}, \tag{4.46}$$

are equally important. This can be illustrated as in Fig. 4.5 where an (s, γ)-plane is indicated. The radius of the quarter circle equals the total propagation constant, nk_0, and by the convention of positive x- and z-propagation constants, only the first quadrant is needed for the description.

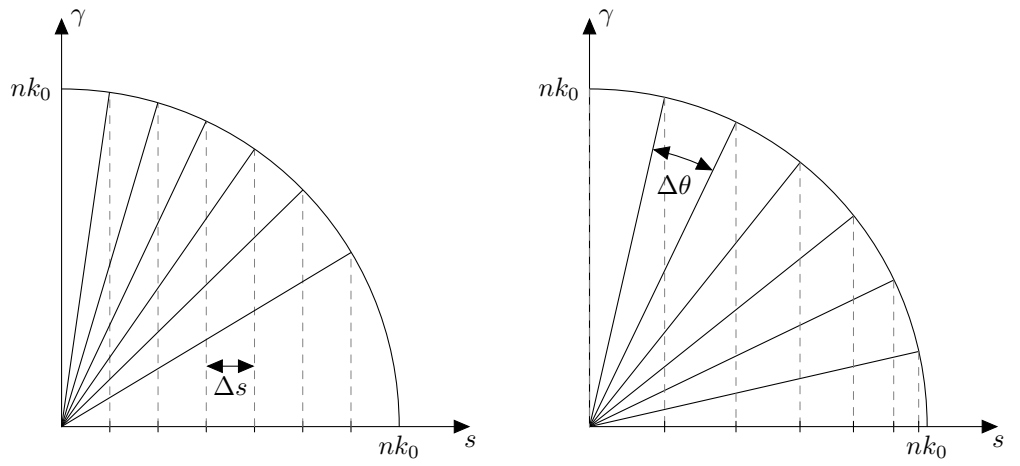

(a) Sampling: Equal s spacing.

(b) Sampling: Equal angular spacing.

Figure 4.5 Plot of Eq. (4.46) in the (s, γ)-plane where the quarter circle represents the total propagation constant, nk_0, in the uniform layer.

In Fig. 4.5(a), the equal s-spacing that was used in the previous section is indicated. The figure clearly illustrates that this sampling does not induce an equal weighting of all directions in the (s, γ)-plane, but favors certain directions. From this, it can be understood that the choice of s-values used in the Riemann sum is inexpedient.

Fig. 4.5(b) shows an equal angular spacing which ensures an equal weighting of all directions. It also illustrates that as s approaches nk_0 the spacing between the values of s decreases. In terms of the angle from the s-axis, θ, s is given as:

$$s = nk_0 \cos(\theta). \tag{4.47}$$

Thus, by choosing equidistant values of θ in the range:

$$\theta \in \left[0, \frac{\pi}{2}\right], \tag{4.48}$$

Eq. (4.47) gives non-equidistant and increasingly dense values of s as the singular end point is approached.

Strictly, the above description of the xz-plane symmetry holds only for the uniform layer and not for the waveguide layer because certain directions must be favored in

the waveguide layer. However, the waveguide layer can be considered as a perturbed uniform layer where the high-refractive index region is a minor perturbation of the infinite solution domain. In this picture, the θ-sampling must, if the refractive index contrast, $\Delta n \equiv n_2 - n_1$, and the core width, D, are not large, to some extent remain valid, and therefore this procedure is also applied for the waveguide layer. It is noted that the integrand for the waveguide layer qualitatively looks as the integrand for the uniform layer which further supports the use of the θ-procedure for the waveguide layer.

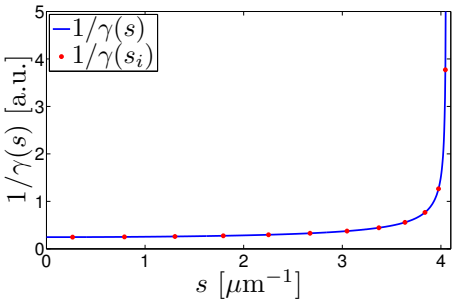

(a) Uniform layer. The integrand is $1/\gamma(s)$.

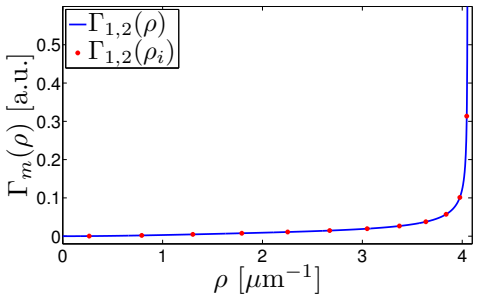

(b) Waveguide layer. The integrand is $\Gamma_m(\rho)$, defined in Eq. (4.43).

Figure 4.6 Integrands in expressions for P, see Eqs. (4.35a) and (4.43), in open geometry. The plots display the integrands as well as the non-equidistant sampling points given by Eq. (4.47).

The θ-sampling can be seen for the two types of layers in Figs. 4.6(a) and 4.6(b), respectively, with $\# = 12$ subintervals. The plots illustrate the non-equidistant spacing of the discrete s- and ρ-values. Using the same number of intervals as for the powers in Fig. 4.4, but now with the θ-sampling, shown in Fig. 4.6, the powers as functions of the number of intervals for the uniform layer and for the waveguide layer can be seen in Figs. 4.7(a) and 4.7(b), respectively. As the sampling is non-equidistant, the results can no longer be compared to the repetition length.

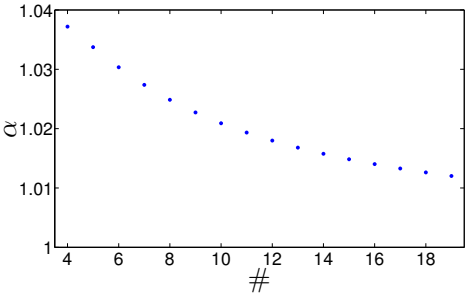

(a) Uniform layer.

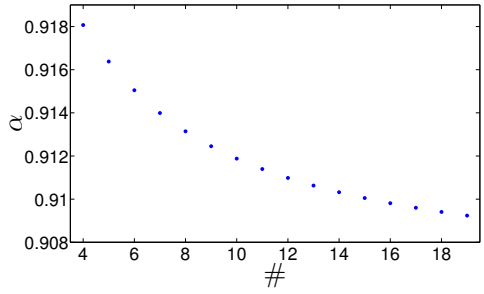

(b) Waveguide layer.

Figure 4.7 Power ratios as functions of number of included sampling points. The power ratios have been calculated using the non-equidistant sampling procedure given in Eq. (4.47).

Comparing firstly the results for the vacuum layer with those obtained with the Riemann sum procedure, it is seen that the power ratio converges to unity, and in particular that faster convergence is obtained with the non-equidistant spacing of the

s-values: With $\# = 24$ intervals, the error is less than one percent. For the waveguide layer, faster convergence is also obtained, and comparing again with the "true" value, $\alpha_{\mathrm{g,tr}} = 0.906$, it is found that $\# = 7$ gives an error of less than one percent.

In conclusion, the non-equidistant spacing of the sampling values of s and ρ has proven to deliver a much faster convergence than the Riemann sum procedure. Since, as earlier stated, the determination of the power ratio is essentially a matter of approximating the radiation mode contribution, this fast convergence is highly desirable. The convergence studies for the two methods for approximating the integrals have also unveiled another interesting point: For both methods, the convergence is faster for the waveguide layer than for the uniform layer. For the uniform layer, the integral is the only contribution to the power, and hence the result is critically dependent on the approximation of the integral. For the waveguide layer, the power is made up of a sum-contribution from the guided modes and an integral-contribution from the radiation modes. Since the waveguide layer convergence is obtained for a comparatively smaller number of subintervals, a significant part of the emitted power must be due to the guided modes.

The overall picture for both of the procedures applied to calculate the power is that uniform convergence is obtained. Compared to the corresponding results for the closed geometry approach, this is a significant improvement, and the choice of procedure for approximating the integrals in the open geometry is largely a matter of the speed of the uniform convergence. The results in this section illustrate a major superiority of the open geometry approach compared to the closed geometry approach, namely that the normalized SER can be determined unambiguously using the open geometry approach. As earlier discussed, the difference in the determination of the power in the closed and open geometry approaches is essentially the treatment of the contributions from the semi-radiating and radiating modes, respectively. From the converging results in the open geometry approach, it is concluded that the open geometry treatment of the radiation modes is more realistic and accurate than the corresponding closed geometry treatment.

4.7 Summary

This chapter has introduced the open geometry approach, and in this first introductory chapter single-layers have been treated. The next chapter presents and analyzes the more interesting and advanced open two-layer geometry.

The open geometry has essentially been introduced as the limiting case of the closed geometry when the width of the geometry tends to infinity. Physically, this prompts that the electric field is nowhere forced to vanish, and hence the outer BCs that were introduced for the closed geometry do not exist for the open geometry.

Specifically, a uniform open layer and a waveguide open layer have been analyzed. In the uniform layer, no BCs exist, and therefore no constraints are put on the real x-propagation constants, s, of the layer which accordingly form a continuum in the range $]0, \infty[$. Consequently, no guided modes, but only radiation modes exist in such a layer. Since these radiation modes are oscillatory along the entire x-axis, a new normalization procedure was introduced, utilizing the Dirac delta function. In the waveguide layer, both a finite number of discrete guided modes and a continuum of radiation modes exist. The normalization of the guided modes was carried out as for the closed geometry, whereas the normalization of the waveguide layer radiation modes proved to be given, in essence, as for the radiation modes of the uniform layer.

Next, a number of orthogonality and completeness relations involving the modes in the different types of open geometry layers were presented, and these play a central role

in the treatment of the open two-layer geometry in the next chapter. Following this, the expansion of the electric field on the eigenmodes was introduced.

In the determination of expressions for the normalized SER, as for the closed geometry due to a dipole current source, the electric field expansions were applied, and the expressions for the power ratio in the uniform layer and in the waveguide layer contained improper integrals. The expression for the power in the uniform layer had an analytical value, and in both the closed and open geometries this power is used as the reference power. The improper integral in the expression for the power in the waveguide layer had no immediate analytical solution, and the determination of the emitted power in the waveguide was consequently a matter of obtaining a precise approximation to this integral. To this end, two different numerical approaches, namely a Riemann sum approach and a non-equidistant sampling approach, were introduced. Both approaches displayed uniform convergence, but the non-equidistant approach at a much faster rate. Still, the SER results essentially converged, regardless of integral-approximation approach, and compared to the corresponding results for the closed geometry this represents a significant improvement. The improved results in the open geometry approach were, in particular, explained by and attributed to the treatment of the radiation modes.

Chapter 5

Open Geometry: Two Layers

5.1 Introduction

This chapter focuses on the special case of light emission from an abruptly terminated symmetric slab waveguide into a uniform medium in the open geometry approach. The situation is sketched in Fig. 5.1 where a waveguide layer and a uniform layer have been brought together at $z = 0$. The waveguide and uniform layers are termed layer 1 and 2, respectively. For simplicity, it is assumed that the waveguide supports only the fundamental mode, $U_1(x)$, which limits this treatment to thin waveguide cores and low index contrasts $\Delta n = n_2 - n_1$. The refractive index of the uniform layer, n_0, is arbitrary.

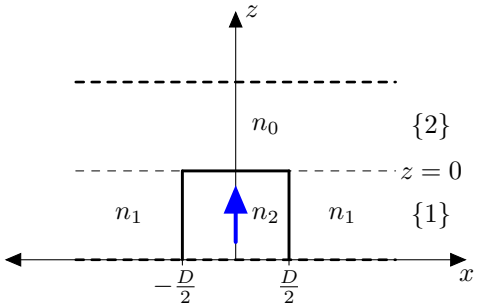

Figure 5.1 Abruptly terminated symmetric waveguide in the open geometry, illustrated in an xz-plane.

As will be discussed at the end of this chapter, the determination of reflection and transmission coefficients offers a direct and intuitive route to calculations of the normalized SER in multi-layered open structures. Therefore, the open two layer problem is of significant interest since its treatment inevitably involves calculation of reflection and transmission coefficients between the two layers. In this treatment, light is assumed incident on the interface from the waveguide layer whereby two scenarios must be considered, namely an incident guided mode and an incident radiation mode. Consequently, only reflection and transmission coefficients from layer 1 to layer 2 will be obtained.

The treatment of an incident guided mode in Section 5.2 is largely inspired by the works in [Tigelis]. The further treatment of an incident radiation mode in Section 5.3 is a direct extension of the procedures in Section 5.2, but includes new features due to the oscillatory nature of the radiation modes. Throughout this chapter, all modes are

assumed normalized with respect to the $L^2(\mathbb{R})$ inner product to follow the convention in [Tigelis].

5.2 Illumination by Fundamental Mode

Illuminating the structure in Fig. 5.1 along the positive z-direction with the fundamental and guided mode, $U_1(x)$, results in reflection and transmission at the layer interface at $z = 0$. Specifically, part of the incident mode is reflected back into itself and into the continuum of radiation modes, $\psi_m(x, \rho)$. Similarly, part of the incident mode is transmitted across the interface and couple into the continuum of uniform layer radiation modes, $\phi_l(x, s)$. Following the expansion of the field specified in Eqs. (4.26) and (4.27), the field on either side of the interface, $E_1(x, z)$ and $E_2(x, z)$, respectively, can be expressed as [Tigelis, Eq. (9)]:

$$E_1(x,z) = U_1(x)\left[\exp(-i\beta_1 z) + R_1 \exp(i\beta_1 z)\right] + \sum_{m=1}^{2} \int_0^\infty R(\rho)\psi_m(x,\rho)\exp(i\beta(\rho)z)\,\mathrm{d}\rho, \tag{5.1a}$$

$$E_2(x,z) = \sum_{l=1}^{2} \int_0^\infty T(s)\phi_l(x,s)\exp(-i\gamma(s)z)\,\mathrm{d}s, \tag{5.1b}$$

where the coefficients R_1, $R(\rho)$ and $T(s)$ represent reflection into the guided mode, reflection into the waveguide radiation modes and transmission into the uniform layer radiation modes, respectively. The reflection coefficient $R(\rho)$ generally depends on m, but since a symmetric waveguide is considered, and since the incident mode is the symmetric and even fundamental mode, the reflection to the $m = 1$ and $m = 2$ radiation modes, respectively, must be equal on symmetry grounds. A similar argument applies to the transmission coefficients $T(s)$ for which the l-dependence is therefore omitted.

Application of z-BCs: Fredholm Equation of the Second Kind

As in the closed geometry, the field is required to remain continuous and differentiable everywhere and in particular across any interface. Applying the continuity demand at $z = 0$, and using the orthogonality properties given in Eqs. (4.24) gives the reflection and transmission coefficients in terms of the field at $z = 0$, the aperture field, $\Phi(x)$:

$$\boxed{\begin{aligned} R_1 &= -1 + \int_{-\infty}^{\infty} \Phi(x)U_1(x)^*\,\mathrm{d}x, && \text{(5.2a)}\\ R(\rho) &= \int_{-\infty}^{\infty} \Phi(x)\psi_m(x,\rho)^*\,\mathrm{d}x, \quad m = 1,2, && \text{(5.2b)}\\ T(s) &= \int_{-\infty}^{\infty} \Phi(x)\phi_l(x,s)^*\,\mathrm{d}x, \qquad l = 1,2. && \text{(5.2c)} \end{aligned}}$$

The derivations of the expressions in Eqs. (5.2) are contained in Appendix E.1. Since $\phi_l(x, s)$ is a complex exponential, the expression in Eq. (5.2c) indicates that the transmission coefficients essentially can be thought of as the Fourier transform of the aperture field in the propagation constant s.

A Fredholm equation of the first kind [Baker, p. 33] for $\Phi(x)$ can be obtained by applying the differentiability demand at $z = 0$ to Eqs. (5.1) while inserting the expressions

for R_1, $R(\rho)$ and $T(s)$ from Eqs. (5.2). The Fredholm equation of the first kind can be converted to a Fredholm equation of the second kind by creative application of the completeness relations in Eqs. (4.24e) and (4.24f). The details of the derivation of this integral equation can be found in Appendix E.1, and the resulting Fredholm equation of the second kind is:

$$\boxed{\Phi(x) = \Phi_0(x) + \lambda \int_{-\infty}^{\infty} \Phi(x') K(x, x') \, \mathrm{d}x',} \tag{5.3a}$$

where the zeroth order aperture field, $\Phi_0(x)$, the integral prefactor, λ, and the kernel, $K(x, x')$, are:

$$\Phi_0(x) = \frac{2U_1(x)\beta_1}{k_0(n_0 + n_1)}, \tag{5.3b}$$

$$\lambda = \frac{-1}{k_0(n_0 + n_1)}, \tag{5.3c}$$

$$\begin{aligned} K(x, x') = {} & [\beta_1 - k_0 n_1] \, U_1(x) U_1(x')^* + \sum_{m=1}^{2} \int_0^{\infty} [\beta(\rho) - k_0 n_1] \, \psi_m(x, \rho) \psi_m(x', \rho)^* \, \mathrm{d}\rho \\ & + \sum_{l=1}^{2} \int_0^{\infty} [\gamma(s) - k_0 n_0] \, \phi_l(x, s) \phi_l(x', s)^* \, \mathrm{d}s. \end{aligned} \tag{5.3d}$$

In this context, it is noted that the expression for the Fredholm equation in [Tigelis, Eq. (14)] is erroneous, in that it does not include the prefactor λ. The ensuing expressions for the first and second order aperture fields are, however, correct.

The solution to the Fredholm equation is given as a Liouville-Neumann series [Tigelis, Baker, p. 34]:

$$\Phi(x) = \lim_{N \to \infty} \Big\{ \Phi_0(x) + \lambda^N \sum_{j=1}^{N} C_j(x) \Big\}, \tag{5.4a}$$

where the jth term in the sum is given by:

$$C_j(x) = \int_{-\infty}^{\infty} \dots \int_{-\infty}^{\infty} \int_{-\infty}^{\infty} K(x, x_1) \dots K(x_{j-1}, x_j) \Phi_0(x_j) \, \mathrm{d}x_1 \dots \, \mathrm{d}x_{j-1} \, \mathrm{d}x_j. \tag{5.4b}$$

Under the restrictions given in [Baker, p. 35], the series is uniformly convergent, and so only a finite number of the terms of $C_j(x)$ are necessary to evaluate a valid approximation of $\Phi(x)$. Assuming that the refractive indices of the waveguide layer, n_1 and n_2, are near-identical ($n_1 \approx n_2$), it may be justified to only include a single term in the approximation [Tigelis]. The first order approximation of the aperture field, $\Phi_1(x)$, is readily found by evaluating Eq. (5.4a) with $N = 1$ rather than $\lim_{N \to \infty}$:

$$\Phi_1(x) = \Phi_0(x) + \lambda C_1(x) = \Phi_0(x) + \lambda \int_{-\infty}^{\infty} K(x, x') \Phi_0(x') \, \mathrm{d}x'. \tag{5.4c}$$

In the following section, first order expressions for the aperture field and for the reflection and transmission coefficients are derived.

Evaluation of the First Order Aperture Field and Coefficients

The first order aperture field can be expressed explicitly by insertion of $\Phi_0(x')$ and $K(x,x')$ into Eq. (5.4c) which yields:

$$\Phi_1(x) = \Phi_0(x) - c\Bigg\{U_1(x)\left[\beta_1 - k_0 n_1\right] + \sum_{l=1}^{2}\int_0^\infty \left[\gamma(s) - k_0 n_0\right]\phi_l(x,s)\langle U_1, \phi_l(s)\rangle_{L^2}\,\mathrm{d}s\Bigg\}, \tag{5.5}$$

where the constant c is:

$$c = \frac{2\beta_1}{k_0^2(n_0+n_1)^2}, \tag{5.6}$$

and where the orthogonality property in Eqs. (4.24a) and (4.24d) have been applied to arrive at the result. $\langle U_1, \phi_l(s)\rangle_{L^2}$ denotes the overlap integral in $L^2(\mathbb{R})$-space between the fundamental mode, $U_1(x)$, and a uniform layer radiation mode, $\phi_l(x,s)$. The overlap integral is defined by the $L^2(\mathbb{R})$ inner product as:

$$\langle U_1, \phi_l(s)\rangle_{L^2} = \int_{-\infty}^{\infty} U_1(x)\phi_l(x,s)^*\,\mathrm{d}x. \tag{5.7}$$

Appendix E.3 expresses the overlap integral $\langle U_1, \phi_l(s)\rangle_{L^2}$. In this appendix, it is shown that $\langle U_1, \phi_1(s)\rangle_{L^2} = \langle U_1, \phi_2(s)\rangle_{L^2}$, resulting from $U_1(x)$ being an even function in x.

Having obtained the first order aperture field, $\Phi_1(x)$, the appertaining first order reflection and transmission coefficients are evaluated by insertion of $\Phi_1(x)$ into Eqs. (5.2). Using the orthogonality properties in Eqs. (4.24a)-(4.24d), the first order coefficients, $R_1^{(1)}$, $R^{(1)}(\rho)$ and $T^{(1)}(s)$, are determined:

$$R_1^{(1)} = -1 - c\Big\{\beta_1 - k_0(n_0+2n_1) + \sum_{l=1}^{2}\int_0^\infty \left[\gamma(s) - k_0 n_0\right]\left|\langle U_1, \phi_l(s)\rangle_{L^2}\right|^2\,\mathrm{d}s\Big\}, \tag{5.8a}$$

$$R^{(1)}(\rho) = -c\sum_{l=1}^{2}\int_0^\infty \left[\gamma(s) - k_0 n_0\right]\langle \phi_l(s), \psi_m(\rho)\rangle_{L^2}\langle U_1, \phi_l(s)\rangle_{L^2}\,\mathrm{d}s, \tag{5.8b}$$

$$T^{(1)}(s) = -c\langle U_1, \phi_l(s)\rangle_{L^2}\left[-2k_0(n_0+n_1) + \beta_1 + \gamma(s)\right]. \tag{5.8c}$$

The inner product $\langle \phi_l(s), \psi_m(\rho)\rangle_{L^2}$ is expressed in Appendix E.3, and using this $R^{(1)}(\rho)$ is expressed explicitly in Appendix E.5.

The following subsection examines the results obtained from calculations of the reflection and transmission coefficients as well as the field profile obtained from the open geometry approach.

Computational results

To verify that the expression for $R_1^{(1)}(\rho)$ (Eq. (5.8a)) is correct, it is beneficial to compare with existing results, such as [Tigelis, Fig. 2]. Using the same parameters as in this reference, namely a wavelength of $\lambda = 0.86\,\mu$m and refractive indices $n_0 = 1.0$, $n_1 = 3.24$ and $n_2 = 3.6$ for the uniform layer, the cladding and the core, respectively, the absolute

square of R_1 is computed and plotted as a function of the width of the waveguide, D, in Fig. 5.2(a) where exact agreement with [Tigelis, Fig. 2] is obtained.

In this context, it is noted that the D-range in [Tigelis] is in direct conflict with the assumption of only one guided mode: For the given wavelength and refractive indices, the waveguide changes from single-mode support to multi-mode support at approximately $D = 0.274\,\mu$m. Because the second guided mode is uneven, the results remain valid even when the waveguide supports two guided modes. However, upon inclusion of a third guided mode at $D = 0.549\,\mu$m, the results evidently become faulty. To accurately compute $R_1^{(1)}$ in a multi-mode waveguide, the Fredholm equation in Eqs. (5.3) should be re-derived starting from different field expansions (Eqs. (5.1)). The range $0.274\,\mu\text{m} < D < 1.0\,\mu$m in Fig. 5.2(a) is indicated by a dashed line to emphasize that the calculation is not representative in this range.

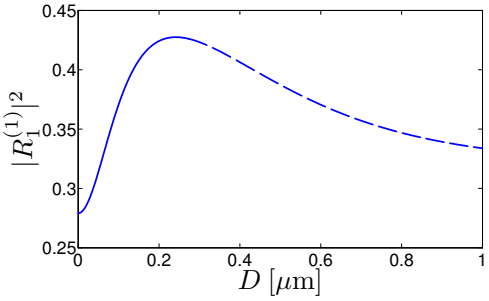

(a) $|R_1^{(1)}|^2$ as function of core width, D. The range of multiple guided modes is indicated by a dashed line. Setup parameters: $\lambda = 0.86\,\mu$m, $n_0 = 1.0$, $n_1 = 3.24$ and $n_2 = 3.6$.

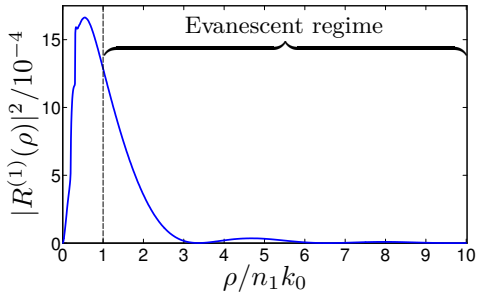

(b) $|R^{(1)}(\rho)|^2$ as function of ρ. The transition from propagating ρ-values to the evanescent regime is marked. Setup parameters: $n_0 = 1.0$, $n_1 = 3.24$, $n_2 = 3.6$ and $D = 0.15\,\mu$m. **The plot is incorrect due to errors in $\langle\psi(\rho), \phi(s)\rangle_{L^2}$ in non-revised version of report and errors in implementation of numerical integration of Eq.** (5.8b)**.**

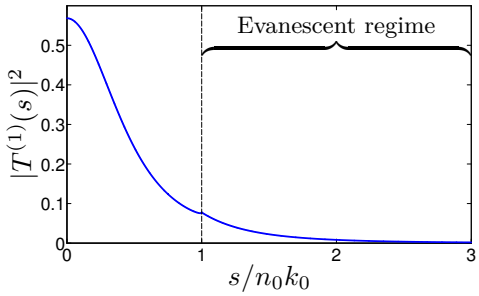

(c) $|T^{(1)}(s)|^2$ as function of s. The transition from propagating s-values to the evanescent regime is marked. Setup parameters: $n_0 = 1.0$, $n_1 = 3.24$, $n_2 = 3.6$ and $D = 0.15\,\mu$m. **The plot is incorrect due to error in $\langle\psi(\rho), \phi(s)\rangle_{L^2}$ in non-revised version of report.**

Figure 5.2 Reflection and transmission coefficients, $R_1^{(1)}$, $R^{(1)}(\rho)$ and $T^{(1)}(s)$.

Reflection into the radiation modes in the waveguide layer may be investigated by plotting the absolute square of $R^{(1)}(\rho)$ as function of ρ which is done in Fig. 5.2(b) for the setup parameters indicated in the figure caption. The choice of wavelength is

again $\lambda = 1.55\,\mu$m which is used as the wavelength henceforth. As expected, $R^{(1)}(\rho)$ tends to zero as ρ increases which is necessary for the field in layer 1 (Eq. (5.1a)) to be well-defined. The range $0 < \rho < n_1 k_0$ is of special interest as it determines the far-field radiation pattern. For values of $\rho > n_1 k_0$, the z-propagation constant, $\beta(\rho)$, is imaginary, cf. Eq. (4.7), and these radiation modes are consequently evanescent along z. Therefore, this range of ρ-values only affects the near-field pattern. A decreasing oscillatory behavior of $|R(\rho)|^2$ is observed in the near-field range. The oscillatory behavior can be accounted for by a closer inspection of Eq. (5.8b): The values of $R(\rho)$ depend on the overlap integral $\langle \phi_l(s), \psi_m(\rho) \rangle_{L^2}$ which can be expected to oscillate as the two eigenmodes, $\phi_l(s)$ and $\psi_m(\rho)$, move in and out of phase as ρ is varied. That $|R(\rho)|^2$ oscillates is noteworthy because it shows that coupling to the radiation modes is not monotonously decreasing in ρ, not even in the near field regime.

When computing the field profile from Eq. (5.1) numerically, special care must be taken to ensure that the propagating regime, $0 < \rho < n_1 k_0$, is sampled sufficiently densely, ensuring that the features of the far-field are well-modeled. Inclusion of ρ-values from the near-field regime, $\rho > n_1 k_0$, is necessary to obtain a continuous field across $z = 0$, but does not otherwise affect the field significantly.

The last coefficient to be considered is the transmission coefficient, $T^{(1)}(s)$. Again, the absolute square of the coefficient is plotted as function of the x-propagation constant, s, and the resulting plot can be seen in Fig. 5.2(c). Similar to the case of reflection into the waveguide radiation modes, the s-values can be separated into two ranges, namely the far-field range, $0 < s < n_0 k_0$, which describes the propagating waves, and the near-field range, $s > n_0 k_0$, which describes the evanescent waves. This separation is indicated in Fig. 5.2(c). The overall picture of $|T^{(1)}(s)|^2$ is that of a monotonously descending curve, with the exception of a small protrusion at the transition from the propagating to the evanescent regime. As for the reflection coefficients $R(\rho)$, it is essential to include a dense sampling of the propagating regime, $0 < s < n_0 k_0$, when evaluating the field in layer 2 numerically to obtain a well-modeled far-field pattern. As discussed on p. 62, the transmission coefficient represents the Fourier transform in s of the aperture field, and the plot therefore shows that the aperture field is dominated by the small propagation constants, that is, the aperture field is slowly varying in x.

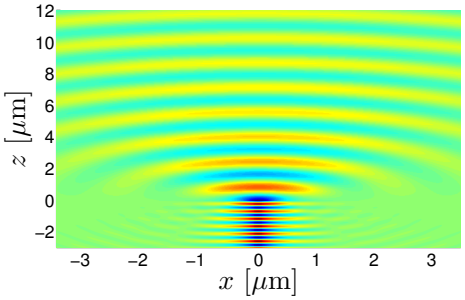

(a) Field profile due to an incident guided mode scattered at an abrupt waveguide-vacuum interface at $z = 0$. Setup parameters: $n_0 = 1.0$, $n_1 = 3.24$, $n_2 = 3.6$ and $D = 0.15\,\mu$m.

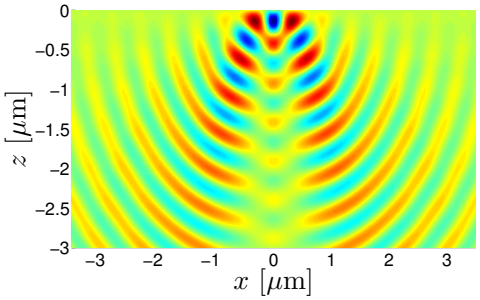

(b) Field profile of the radiation modes excited due to the reflection of the guided mode computed in Fig. 5.3(a).

Figure 5.3 Field profiles for open two-layer geometry, illuminated by fundamental mode. **Both field plots are not correct, due to having been plotted with erroneous formulas. The changes, however, are slight, and the plots are qualitatively the same.**

Finally, the field profile due to the incident guided mode is considered. Having obtained expressions and values for $R_1^{(1)}$, $R^{(1)}(\rho)$ and $T^{(1)}(s)$, the first order field can be approximated by insertion into Eq. (5.1). The improper integrals must necessarily be truncated in order to allow for a practical computation. Such a truncation can be justified on the basis of Figs. 5.2(b) and 5.2(c) since both coefficients tend to zero as ρ and s tend to infinity. Truncating the ρ-integral at $\rho = 6n_1k_0$ and the s-integral at $s = 4n_0k_0$ then allows for approximation of the integrals by use of e.g. a Riemann sum which has been applied in the present case. The resulting field profile can be seen in Fig. 5.3(a). An apparent improvement compared to the results from the closed geometry approach is observed as no parasitic reflections are visible. However, the results are qualitatively identical to those obtained using the closed geometry approach: In layer 1, the field is confined to the waveguide region whereas the field in layer 2 disperses from the aperture as near-spherical waves.

It should be noted, that the quality of the open geometry field plot depends critically on the numbers of included sampling points that have been chosen as 1500 and 1200 for the ρ- and s-integrals, respectively. A small number of sampling points results in a correspondingly shorter repetition length, c.f. Eq. (4.44), and resulting low quality field plots. However, much smaller numbers than the presently used can be applied with excellent results.

From Fig. 5.3(a) it is clear that the significance of the excited radiation modes are inferior compared to the incident and reflected guided mode, as the field in layer 1 is dominated by the guided mode. The contribution from the radiation modes in layer 1 is plotted in Fig. 5.3(b), to more clearly display the features of the radiation pattern given by the integral term in Eq. (5.1a). From Fig. 5.3(b), it is seen that the radiation pattern is mostly a local contribution to the total field, and that the effects of the reflected radiation modes diminishes and disperses as they propagate away from the reflection-interface. However, the radiation modes must be included to accurately model reflection away from the core region.

5.3 Illumination by Radiation Mode

Whereas the preceding section considered illumination of the geometry in Fig. 5.1 with the fundamental guided mode, the present section will treat illumination with an arbitrary radiation mode, $\psi_{\hat{m}}(x, \hat{\rho})$, $\hat{m} \in \{1, 2\}$, $\hat{\rho} \in]0, \infty[$. It should be noted that the radiation mode index, m, and the corresponding propagation constant, ρ, have been assigned a "hat"-notation to clearly distinguish the illumination mode from other radiation modes.

As a consequence of the illumination choice, the field in layer 1 consists of the illuminating radiation mode and the part of the illumination mode that is reflected back into the guided mode and into the other radiation modes. Likewise, the field in layer 2 consists of the part of the illuminating radiation mode transmitted into the uniform layer radiation modes. Using again expansions of the field, given by Eqs. (4.26) and (4.27), the field on either side of the interface, $\mathcal{E}_1(x, z)$ and $\mathcal{E}_2(x, z)$, may be expressed in a manner

similar to Eqs. (5.1):

$$\mathcal{E}_1(x,z) = \psi_{\hat{m}}(x,\hat{\rho})\exp(-i\beta(\hat{\rho})z) + \mathcal{R}_{1,\hat{m}}(\hat{\rho})U_1(x)\exp(i\beta_1 z) + \sum_{m=1}^{2}\int_0^\infty \mathcal{R}_{m,\hat{m}}(\rho,\hat{\rho})\psi_m(x,\rho)\exp(i\beta(\rho)z)\,\mathrm{d}\rho, \tag{5.9a}$$

$$\mathcal{E}_2(x,z) = \sum_{l=1}^{2}\int_0^\infty \mathcal{T}_{l,\hat{m}}(s,\hat{\rho})\phi_l(x,s)\exp(-i\gamma(s)z)\,\mathrm{d}s, \tag{5.9b}$$

where $\mathcal{R}_{1,\hat{m}}(\hat{\rho})$, $\mathcal{R}_{m,\hat{m}}(\rho,\hat{\rho})$, and $\mathcal{T}_{l,\hat{m}}(s,\hat{\rho})$ represent reflection into the guided mode, reflection into the waveguide layer radiation modes, and transmission to the uniform layer radiation modes, respectively. These coefficients are dependent on the illumination mode, $\psi_{\hat{m}}$, which explains the subscripts $\hat{m}$ and dependence on $\hat{\rho}$, and generally the subscripts m and l cannot be omitted in this case, as the illuminating mode is asymmetric.

Application of z-BCs: Fredholm Equation of the Second Kind

Demanding again that the electric field is continuous at $z = 0$, and using the orthonormality relations in Eqs. (4.24c) and (4.24d), the following expressions for $\mathcal{R}_{1,\hat{m}}(\hat{\rho})$, $\mathcal{R}_{m,\hat{m}}(\rho,\hat{\rho})$, and $\mathcal{T}_{l,\hat{m}}(s,\hat{\rho})$, given in terms of the aperture field at $z = 0$, $\Theta_{\hat{m}}(x,\hat{\rho})$, are derived in Appendix E.4:

$$\boxed{\begin{aligned}\mathcal{R}_{1,\hat{m}}(\hat{\rho}) &= \int_{-\infty}^{\infty}\Theta_{\hat{m}}(x,\hat{\rho})U_1(x)^*\,\mathrm{d}x, &(5.10a)\\ \mathcal{R}_{m,\hat{m}}(\rho,\hat{\rho}) &= \int_{-\infty}^{\infty}\Theta_{\hat{m}}(x,\hat{\rho})\psi_m(x,\rho)^*\,\mathrm{d}x - \delta_{\hat{m}m}\delta(\hat{\rho}-\rho), &(5.10b)\\ \mathcal{T}_{l,\hat{m}}(s,\hat{\rho}) &= \int_{-\infty}^{\infty}\Theta_{\hat{m}}(x,\hat{\rho})\phi_l(x,s)^*\,\mathrm{d}x. &(5.10c)\end{aligned}}$$

The term $\delta_{\hat{m}m}\delta(\hat{\rho}-\rho)$ in the expression for $\mathcal{R}_{m,\hat{m}}(\rho,\hat{\rho})$ represents reflection into the illumination radiation mode since this term only contributes to the field in layer 1 (Eq. (5.9a)) when $\psi_m(x,\rho) = \psi_{\hat{m}}(x,\hat{\rho})$.

As for illumination by a guided mode, treated in the previous sections, application of the demand of differentiability at $z = 0$ and the expressions in Eqs. (5.10) yield a first order Fredholm equation, and further application of the completeness relations in Eqs. (4.24e) and (4.24f) transforms this into a second order Fredholm equation:

$$\boxed{\Theta_{\hat{m}}(x,\hat{\rho}) = \Theta_{0,\hat{m}}(x,\hat{\rho}) + \lambda\int_{-\infty}^{\infty}\Theta_{\hat{m}}(x',\hat{\rho})\mathcal{K}(x,x')\,\mathrm{d}x',} \tag{5.11a}$$

where:

$$\Theta_{0,\hat{m}}(x,\hat{\rho}) = \frac{2\beta(\hat{\rho})\psi_{\hat{m}}(x,\hat{\rho})}{k_0(n_0+n_1)}, \tag{5.11b}$$

$$\mathcal{K}(x,x') = U_1(x)U_1(x')^*(\beta_1 - n_1k_0) + \sum_{m=1}^{2}\int_0^\infty \psi_m(x,\rho)\psi_m(x',\rho)^*(\beta(\rho)-n_1k_0)\,\mathrm{d}\rho + \sum_{l=1}^{2}\int_0^\infty \phi_l(x,s)\phi_l(x',s)^*(\gamma(s)-n_0k_0)\,\mathrm{d}s, \tag{5.11c}$$

are the zeroth order aperture field and the kernel of the second order Fredholm equation, respectively. The integral prefactor, λ, is given in Eq. (5.3c). The above equations are derived in Appendix E.4.

The solution to this Fredholm equation is given by the scheme in Eqs. (5.4) with the changes from $\Phi_0(x) \to \Theta_{0,\hat{m}}(x,\hat{\rho})$ and $K(x,x') \to \mathcal{K}(x,x')$. In the following section, the first order aperture field and the first order reflection and transmission coefficients are expressed.

Evaluation of the First Order Aperture Field and Coefficients

The first order aperture field, $\Theta_{1,\hat{m}}(x,\hat{\rho})$, resulting from illumination by an arbitrary radiation mode, $\psi_{\hat{m}}(x,\hat{\rho})$, is given by the expression in Eq. (5.4c) with the change from $\Phi_0(x) \to \Theta_{0,\hat{m}}(x,\hat{\rho})$ and $K(x,x') \to \mathcal{K}(x,x')$. Applying the orthogonality relations in Eqs. (4.24b) and (4.24d), the following expression is obtained:

$$\Theta_{1,\hat{m}}(x,\hat{\rho}) = \Theta_{0,\hat{m}}(x,\hat{\rho}) - \mathcal{C}\Bigg\{\psi_{\hat{m}}(x,\hat{\rho})(\beta(\hat{\rho}) - n_1 k_0) + \sum_{l=1}^{2}\int_0^\infty \phi_l(x,s)(\gamma(s) - n_0 k_0)\langle \psi_{\hat{m}}(\hat{\rho}), \phi_l(s)\rangle_{L^2}\,\mathrm{d}s\Bigg\}, \tag{5.12}$$

where:

$$\mathcal{C} = \frac{2\beta(\hat{\rho})}{k_0^2(n_0+n_1)^2}. \tag{5.13}$$

By insertion of the first order aperture field in Eq. (5.12) into the expressions in Eqs. (5.10), expressions for the first order reflection and transmission coefficients are obtained:

$$\mathcal{R}^{(1)}_{1,\hat{m}}(\hat{\rho}) = -\mathcal{C}\sum_{l=1}^{2}\int_0^\infty \langle \psi_{\hat{m}}(\hat{\rho}), \phi_l(s)\rangle_{L^2}\langle \phi_l(s), U_1\rangle_{L^2}(\gamma(s) - k_0 n_0)\,\mathrm{d}s, \tag{5.14a}$$

$$\mathcal{R}^{(1)}_{m,\hat{m}}(\rho,\hat{\rho}) = \delta_{m\hat{m}}\delta(\rho-\hat{\rho})\left\{\mathcal{C}\left[k_0(2n_1+n_0) - \beta(\hat{\rho})\right] - 1\right\} - \mathcal{C}\sum_{l=1}^{2}\int_0^\infty \langle \psi_{\hat{m}}(\hat{\rho}), \phi_l(s)\rangle_{L^2}\langle \phi_l(s), \psi_m(\rho)\rangle_{L^2}[\gamma(s) - k_0 n_0]\,\mathrm{d}s, \tag{5.14b}$$

$$\mathcal{T}^{(1)}_{l,\hat{m}}(s,\hat{\rho}) = \mathcal{C}\langle \psi_{\hat{m}}(\hat{\rho}), \phi_l(s)\rangle_{L^2}[2k_0(n_0+n_1) - \beta(\hat{\rho}) - \gamma(s)]. \tag{5.14c}$$

As for illumination by a guided mode, the reflection and transmission coefficients may be expressed explicitly in finite terms and Dirac delta terms using the expression for the overlap integral between the waveguide layer and uniform layer radiation modes, $\langle \psi_m(\rho), \phi_l(s)\rangle_{L^2}$, introduced in Appendix E.3. These expressions can be found in Appendix E.5.

The following section presents computational results for the first order expressions that have been derived and discussed in this section.

Computational results

This section contains the first computational results for illumination by a radiation mode. The numerical investigations of the first order expressions, derived in the preceding section

(Eqs. (5.12) and (5.14)), will establish that the aperture field is undefined, and that the reflection and transmission coefficients consequently do not, as expected, converge to zero. As discussed in the following, the current status of this point of the project is therefore not conclusive, and more work and time is needed to resolve the issue.

The practical implementation in MATLAB of the expression for the aperture field is carried out by approximating the integral with a sum and by truncating this sum at some finite value of the integration variable, s. This procedure is evidently critically dependent on the integrand to converge to zero as s increases. To investigate this requirement, the integral in Eq. (5.12) may be rewritten using the expression for the inner product $\langle \psi_{\hat{m}}(\hat{\rho}), \phi_l(s) \rangle_{L^2}$ that was introduced in Eq. (E.43):

$$\begin{aligned}
&\int_0^\infty \phi_l(x,s)(\gamma(s) - n_0 k_0) \langle \psi_{\hat{m}}(\hat{\rho}), \phi_l(s) \rangle_{L^2} \, \mathrm{d}s \\
&\qquad = \int_0^\infty \phi_l(x,s)(\gamma(s) - n_0 k_0) \{ G_{\hat{m},l}(\hat{\rho}) \delta(\hat{\rho} - s) + H_{\hat{m},l}(\hat{\rho}, s) \} \, \mathrm{d}s \\
&\qquad = G_{\hat{m},l}(\hat{\rho}) \phi_l(x,\hat{\rho})(\gamma(\hat{\rho}) - n_0 k_0) + \int_0^\infty \phi_l(x,s)(\gamma(s) - n_0 k_0) H_{\hat{m},l}(\hat{\rho}, s) \, \mathrm{d}s \\
&\qquad \equiv G_{\hat{m},l}(\hat{\rho}) \phi_l(x,\hat{\rho})(\gamma(\hat{\rho}) - n_0 k_0) + \int_0^\infty J_l(s) \, \mathrm{d}s,
\end{aligned} \tag{5.15}$$

with:

$$J_l(s) = \phi_l(x,s)(\gamma(s) - n_0 k_0) H_{\hat{m},l}(\hat{\rho}, s). \tag{5.16}$$

$J_l(s)$ is also function of $\hat{m}$ and $\hat{\rho}$, but these dependences have been omitted in the notation as they are of no significance for the following. As discussed above, the numerical procedure for approximating the integrals is only valid if $J_l(s)$ converges to zero as s increases. Therefore, to illustrate the problem the real and imaginary parts of $J_l(s)$ are plotted with $l = 1, x = 1\,\mu\mathrm{m}, \hat{m} = 1$, and $\hat{\rho} = 1.5\,\mu\mathrm{m}^{-1}$ in Fig. 5.4(a).

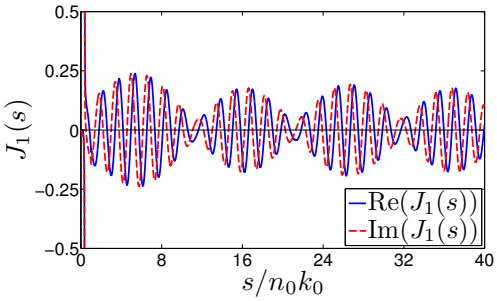

(a) Integrand of s-integral, $J_l(s)$, defined in Eq. (5.16), that defines the first order aperture field, $\Theta_{1,\hat{m}}(x,\hat{\rho})$

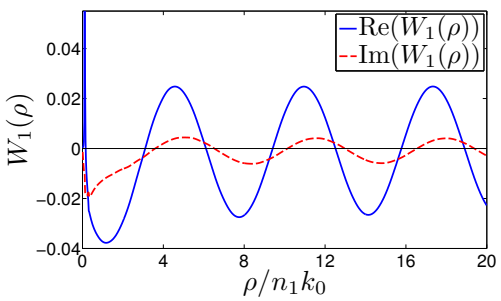

(b) Non-Dirac delta function terms, $W_l(\rho)$, in expression for $\mathcal{R}^{(1)}_{m,\hat{m}}(\rho,\hat{\rho})$, defined in Eq. (5.17).

Figure 5.4 Plots of first order results for illumination by radiation mode. The geometry parameters are as in Fig. 5.3(a).

The plot shows that the integrand does not converge to zero as s increases, but rather it oscillates. The choices of parameters ($l, x, \hat{m}$, and $\hat{\rho}$) are arbitrary, but investigations with different values give the same conclusion: The integrand does not converge. This entails

that the s-integral that defines the first order aperture field in Eq. (5.12) is divergent, or put differently, that the aperture field is undefined, in contradiction with the very well-defined physical problem of an incident radiation mode. Consequently, the treatment of the reflection and transmission coefficients, derived directly from the aperture field, cf. Eqs. (5.14), is expected to suffer from numerical problems as well. This is analyzed and confirmed in the following.

In the expression for $\mathcal{R}^{(1)}_{m,\hat{m}}(\rho,\hat{\rho})$ in Eq. (E.60b), focus is put on the terms that do not contain the Dirac delta function which are:

$$\begin{aligned}\sum_{l=1}^{2} W_l(\rho) \equiv \sum_{l=1}^{2} \mathcal{C}\Bigg\{ & G_{\hat{m},l}(\hat{\rho}) H_{m,l}(\rho,\hat{\rho})^* \left[\gamma(\hat{\rho}) - k_0 n_0\right] \\ & + G_{m,l}(\rho)^* H_{\hat{m},l}(\hat{\rho},\rho) \left[\gamma(\rho) - k_0 n_0\right] \\ & + \int_0^\infty H_{\hat{m},l}(\hat{\rho},s) H_{m,l}(\rho,s)^* \left[\gamma(s) - k_0 n_0\right] \,\mathrm{d}s \Bigg\}, \end{aligned} \tag{5.17}$$

where again the dependence on $\hat{m}$ and $\hat{\rho}$ has been omitted. Using $l = 1, x = 1\,\mu\mathrm{m}, \hat{m} = 1$, and $\hat{\rho} = 1.5\,\mu\mathrm{m}^{-1}$, the real and imaginary parts of $W_l(\rho)$ have been plotted in Fig. 5.4(b). The plot illustrates that the reflection coefficient does not converge to zero, but rather it oscillates, and since investigations with other choices of the parameters ($l, x, \hat{m}$, and $\hat{\rho}$) yield the same oscillatory behavior, this is a general issue. Consequently, truncation of the semi-infinite ρ-integral that defines the electric field in layer 1 (Eq. (5.9a)) is precluded, entailing that the electric field is nowhere finite.

Due to the time limitations of the project, the above numerical problems have not been resolved, but instead potential explanations are given in the following.

The results obtained for illumination by a guided mode (Section 5.2) did not exhibit the same numerical problems since the reflection and transmission coefficients converged as expected. Likewise, the electric field was continuous and differentiable across the interface at $z = 0$ which establishes that the overlap integrals, $\langle \phi_l(s), U_1 \rangle_{L^2}$ and $\langle \psi_m(\rho), \phi_l(s) \rangle_{L^2}$, that implicitly determine the field on either side of the interface (Eqs. (5.1) and (5.8)) have been derived and implemented correctly. Hence, mistakes in these, in particular in $\langle \psi_m(\rho), \phi_l(s) \rangle_{L^2}$, are not likely to be responsible for the numerical problems in the evaluation of $\Theta_{1,\hat{m}}(x,\hat{\rho})$.

Focus may instead be put on the derivation of the expression for the first order aperture field, that is the result of a truncated Liouville-Neumann series solution to the Fredholm equation of the second kind in Eqs. (5.11). As stated on p. 63, the series solution to the integral equation is uniformly convergent when the conditions in [Baker, p. 35] are fulfilled. Until this point, these conditions have been assumed satisfied, and the results for illumination by the guided mode indicate that this assumption is valid. However, it cannot be eliminated that the assumption fails for illumination by a radiation mode, and that another procedure for solving the second order Fredholm equation in the aperture field is called for.

The derivations and implementation in MATLAB have been thoroughly controlled, and therefore these are unlikely to cause the problems, but it cannot be entirely left out of suspicion.

The following section presents an outline for the calculation of the SER in an open three-layer geometry. Due to the numerical problems encountered in this section, numerical results for the SER are, however, not obtained.

5.4 Spontaneous Emission Rate

Despite the numerical problems encountered in the evaluation of the reflection and transmission coefficients due to an incident radiation mode, it is still relevant to outline a procedure for obtaining the normalized SER in a multi-layered open geometry. Specifically, this section will focus on obtaining the power emitted from a dipole and through that the normalized SER in a geometry of three layers, as sketched in Fig. 5.5.

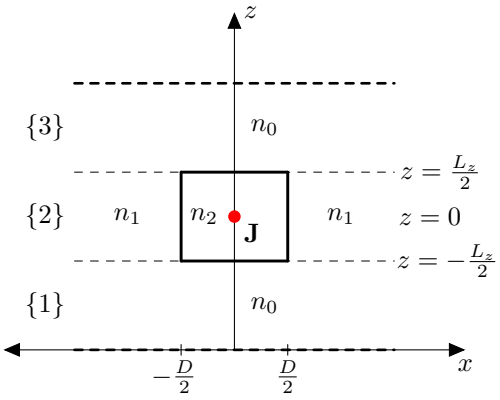

Figure 5.5 Dipole, **J**, embedded in a waveguide layer, surrounded by uniform layers. The dipole is placed at $(x, z) = (0, 0)$.

Initially, it is recalled that the power emitted from a dipole essentially is the real part of the electric field generated by the dipole at the position of the dipole, cf. Eq. (3.34). Obtaining the normalized SER in the open geometry, as in the closed geometry, consequently reduces to determining the electric field due to the dipole and the surrounding optical environment. To this end, the field emitted upwards from the dipole at $z = 0$, $E^{\uparrow}(x, 0)$, represented as in Eq. (4.27), is expressed as:

$$E^{\uparrow}(x,0) = \sum_{n=1}^{N_{\mathrm{g}}} \mathcal{A}_n^{\mathrm{g}} U_n(x) + \sum_{m=1}^{2} \int_0^{\infty} \mathcal{A}^{\mathrm{r}}(\rho)\psi_m(x,\rho)\,\mathrm{d}\rho. \tag{5.18}$$

To allow for a numerical treatment, a discretization of the integral term is desirable. Transforming the integral into a sum, by the introduction of a sampling of the continuous integration constant, ρ, produces a discretized expression for the electric field:

$$E^{\uparrow}(x,0) \simeq \sum_{n=1}^{N_{\mathrm{g}}} \mathcal{A}_n^{\mathrm{g}} U_n(x) + \sum_{m=1}^{2} \sum_{n=1}^{N_{\mathrm{r}}} \mathcal{A}^{\mathrm{r}}(\rho_n)\psi_m(x,\rho_n)\Delta\rho_n, \tag{5.19}$$

where the integral over the radiation modes has been discretized into N_{r} sampling points and truncated at the value $\rho_{N_{\mathrm{r}}}$. The distance between the sampling points, $\Delta\rho_n$, is assumed dependent on n to allow for non-equidistant sampling. The total number of guided modes is, to generalize the outline, assumed equal to N_{g} such that the total number of included modes is $M = N_{\mathrm{g}} + 2N_{\mathrm{r}}$. The modal amplitudes excited by the dipole current are termed $\mathcal{A}_n^{\mathrm{g}}$ and $\mathcal{A}^{\mathrm{r}}(\rho)$ for the guided and radiation modes, respectively, see Eq. (4.31). On symmetry grounds, excitations into $m = 1$th and $m = 2$nd radiation mode are the same, and no distinction is made between these. To allow for a vectorial

treatment, highly suitable in the numerical implementation, it is beneficial to define a vector, $\boldsymbol{E}(x)$, containing the guided and sampled radiation modes, and a coefficient vector, $\boldsymbol{c}^{\uparrow}(z)$, whose elements contain constants such that the dotproduct between $\boldsymbol{c}^{\uparrow}(0)$ and $\boldsymbol{E}(x)$ equals $E^{\uparrow}(x,0)$:

$$\boldsymbol{E}(x) = \begin{bmatrix} U_1(x) \\ \vdots \\ U_{N_\mathrm{g}}(x) \\ \psi_1(x,\rho_1) \\ \psi_2(x,\rho_1) \\ \vdots \\ \psi_1(x,\rho_{N_\mathrm{r}}) \\ \psi_2(x,\rho_{N_\mathrm{r}}) \end{bmatrix}, \qquad \boldsymbol{c}^{\uparrow}(0) = \begin{bmatrix} \mathcal{A}^{\mathrm{g}}_1 \\ \vdots \\ \mathcal{A}^{\mathrm{g}}_{N_\mathrm{g}} \\ \mathcal{A}^{\mathrm{r}}(\rho_1)\Delta\rho_1, \\ \mathcal{A}^{\mathrm{r}}(\rho_1)\Delta\rho_1, \\ \vdots \\ \mathcal{A}^{\mathrm{r}}(\rho_{N_\mathrm{r}})\Delta\rho_{N_\mathrm{r}} \\ \mathcal{A}^{\mathrm{r}}(\rho_{N_\mathrm{r}})\Delta\rho_{N_\mathrm{r}} \end{bmatrix}. \tag{5.20}$$

This vectorial representation allows treatment of the effects of propagation and reflection to be conducted entirely in terms of the coefficient vector.

Focusing initially on the reduced system of the two upper layers (Fig. 5.5), the upwards emitted field will eventually reflect at the interface between the waveguide layer and the uniform layer. Propagation of the modes along z can be handled by a propagation matrix, $\mathbf{P}$, that is, a diagonal matrix with elements $\exp(-i\beta L_z/2)$ where β denotes the z-propagation constant appertaining to the relevant mode and $L_z/2$ the distance traveled from the dipole to the interface. Consequently, the coefficient vector at the interface before reflection, $\boldsymbol{c}^{\uparrow}(L_z/2)$, can be expressed as $\boldsymbol{c}^{\uparrow}(L_z/2) = \mathbf{P}\boldsymbol{c}^{\uparrow}(0)$. The reflected and downward propagating field directly after the interface is given by the following coefficient vector:

$$\boldsymbol{c}^{\downarrow}(L_z/2) = \mathbf{R}_{2,3}\boldsymbol{c}^{\uparrow}(L_z/2), \tag{5.21}$$

where $\mathbf{R}_{2,3}$ is a matrix that describes reflection at the interface between layers 2 and 3, similar to the reflection matrices introduced in the closed geometry approach.

In the following, to simplify matters and in accordance with the analysis in the previous section, a single guided mode is assumed. Applying the same discretization as earlier, an arbitrary mode is expected to couple to M modes at the interface, that is, to itself and the $M-1$ other modes. Specifically, the guided mode, $U_1(x)$, is expected to reflect back into itself, but also into the $2N_\mathrm{r}$ sampled radiation modes, described by the coefficients R_1 and $R(\rho_n)$, respectively. Similarly, a sampled radiation mode, $\psi_{\hat{m}}(x,\rho_j)$, is expected to couple to the guided mode and the radiation modes through the coefficients $\mathcal{R}_{\hat{m}}(\rho_n)$ and $\mathcal{R}_{m,\hat{m}}(\rho_n,\rho_j)$, respectively. Further, due to the discretization of the integral, a factor $\Delta\rho_n$ must be included in the matrix treatment of the radiation mode integrals. Following this discussion, the composition of the reflection matrix can be outlined as:

$$\mathbf{R}_{2,3} = \begin{array}{c} \\ 1 \\ N_\mathrm{g} \\ M \end{array} \begin{array}{c} \begin{array}{cc} 1 & N_\mathrm{g} \qquad\qquad M \end{array} \\ \left[\begin{array}{c|c} \text{Guided to guided} & \text{Radiation to guided} \\ \hline \text{Guided to radiation} & \text{Radiation to radiation} \end{array}\right] \end{array}. \tag{5.22}$$

Explicit expressions for the elements in the above matrix in terms of the reflection coefficients R_1, $R(\rho_n)$, $\mathcal{R}_{\hat{m}}(\rho_n)$ and $\mathcal{R}_{m,\hat{m}}(\rho_n, \rho_j)$ are extensive and are therefore omitted, due to the conspectus-approach of this section. However, it is stressed that special care must be taken concerning all diagonal elements of the lower right quadrant since these contain coefficients with Dirac delta functions with zero-arguments. The integral discretization width, $\Delta\rho_n$, should not be multiplied to these terms due to the property of the Dirac delta function (Eq. (4.16)). Finally, the reflection matrix $\mathbf{R}_{2,1}$ is identical to the reflection matrix $\mathbf{R}_{2,3}$ due to the symmetry of the setup.

Having discretized the otherwise continuous field and outlined a procedure for obtaining a reflection matrix, the matter of determining the intra-waveguide field can be carried out in a similar manner to that in the closed geometry (Appendix C.7). Having obtained this field, computation of the emitted power by use of Eq. (3.34), and through that the normalized SER, is possible.

Having outlined a method for obtaining the normalized SER, it is relevant to compare the present theoretical procedure to that used in the closed geometry. Once again, a discretization is necessary to handle the different contributions, a situation highly akin to the closed geometry, and in this context it is natural to question if the treatment of the mathematically more advanced open geometry has been useful. However, a defining and decisive difference between the closed and open geometry approaches is the freedom of choice concerning the sampling of the radiation modes in the open geometry. The θ-discretization, introduced in Section 4.6, or a similar discretization could, seen in the light of the converging results obtained for the open single-layer geometries, conveniently be applied, with well-founded expectations for rapid convergence.

Finally, looking forward, it is noted that the theory presented in this section can be expanded to include more complex structures with multiple layers by use of the scattering matrix formalism, introduced in Section 3.6. Application of the scattering matrix formalism is only reliant on knowledge of the reflection and transmission matrices at interfaces. Determining the field inside, e.g. a microcavity is then essentially a matter of applying scattering reflection matrices rather than ordinary reflection matrices. Again, high expectations for rapid convergence are reasonable, based on the results obtained with the θ-discretization in Section 4.6.

5.5 Summary

This chapter has presented the theory necessary to describe a two-layered open geometry, namely a geometry modeling an abruptly terminated waveguide with low index contrast and core width, and the results obtained from the theoretical approach. The eigenmodes in the open geometry were presented in the previous chapter, and the present chapter has consequently focused on the effects introduced due to the interface between the two layers.

The interface effects were dependent on the type of incident mode, and firstly an incident guided mode was examined. A Fredholm equation of the second kind for the aperture field was presented, and definitions of reflection and transmission coefficients, essentially given as the projections of the aperture field onto the eigenmodes of each layer, were presented. Following this, a procedure for obtaining approximate solutions was discussed, involving the application of a truncated Liouville-Neumann series. Application of the truncated Liouville-Neumann series to the first order yielded approximate expressions for the aperture field and from this approximate expressions for the reflection and transmission coefficients. Next, results for these first order reflection and transmission

coefficients were presented which were in agreement with qualitative expectations. By combining the results from the treatment of an incident guided mode, a first order field profile of an open two-layer geometry was presented. This field profile clearly showcased that issues of parasitic reflections, observed in the closed geometry, are avoided in the open geometry.

Thereafter, treatment of an incident radiation mode was initiated. Similar to the case of an incident guided mode, a Fredholm equation of the second kind was presented, and approximate first order solutions for the aperture field and reflection and transmission coefficients were given. Numerical investigations displayed that these expressions did not converge as expected.

Lastly, a procedure for determination of the normalized SER in multi-layered open geometries was outlined. The procedure essentially relied on a discretization of the continuous radiation mode propagation constants and on the scattering matrix formalism, introduced for the closed geometry.

Chapter 6

Conclusion

The work presented in this bachelor thesis has investigated two methods for modeling and simulating the electric field inside various optical environments in dielectric slab structures. In the first method, the closed geometry approach, the solution domain is given finite dimensions, and the electric field is forced to vanish outside this simulation domain. In the second method, the open geometry approach, the solution domain is given infinite dimensions, and the field is consequently nowhere forced to vanish. The overall aim of the project has been to determine to what extent the mathematically more advanced open geometry approach produces more accurate results than the mathematically simpler closed geometry approach.

Specifically, the two approaches have been compared qualitatively by comparison of the electric field profiles, and quantitatively by computation of the normalized SER due to a dipole current source. Comparison of the results from the two approaches indicates how optical structures may potentially be modeled more accurately with the open geometry approach. The results and findings of this thesis may therefore contribute to the future theoretical simulations of nano-photonic structures.

As discussed in the following paragraphs, it has been demonstrated that the open geometry approach yields more reliable results for the electric field and for the normalized SER. This can mainly be attributed to the treatment of the radiation modes in the open geometry approach.

Using the closed geometry approach, the electric field was required to vanish outside the slab structure which cast the scalar Helmholtz equation and the corresponding BCs on the form of an ordinary and standardized PDE problem. Having determined the discrete eigenmodes of this PDE problem in each layer in the geometry, the electric field was expanded on these eigenmodes throughout the geometry using eigenmode expansion technique and the scattering matrix formalism. This formalism and the corresponding expansion of the electric field can, in principle, be carried out for any arbitrary step-index profile, and the versatility of this tool was applied to plot the field profile in a number of step-index profiles. Even though the tool is limited to step-index profiles, it can nonetheless be used to approximate arbitrary geometries by application of a staircase-approximation.

The field profiles from the closed geometry constituted qualitatively good results, but the assumption of perfectly conducting boundaries, necessary to confine the field to a domain of finite dimensions, introduced parasitic reflections in the field profiles, visible as interference effects. The closed geometry, with its perfectly conducting boundaries, represents a box enclosed by metal, and the field and corresponding parasitic reflections

very well represent this. However, the slab structures of interest are not enclosed by metal, and these parasitic reflections in the simulations are consequently undesirable.

The power emitted from the dipole current source was argued to be an equivalent quantity to the normalized SER, and it was shown that this power was given as the real part of the electric field due to the dipole evaluated at the point of the dipole. Therefore, the presence of parasitic reflections in the closed geometry inescapably affected the SER results.

The overall and unsatisfactory picture of the results was that the normalized SER did not converge as the width of the structure was increased, and the relative fluctuations of the normalized SER in different single- and three-layer closed geometries were in the range from 8% to 26%. The fluctuations decreased slightly as the width of the geometry was increased which could be explained by the aforementioned field profiles: Increasing the width, the relative effect from the parasitic reflections in the point of the dipole current source diminished, and hence a more correct electric field was obtained. However, increasing the width of the geometry necessitates inclusion of additional eigenmodes, and at this price the small decrease in the variations of the SER was unsatisfactory.

In conclusion, the SER from the dipole current source could not be determined satisfactorily accurate using the closed geometry approach, and this therefore motivated the introduction of the open geometry approach.

The treatment of the open geometry approach was split into two chapters. The first of these, Chapter 4, presented an open single-layer geometry, and the PDE for the electric field to be solved was identical to that in the closed geometry. However, the infinite width of the structure removed the outer BCs that ensured vanishing of the field at the boundaries in the closed geometry. The mathematical treatment of this involved introduction of a new normalization procedure and of more distinct mode types, compared to the closed geometry. Specifically, the infinite width of the structure entailed a clear segregation of the radiation modes and the guided modes, as a finite number of guided modes and a continuum of radiation modes existed, in contrast to the discrete set of eigenmodes in the closed geometry.

Expressions for the SER from a dipole current source in the open single-layer geometry were derived, and due to the continuum of radiation modes these contained integrals over the continuous radiation mode propagation constants. In general, the practical evaluation of these integrals had to be carried out numerically which called for a discretization of the propagation constants. The results for the SER, as function of the degree of discretization, converged uniformly, contrary to the corresponding results in the closed geometry. Using a non-equidistant discretization, uniform convergence and relative errors of less than 1% was attained with 24 and 7 sampling points for a uniform and a waveguide layer, respectively. These results therefore gave a first and important contribution to the assessment of the open geometry approach compared to the closed geometry approach: The SER due to the dipole may be determined accurately using the open geometry approach.

Finally, Chapter 5 presented the formalism for analyzing a two-layered open geometry consisting of a waveguide layer and a uniform layer. The further treatment of this open geometry was split into two cases, namely those of illumination by a guided mode and illumination by a radiation mode. In both situations, the fields on either side of the interface between the layers were defined, expressed in terms of eigenmodes and reflection and transmission coefficients. Applying the demand for continuity and differentiability of the field at the interface and the orthonormality and completeness relations for the guided and radiation modes further led to expressions for the reflection and transmission

coefficients and Fredholm integral equations of the second kind in the aperture fields.

Despite the integral equations being of the same type in both of the aforementioned cases, the numerical results were only as expected for the case of illumination by a guided mode: The reflection and transmission coefficients subsided as functions of the respective propagation constants, as expected, and the field profile did not suffer from the parasitic reflections observed in the closed geometry. The same formalism was derived for illumination by a radiation mode, but the numerical results were not as expected: The aperture field was undefined, and the reflection and transmission coefficients did not converge to zero for increasing values of the propagation constants. Consequently, no meaningful field profile could be produced.

Lastly, an outline for the calculation of the normalized SER in an open three-layered geometry was presented, and if the numerical problems for the illumination by a radiation mode are resolved, the computation of the normalized SER in this structure is straightforward.

In conclusion, the outcome of this thesis is a formalism that allows a precise determination of the normalized SER using the open geometry approach. Furthermore, it has been documented that the open geometry approach represents a considerable improvement in the modeling of slab structures.

Appendix **A**

Nomenclature and Acronyms

This chapter contains an overview of nomenclature and acronyms, starting with an overview of nomenclature.

A.1 Nomenclature

The four tables below list the used symbols, and each table display the symbols introduced in either of the four chapters. Finally, each table is arranged alphabetically with respect to the first column. Symbols used in several chapters are not reintroduced if they are already contained in a previous table.

Chapter 2

Meaning	Symbol
Angular frequency	ω
Cartesian x-component of electric field	E_x
Cartesian x-component of magnetic field	H_x
Electric displacement field	$\mathbf{D}$
Electric field	$\mathbf{E}$
Electric susceptibility	χ_e
Free charge density	ρ_f
Free current density	$\mathbf{J}_f$
Free space propagation constant	k_0
Magnetic $\mathbf{H}$-field	$\mathbf{H}$
Magnetic field	$\mathbf{B}$
Permeability	μ
Permittivity	ϵ
Refractive index	n
Relative permittivity	ϵ_r
Vacuum permeability	μ_0
Vacuum permittivity	ϵ_0
x-dependent eigenmodes	e_x, $e_{x,j}$
x-propagation constant	κ, κ_j
z-dependent eigenmodes	e_z, $e_{z,j}$
z-propagation constant	β, β_j

Chapter 3

Meaning	Symbol
Current density due to current source	$\mathbf{J}$
Effective reflection and propagation matrices	$\mathbf{R}_{\text{bot}}$, $\mathbf{R}_{\text{top}}$
Electric field along positive and negative z direction	$E_{\uparrow}$, $E_{\downarrow}$
Set of imaginary numbers	$\mathbb{I}$
Layer number (along z)	$\{q\}$
Modal amplitudes	$\mathcal{A}_j$, $\mathcal{B}_j$
Mode contribution vectors to electric field	$\boldsymbol{\epsilon}^{\uparrow}$, $\boldsymbol{\epsilon}^{\downarrow}$
Non-normalized x-eigenmode	$\check{\boldsymbol{e}}_j$
Normalization constant with Power inner product	$\mathcal{N}_j$
Normalized x-eigenmode	$\boldsymbol{e}_j$
Normalized spontaneous emission rate	α
Number of zones in some layer	P
Power emitted from current source in bulk material	P_0
Power emitted from current source in bulk material	P
Power inner product	$\langle\cdot,\cdot\rangle_{\text{P}}$, $\mathcal{N}'_j$
Power ratio deviation	$\delta\alpha$
Reflection matrix from layer q to $q+1$	$\mathbf{R}_{q,q+1}$
Repetition length for power ratio (closed geometry)	δL_x
Scattering reflection matrix from layer q to r	$\mathbf{SR}_{q,r}$
Scattering transmission matrix from layer q to r	$\mathbf{ST}_{q,r}$
Spontaneous emission rate	γ
Spontaneous emission rate in bulk material	γ_0
Transmission matrix from layer q to $q+1$	$\mathbf{T}_{q,q+1}$
Width of waveguide	D_g
x-coordinate of interface between the p and $p+1$th zone	$L_{p,p+1}$
x-width of closed geometry	L_x
z-coordinate of interface between the q and $q+1$th layer	$z_{q,q+1}$
Zone number (along x)	$[p]$

Chapter 4

Meaning	Symbol
Angular mode spacing	θ
Integrand in power expression from radiation modes	Γ_m
$L^2(\mathbb{R})$ inner product	$\langle \cdot, \cdot \rangle_{L^2}$
Modal amplitudes	$\mathcal{A}_l(s)$, $\mathcal{B}_m(\rho)$
Mode discretization step	Δs
Normalization constant with $L^2(\mathbb{R})$ inner product	$\mathcal{N}_{L^2}$
Number of subintervals in numerical integration	$\#$
Power contribution from guided modes	P_{g}
Power contribution from radiation modes	P_{r}
Repetition length	L_{rep}
Scattering contribution to radiation mode (non-normalized)	$\check{\xi}_m$
Uniform layer radiation mode (non-normalized)	$\check{\phi}_l$
Uniform layer radiation mode (normalized)	ϕ_l
Uniform layer x-propagation constant	s
Uniform layer z-propagation constant	γ
Waveguide layer guided mode (non-normalized)	$\check{U}_j$
Waveguide layer guided mode (normalized)	U_j
Waveguide layer guided mode x-propagation constant	$h_j^{[1,3]}$, $h_j^{[2]}$
Waveguide layer guided mode z-propagation constant	β_j
Waveguide layer radiation mode (non-normalized)	$\check{\psi}_m$
Waveguide layer radiation mode (normalized)	ψ_m
Waveguide layer radiation mode x-propagation constant	ρ, ρ_{co}
Waveguide layer radiation mode z-propagation constant	β

Chapter 5

Meaning	Symbol
Aperture field due to incident radiation mode	$\Theta_{\hat{m}}(x, \hat{\rho})$
Aperture field due to incident guided mode	$\Phi(x)$
Coefficient vector	$\boldsymbol{c}^{\uparrow}(z)$, $\boldsymbol{c}^{\downarrow}(z)$
Dirac delta prefactor in $\langle \psi_m(\rho), \phi_l(s) \rangle_{L^2}$	$G_{m,l}(\rho)$
Effective reflection matrices for guided and radiation modes	$\mathbf{R}_{2,3}$, $\mathbf{R}_{2,1}$
Electric field in layer 1 due to incident guided mode	$E_1(x, z)$
Electric field in layer 1 due to incident radiation mode	$\mathcal{E}_1(x, z)$
Electric field in layer 2 due to incident guided mode	$E_2(x, z)$
Electric field in layer 2 due to incident radiation mode	$\mathcal{E}_2(x, z)$
First order aperture field due to incident guided mode	$\Phi_1(x)$
First order aperture field due to incident radiation mode	$\Theta_{1,\hat{m}}(x, \hat{\rho})$
First order coefficients with superscript	$^{(1)}$
Guided and sampled radiation mode vector	$\boldsymbol{E}(x)$
Incident radiation mode	$\psi_{\hat{m}}(x, \hat{\rho})$
Index contrast	Δn
Integral prefactor in Fredholm equations of the second kind	λ
Integrand for aperture field $\Theta_{1,\hat{m}}$, see Eq. (5.16)	$J_l(s)$
jth term in the Liouville-Neumann series solution	$C_j(x)$
Kernel in Fredholm equation, see Eq. (5.3d)	$K(x, x')$
Kernel in Fredholm equation, see Eq. (5.11c)	$\mathcal{K}(x, x')$
Non-Dirac delta terms in $\langle \psi_m(\rho), \phi_l(s) \rangle_{L^2}$	$H_{m,l}(\rho, s)$
Non-Dirac delta terms in $\mathcal{R}_{m,\hat{m}}(\rho, \hat{\rho})$, see Eq. (5.17)	$W_l(\rho)$
Number of constituting modes in discrete treatment	M
Number of guided modes	N_{g}
Number of sampled radiation modes	N_{r}
Reflection from guided mode to guided mode	R_1
Reflection from guided mode to waveguide radiation modes	$R(\rho)$
Reflection from radiation mode to guided mode	$\mathcal{R}_{1,\hat{m}}(\hat{\rho})$
Reflection from radiation mode to waveguide radiation modes	$\mathcal{R}_{m,\hat{m}}(\rho, \hat{\rho})$
Refractive index in uniform layer	n_0
Refractive index of cladding region	n_1
Refractive index of core region	n_2
Sampling distance between radiation modes	$\Delta\rho_n$
Transmission from guided mode to uniform layer radiation modes	$T(s)$
Transmission from radiation mode to uniform layer radiation modes	$\mathcal{T}_{l,\hat{m}}(s, \hat{\rho})$
Zeroth order aperture field due to incident guided mode	$\Phi_0(x)$
Zeroth order aperture field due to incident radiation mode	$\Theta_{0,\hat{m}}(x, \hat{\rho})$
z-length of waveguide region in three-layer SER treatment	L_z

A.2 Acronyms

The acronyms used in this report are stated below, arranged alphabetically, and apply to all chapters.

Meaning	**Acronym**
Electromagnetic wave	EW
Transverse electric	TE
Transverse magnetic	TM
Transerve electromagnetic	TEM
Sturm-Liouville	SL
Partial differential equation	PDE
Ordinary differential equation	ODE
Spontaneous emission rate	SER

Appendix **B**

Chapter 2

B.1 Product Solution for Helmholtz Equation

In this section, it is verified that the product solution defined in Eqs. (2.11) and (2.14) fulfills the scalar Helmholtz equation in Eq. (2.10). Firstly, the product solution is written out explicitly for an arbitrary j:

$$E_y(x,z) = e_{x,j}(x)e_{z,j}(z) = \left(a_j \mathrm{e}^{i\kappa_j x} + b_j \mathrm{e}^{-i\kappa_j x}\right)\left(c_{1,j}\mathrm{e}^{i\beta_j z} + c_{2,j}\mathrm{e}^{-i\beta_j z}\right). \tag{B.1}$$

This expression is inserted into the left hand side of Eq. (2.10):

$$\begin{aligned}
\nabla^2 E_y + n^2 k_0^2 E_y &= \frac{\mathrm{d}^2 E_y}{\mathrm{d}x^2} + \frac{\mathrm{d}^2 E_y}{\mathrm{d}z^2} + n^2 k_0^2 E_y \\
&= \left[-\left(\kappa_j^2 + \beta_j^2\right)\left(a_j \mathrm{e}^{i\kappa_j x} + b_j \mathrm{e}^{-i\kappa_j x}\right)\left(c_{1,j}\mathrm{e}^{i\beta_j z} + c_{2,j}\mathrm{e}^{-i\beta_j z}\right)\right] \\
&\quad + \left[n^2 k_0^2 \left(a_j \mathrm{e}^{i\kappa_j x} + b_j \mathrm{e}^{-i\kappa_j x}\right)\left(c_{1,j}\mathrm{e}^{i\beta_j z} + c_{2,j}\mathrm{e}^{-i\beta_j z}\right)\right] \\
&= \left[-\left(\kappa_j^2 + \beta_j^2\right) + n^2 k_0^2\right]\left[\left(a_j \mathrm{e}^{i\kappa_j x} + b_j \mathrm{e}^{-i\kappa_j x}\right)\left(c_{1,j}\mathrm{e}^{i\beta_j z} + c_{2,j}\mathrm{e}^{-i\beta_j z}\right)\right] \\
&= 0,
\end{aligned} \tag{B.2}$$

where the last equal sign follows from the definition of κ_j in Eq. (2.13a). Hence, the product solution satisfies the scalar Helmholtz equation.

Appendix C

Chapter 3

C.1 Boundary Condition Matrix

This appendix introduces the boundary condition matrix necessary to determine the eigenmodes in an arbitrary zone-configuration. The boundary condition matrix along with the definition of the eigenmode-form, to be introduced shortly, uniquely determines the allowed modes in a layer.

The structure of the zone-solutions, $e^{[p]}_{x,j}(x)$, and the BCs can be exploited to obtain a matrix that allows determination of the allowed eigenmodes. Referring to Eq. (2.14a), the structure of $e^{[p]}_{x,j}(x)$ is:

$$e^{[p]}_{x,j}(x) = \tilde{a}^{[p]}_j \exp(i\kappa^{[p]}_j x) + \tilde{b}^{[p]}_j \exp(-i\kappa^{[p]}_j x), \tag{C.1}$$

where $\tilde{a}^{[p]}_j$ and $\tilde{b}^{[p]}_j$ are the complex coefficients determining the amplitudes of the forward and backward propagating parts of the eigenmode, respectively. An eigenmode, $e_{x,j}(x)$, is then given as the piecewise function of the zone-solutions in Eq. (C.1).

In the case of $\kappa^{[p]}_j \in \mathbb{I}$ (set of imaginary numbers), the otherwise harmonic waves become exponentially in- or decreasing functions. Since the values of $e^{[p]}_{x,j}(x)$ must be reasonable in the interval $L_{p-1,p} \leq x \leq L_{p,p+1}$ to ensure numerical stability, the coefficients $\tilde{a}^{[p]}_j$ and $\tilde{b}^{[p]}_j$ risk assuming either very small or very large numerical values. The problem is circumvented by defining the exponential functions relative to the appropriate zone boundaries:

$$e^{[p]}_{x,j}(x) = a^{[p]}_j \exp(i\kappa^{[p]}_j (x - L_{p-1,p})) + b^{[p]}_j \exp(-i\kappa^{[p]}_j (x - L_{p,p+1})) \tag{C.2}$$

where $L_{0,1} \equiv 0$ and $L_{P,P+1} \equiv L_x$, and where $a^{[p]}_j$ and $b^{[p]}_j$ are new coefficients.

Combining the inner and outer BCs from Eqs. (3.1) and (3.2) with the zone-solutions

in Eq. (C.2), the following $2P$ equations for each j are obtained:

$$a_j^{[1]} + b_j^{[1]} \mathrm{e}^{i\kappa_j^{[1]} L_{1,2}} = 0, \tag{C.3a}$$

$$\vdots$$

$$a_j^{[p]} \mathrm{e}^{i\kappa_j^{[p]}(L_{p,p+1}-L_{p-1,p})} + b_j^{[p]} = a_j^{[p+1]} + b_j^{[p+1]} \mathrm{e}^{-i\kappa_j^{[p+1]}(L_{p,p+1}-L_{p+1,p+2})}, \tag{C.3b}$$

$$a_j^{[p]}\kappa_j^{[p]} \mathrm{e}^{i\kappa_j^{[p]}(L_{p,p+1}-L_{p-1,p})} - b_j^{[p]}\kappa_j^{[p]} = a_j^{[p+1]}\kappa_j^{[p+1]} - b_j^{[p+1]}\kappa_j^{[p+1]} \mathrm{e}^{-i\kappa_j^{[p+1]}(L_{p,p+1}-L_{p+1,p+2})}, \tag{C.3c}$$

$$\vdots$$

$$a_j^{[P]} \mathrm{e}^{i\kappa_j^{[P]}(L_x - L_{P-1,P})} + b_j^{[P]} = 0, \tag{C.3d}$$

where $p = 1, 2, \ldots, P-1$. Eqs. (C.3) form a homogeneous system of linear equations in $a_j^{[1]}, b_j^{[1]}, a_j^{[2]}, b_j^{[2]}, \ldots, a_j^{[P]}, b_j^{[P]}$, that can be written as a matrix equation:

$$\mathbf{A}_j \boldsymbol{c}_j = \mathbf{0}, \tag{C.4}$$

where $\boldsymbol{c}_j$ contains the coefficients:

$$\boldsymbol{c}_j = \begin{bmatrix} a_j^{[1]}, & b_j^{[1]}, & a_j^{[2]}, & b_j^{[2]}, & \ldots, & a_j^{[P]}, & b_j^{[P]} \end{bmatrix}^T. \tag{C.5}$$

The boundary condition matrix, $\mathbf{A}_j$, is:

$$\begin{bmatrix}
1 & \mathrm{e}^{i\kappa_j^{[1]} L_{1,2}} & & & & \\
\mathrm{e}^{i\kappa_j^{[1]} L_{1,2}} & 1 & -1 & -\mathrm{e}^{-i\kappa_j^{[2]}(L_{1,2}-L_{2,3})} & & \\
\kappa_j^{[1]} \mathrm{e}^{i\kappa_j^{[1]} L_{1,2}} & -\kappa_j^{[1]} & -\kappa_j^{[2]} & \kappa_j^{[2]} \mathrm{e}^{-i\kappa_j^{[2]}(L_{1,2}-L_{2,3})} & & \\
\ddots & \ddots & \ddots & \ddots & & \\
 & \mathrm{e}^{i\kappa_j^{[P-1]}(L_{P-1,P}-L_{P-2,P-1})} & 1 & -1 & -\mathrm{e}^{-i\kappa_j^{[P]}(L_{P-1,P}-L_x)} \\
 & \kappa_j^{[P-1]} \mathrm{e}^{i\kappa_j^{[P-1]}(L_{P-1,P}-L_{P-2,P-1})} & -\kappa_j^{[P-1]} & -\kappa_j^{[P]} & \kappa_j^{[P]} \mathrm{e}^{-i\kappa_j^{[P]}(L_{P-1,P}-L_x)} \\
 & & & \mathrm{e}^{i\kappa_j^{[P]}(L_x - L_{P-1,P})} & 1
\end{bmatrix}. \tag{C.6}$$

The square matrix $\mathbf{A}_j$ contains the factors to the coefficients in Eqs. (C.3) and hence all the available information about the jth eigenmode and the BCs. The matrix is of central importance in the determination of eigenmodes, as discussed in Section 3.2.

C.2 Normalization with Power Inner Product

In this section, the power inner product, defined in Eq. (3.5), is expressed explicitly in terms of the electric x-eigenmodes. First, the vectorial electric and magnetic eigenmodes, $\boldsymbol{e}_j$ and $\boldsymbol{h}_j$, are defined: The (x, y, z)-components of the vectors contain the electric and magnetic polarization contributions in the (x, y, z)-direction, respectively. Consequently, since the electric field is assumed to be polarized along y, the $\boldsymbol{e}_j(x)$ vector can be written as:

$$\boldsymbol{e}_j(x) \equiv \begin{bmatrix} (\boldsymbol{e}_j(x))_x \\ (\boldsymbol{e}_j(x))_y \\ (\boldsymbol{e}_j(x))_z \end{bmatrix} = \begin{bmatrix} 0 \\ e_{x,j}(x) \\ 0 \end{bmatrix}, \tag{C.7}$$

where $e_{x,j}(x)$ are the eigenmodes determined in Section 3.2. The integrand in the Power inner product can now be written out explicitly:

$$\begin{aligned}(\boldsymbol{e}_j(x) \times \boldsymbol{h}_i^*(x)) \cdot \hat{\boldsymbol{z}} &= (\boldsymbol{e}_j(x) \times \boldsymbol{h}_i^*(x))_z \\ &= (\boldsymbol{e}_j(x))_x (\boldsymbol{h}_i^*(x))_y - (\boldsymbol{e}_j(x))_y (\boldsymbol{h}_i^*(x))_x \\ &= -(\boldsymbol{e}_j(x))_y (\boldsymbol{h}_i^*(x))_x. \end{aligned} \tag{C.8}$$

From Eq. (2.9), the x-component of the **H**-field is related to the y-component of the **E**-field through:

$$H_{x,i} = -\frac{1}{i\omega\mu_0} \frac{\partial E_{y,i}}{\partial z}. \tag{C.9}$$

Assuming in the following that $E_{y,i}$ consists only of a forward propagating part along z, this gives:

$$H_{x,i} = -\frac{1}{i\omega\mu_0} \frac{\partial}{\partial z} (e_{x,i}(x) \exp(i\beta_i z)) = -\frac{\beta_i}{\omega\mu_0} e_{x,i}(x) \exp(i\beta_i z). \tag{C.10}$$

Defining $H_{x,i} \equiv (\boldsymbol{h}_i(x))_x \exp(i\beta_i z)$ then produces:

$$(\boldsymbol{h}_i(x))_x = -\frac{\beta_i}{\omega\mu_0} e_{x,i}(x). \tag{C.11}$$

The same result is obtained for a backward propagating $E_{y,i}$, if $\hat{\boldsymbol{z}}$ in Eq. (C.8) is exchanged with $-\hat{\boldsymbol{z}}$ due to the reversed propagation direction. Insertion into the expression in Eq. (C.8) and integration over x then gives:

$$\begin{aligned}\langle \boldsymbol{e}_j, \boldsymbol{e}_i \rangle_{\mathrm{P}} &= \frac{1}{2} \int_0^{L_x} e_{x,j}(x) \left(\frac{\beta_i}{\omega\mu_0} e_{x,i}(x) \right)^* \mathrm{d}x \\ &= \frac{\beta_i^*}{2\omega\mu_0} \int_0^{L_x} e_{x,j}(x) e_{x,i}(x)^* \mathrm{d}x. \end{aligned} \tag{C.12}$$

C.3 Three-Layer Structure: Scattering Matrices

In this section, the scattering matrices $\mathbf{SR}_{1,3}$ and $\mathbf{ST}_{1,3}$ for a three-layer structure, introduced in Section 3.6, are derived. The derivations rely heavily on the illustration in Fig. 3.9(b) since each term in the following expressions can be traced directly by tracing the back- and forward-propagating fields in the second layer.

The scattering reflection matrix $\mathbf{SR}_{1,3}$ can be expressed by adding the different contributions to the reflection at the first interface, namely the initial reflection due to $\mathbf{R}_{1,2}$ and the contributions due to transmission of the backwards propagating circulating field in the second layer:

$$\begin{aligned}\mathbf{SR}_{1,3} = &\mathbf{R}_{1,2} + \underbrace{\mathbf{T}_{2,1}\mathbf{P}_2\mathbf{R}_{2,3}\mathbf{P}_2\mathbf{T}_{1,2}}_{\substack{\text{First contribution from} \\ \text{circulating field}}} + \underbrace{(\mathbf{T}_{2,1}\mathbf{P}_2\mathbf{R}_{2,3}\mathbf{P}_2)\mathbf{R}_{2,1}\mathbf{P}_2\mathbf{R}_{2,3}\mathbf{P}_2\mathbf{T}_{1,2}}_{\text{Second contribution from circulating field}} \\ &+ \underbrace{(\mathbf{T}_{2,1}\mathbf{P}_2\mathbf{R}_{2,3}\mathbf{P}_2)(\mathbf{R}_{2,1}\mathbf{P}_2\mathbf{R}_{2,3}\mathbf{P}_2)\mathbf{R}_{2,1}\mathbf{P}_2\mathbf{R}_{2,3}\mathbf{P}_2\mathbf{T}_{1,2}}_{\text{Third contribution from circulating field}} + \ldots. \end{aligned} \tag{C.13}$$

Rewriting this expression slightly reveals a geometric matrix-series of the form $\sum_{j=0}^{\infty}\mathbf{M}^j$, with the sum $(\mathbf{I}-\mathbf{M})^{-1}$:

$$\begin{aligned}\mathbf{SR}_{1,3} &= \mathbf{R}_{1,2} + \mathbf{T}_{2,1}\mathbf{P}_2\mathbf{R}_{2,3}\mathbf{P}_2\Big\{\mathbf{I} + \mathbf{R}_{2,1}\mathbf{P}_2\mathbf{R}_{2,3}\mathbf{P}_2 \\ &\quad + \mathbf{R}_{2,1}\mathbf{P}_2\mathbf{R}_{2,3}\mathbf{P}_2\mathbf{R}_{2,1}\mathbf{P}_2\mathbf{R}_{2,3}\mathbf{P}_2 + \dots\Big\}\mathbf{T}_{1,2} \\ &= \mathbf{R}_{1,2} + \mathbf{T}_{2,1}\mathbf{P}_2\mathbf{R}_{2,3}\mathbf{P}_2\left[\sum_{j=0}^{\infty}(\mathbf{R}_{2,1}\mathbf{P}_2\mathbf{R}_{2,3}\mathbf{P}_2)^j\right]\mathbf{T}_{1,2} \\ &= \mathbf{R}_{1,2} + \mathbf{T}_{2,1}\mathbf{P}_2\mathbf{R}_{2,3}\mathbf{P}_2\big(\mathbf{I}-\mathbf{R}_{2,1}\mathbf{P}_2\mathbf{R}_{2,3}\mathbf{P}_2\big)^{-1}\mathbf{T}_{1,2}. \end{aligned} \tag{C.14}$$

A similar procedure can be used for the scattering transmission matrix $\mathbf{ST}_{1,3}$, by considering the transmission contributions due to both direct transmission through the first and second layer and due to transmission of the forward circulating field in the second layer:

$$\begin{aligned}\mathbf{ST}_{1,3} &= \mathbf{T}_{2,3}\mathbf{P}_2\left[\sum_{j=0}^{\infty}(\mathbf{R}_{2,1}\mathbf{P}_2\mathbf{R}_{2,3}\mathbf{P}_2)^j\right]\mathbf{T}_{1,2} \\ &= \mathbf{T}_{2,3}\mathbf{P}_2\big(\mathbf{I}-\mathbf{R}_{2,1}\mathbf{P}_2\mathbf{R}_{2,3}\mathbf{P}_2\big)^{-1}\mathbf{T}_{1,2}. \end{aligned} \tag{C.15}$$

The derivations of the matrices $\mathbf{SR}_{3,1}$ and $\mathbf{ST}_{3,1}$ follow the same pattern, and the results are stated below:

$$\mathbf{SR}_{3,1} = \mathbf{R}_{3,2} + \mathbf{T}_{2,3}\mathbf{P}_2\mathbf{R}_{2,1}\mathbf{P}_2\big(\mathbf{I}-\mathbf{R}_{2,3}\mathbf{P}_2\mathbf{R}_{2,1}\mathbf{P}_2\big)^{-1}\mathbf{T}_{3,2} \tag{C.16a}$$

$$\mathbf{ST}_{3,1} = \mathbf{T}_{2,1}\mathbf{P}_2\big(\mathbf{I}-\mathbf{R}_{2,3}\mathbf{P}_2\mathbf{R}_{2,1}\mathbf{P}_2\big)^{-1}\mathbf{T}_{3,2} \tag{C.16b}$$

C.4 Three-Layer Structure: Coefficients in Second Layer

In this section, the coefficient vectors in the second layer, introduced in Section 3.6, $\boldsymbol{A}^{\{2\}}$ and $\boldsymbol{B}^{\{2\}}$, in a general three layer structure are derived. $\boldsymbol{A}^{\{2\}}$ contains the field coefficients for the forward propagating part of the field at the first interface ($z_{1,2}$), while $\boldsymbol{B}^{\{2\}}$ contains the field coefficients for the backward propagating part of the field at the second interface ($z_{2,3}$).

The vectors can be determined in a manner similar to that in the derivation of the scattering matrices (Appendix C.3), that is, by accounting for the multiple circulations of the field, and the results are:

$$\begin{aligned}\boldsymbol{A}^{\{2\}} &= \sum_{j=0}^{\infty}\left(\mathbf{R}_{2,1}\mathbf{P}_2\mathbf{R}_{2,3}\mathbf{P}_2\right)^j\mathbf{T}_{1,2}\tilde{\boldsymbol{A}}^{\{1\}} + \sum_{j=0}^{\infty}\left(\mathbf{R}_{2,1}\mathbf{P}_2\mathbf{R}_{2,3}\mathbf{P}_2\right)^j\mathbf{R}_{2,1}\mathbf{P}_2\mathbf{T}_{3,2}\tilde{\boldsymbol{B}}^{\{3\}} \\ &= \sum_{j=0}^{\infty}\left(\mathbf{R}_{2,1}\mathbf{P}_2\mathbf{R}_{2,3}\mathbf{P}_2\right)^j\left(\mathbf{T}_{1,2}\tilde{\boldsymbol{A}}^{\{1\}} + \mathbf{R}_{2,1}\mathbf{P}_2\mathbf{T}_{3,2}\tilde{\boldsymbol{B}}^{\{3\}}\right) \\ &= \left(\mathbf{I}-\mathbf{R}_{2,1}\mathbf{P}_2\mathbf{R}_{2,3}\mathbf{P}_2\right)^{-1}\left(\mathbf{T}_{1,2}\tilde{\boldsymbol{A}}^{\{1\}} + \mathbf{R}_{2,1}\mathbf{P}_2\mathbf{T}_{3,2}\tilde{\boldsymbol{B}}^{\{3\}}\right), \end{aligned} \tag{C.17a}$$

$$\begin{aligned}\boldsymbol{B}^{\{2\}} &= \sum_{j=0}^{\infty} \left(\mathbf{R}_{2,3}\mathbf{P}_2\mathbf{R}_{2,1}\mathbf{P}_2\right)^j \mathbf{R}_{2,3}\mathbf{P}_2\mathbf{T}_{1,2}\tilde{\boldsymbol{A}}^{\{1\}} + \sum_{j=0}^{\infty} \left(\mathbf{R}_{2,3}\mathbf{P}_2\mathbf{R}_{2,1}\mathbf{P}_2\right)^j \mathbf{T}_{3,2}\tilde{\boldsymbol{B}}^{\{3\}} \\ &= \sum_{j=0}^{\infty} \left(\mathbf{R}_{2,3}\mathbf{P}_2\mathbf{R}_{2,1}\mathbf{P}_2\right)^j \left(\mathbf{R}_{2,3}\mathbf{P}_2\mathbf{T}_{1,2}\tilde{\boldsymbol{A}}_{\mathrm{I}} + \mathbf{T}_{3,2}\tilde{\boldsymbol{B}}^{\{3\}}\right) \\ &= \left(\mathbf{I} - \mathbf{R}_{2,3}\mathbf{P}_2\mathbf{R}_{2,1}\mathbf{P}_2\right)^{-1} \left(\mathbf{R}_{2,3}\mathbf{P}_2\mathbf{T}_{1,2}\tilde{\boldsymbol{A}}^{\{1\}} + \mathbf{T}_{3,2}\tilde{\boldsymbol{B}}^{\{3\}}\right). \end{aligned} \tag{C.17b}$$

C.5 Multi-Layer Structure: Inner Field Coefficients

This appendix derives the expansion coefficient vectors for the qth layer, $\boldsymbol{A}^{\{q\}}$ and $\boldsymbol{B}^{\{q\}}$, in a structure of Q layers as introduced in the subsection about the multi-layer structure in Section 3.6.

Assuming knowledge of the scattering matrices $\mathbf{SR}_{q,1}$, $\mathbf{SR}_{q,Q}$, $\mathbf{ST}_{1,q}$ and $\mathbf{ST}_{Q,q}$, the field coefficients in the qth layer are desired. Observing Fig. C.1, it is seen that the problem of obtaining these coefficients largely corresponds to the problem of obtaining the inner coefficients in a three layer structure. The difference is that the transmission and reflection matrices that govern the inner field coefficients in the case of a three layer structure are replaced by scattering transmission and reflection matrices.

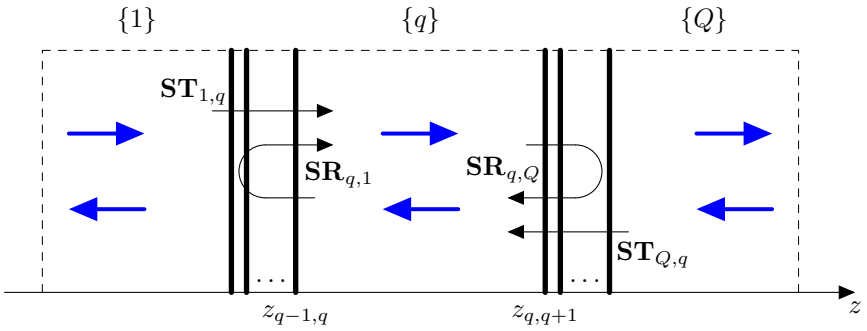

Figure C.1 Illustration of the relevant scattering transmission and reflection matrices, necessary to describe the field coefficients in the qth layer.

Using therefore the expression in Eqs. (C.17), and substituting $\mathbf{R}_{j,k} \curvearrowright \mathbf{SR}_{j,k}$, $\mathbf{T}_{j,k} \curvearrowright \mathbf{ST}_{j,k}$, $2 \curvearrowright q$, and $3 \curvearrowright Q$, the following expressions are obtained:

$$\boldsymbol{A}^{\{q\}} = \left(\mathbf{I} - \mathbf{SR}_{q,1}\mathbf{P}_q\mathbf{SR}_{q,Q}\mathbf{P}_q\right)^{-1} \left(\mathbf{ST}_{1,q}\tilde{\boldsymbol{A}}^{\{1\}} + \mathbf{SR}_{q,1}\mathbf{P}_q\mathbf{ST}_{Q,q}\tilde{\boldsymbol{B}}^{\{Q\}}\right),$$

$$\boldsymbol{B}^{\{q\}} = \left(\mathbf{I} - \mathbf{SR}_{q,Q}\mathbf{P}_q\mathbf{SR}_{q,1}\mathbf{P}_q\right)^{-1} \left(\mathbf{SR}_{q,Q}\mathbf{P}_q\mathbf{ST}_{1,q}\tilde{\boldsymbol{A}}^{\{1\}} + \mathbf{ST}_{Q,q}\tilde{\boldsymbol{B}}^{\{Q\}}\right).$$

C.6 Multi-Layer Structure: Scattering Matrices from Q to $q-1$

The derivations of the scattering matrices follow the procedure outlined in Appendix C.3. Hence, their expressions are merely stated:

$$\mathbf{SR}_{q-1,Q} = \mathbf{R}_{q-1,q} + \mathbf{T}_{q,q-1}\mathbf{P}_q\mathbf{SR}_{q,Q}\mathbf{P}_q \left(\mathbf{I} - \mathbf{R}_{q,q-1}\mathbf{P}_q\mathbf{SR}_{q,Q}\mathbf{P}_q\right)^{-1}\mathbf{T}_{q-1,q}, \tag{C.19a}$$

$$\mathbf{SR}_{Q,q-1} = \mathbf{SR}_{Q,q} + \mathbf{ST}_{q,Q}\mathbf{P}_q\mathbf{R}_{q,q-1}\mathbf{P}_q \left(\mathbf{I} - \mathbf{SR}_{q,Q}\mathbf{P}_q\mathbf{R}_{q,q-1}\mathbf{P}_q\right)^{-1}\mathbf{ST}_{Q,q}, \tag{C.19b}$$

$$\mathbf{ST}_{q-1,Q} = \mathbf{ST}_{q,Q}\mathbf{P}_q \left(\mathbf{I} - \mathbf{R}_{q,q-1}\mathbf{P}_q\mathbf{SR}_{q,Q}\mathbf{P}_q\right)^{-1}\mathbf{T}_{q-1,q}, \tag{C.19c}$$

$$\mathbf{ST}_{Q,q-1} = \mathbf{T}_{q,q-1}\mathbf{P}_q \left(\mathbf{I} - \mathbf{SR}_{q,Q}\mathbf{P}_q\mathbf{R}_{q,q-1}\mathbf{P}_q\right)^{-1}\mathbf{ST}_{Q,q}. \tag{C.19d}$$

C.7 SER Reflections in Three-Layer Structure

The electric field in the dipole layer in a three layer closed geometry is implicitly given through the mode contribution vectors, $\boldsymbol{\epsilon}^{\uparrow}$ and $\boldsymbol{\epsilon}^{\downarrow}$, as described in Section 3.8. This section contains a derivation of expressions for these vectors. Reference is made to Fig. 3.17 for a schematic representation of the three layer geometry.

Firstly, it must be defined in which point the electric field is sought. Strictly, the point cannot be $z = 0$ because the dipole is situated at $z = 0$. However, this point can be approached arbitrarily close from either the positive or the negative direction. In the following, the point of evaluation is chosen as $z = 0^+$, that is, $z = 0$ approached from positive z-values.

The first type of contributions to $\boldsymbol{\epsilon}^{\uparrow}$, $\boldsymbol{\epsilon}^{\uparrow}_{+}$, comes from the part of the field that is initially radiated along the positive z-direction. Since the point of evaluation is placed at $z = 0^+$, the first contribution to $\boldsymbol{\epsilon}^{\uparrow}_{+}$ is given as the field initially radiated outwards from the dipole, given by the modal amplitudes in Eq. (3.35), $\boldsymbol{\mathcal{A}}$. The second contribution to $\boldsymbol{\epsilon}^{\uparrow}_{+}$ comes from the part of the field that has been propagated from $z = 0^+$ to the interface between layers 2 and 3, reflected at this interface, propagated back to the interface between layers 2 and 1, reflected at this interface, and propagated back to $z = 0^+$. The third contribution comes from the part of the field that makes the round trip twice, the fourth contribution makes the round trip three times etc. In total, this yields:

$$\begin{aligned}
\boldsymbol{\epsilon}^{\uparrow}_{+} &= \boldsymbol{\mathcal{A}} + (\mathbf{PR}_{2,1}\mathbf{PPR}_{2,3}\mathbf{P})\boldsymbol{\mathcal{A}} + (\mathbf{PR}_{2,1}\mathbf{PPR}_{2,3}\mathbf{P})^2\boldsymbol{\mathcal{A}} + \ldots \\
&= \sum_{j=0}^{\infty}(\mathbf{PR}_{2,1}\mathbf{PPR}_{2,3}\mathbf{P})^j\boldsymbol{\mathcal{A}} \\
&\equiv \sum_{j=0}^{\infty}(\mathbf{R}_{\text{bot}}\mathbf{R}_{\text{top}})^j\boldsymbol{\mathcal{A}},
\end{aligned} \tag{C.20}$$

with the following definitions:

$$\mathbf{R}_{\text{bot}} \equiv \mathbf{PR}_{2,1}\mathbf{P}, \tag{C.21a}$$

$$\mathbf{R}_{\text{top}} \equiv \mathbf{PR}_{2,3}\mathbf{P}, \tag{C.21b}$$

where $\mathbf{R}_{2,1}$ and $\mathbf{R}_{2,3}$ are the reflection matrices for reflection from layer 2 to layer 1 and from layer 2 to layer 3, respectively, see Section 3.6. $\mathbf{P}$ denotes a propagation matrix, that handles the phase-shift involved in propagation of a distance $L_z/2$. In similarity with the previously defined $\mathbf{P}_q$ matrices from Eq. (3.24) (that handled propagation across an entire layer), the elements of the propagation matrix, $\mathbf{P}$, are defined as:

$$P_{j,k} = \delta_{jk}\exp(i\beta_j L_z/2). \tag{C.22}$$

It is noted that the matrix can also be written by use of the layer propagation matrices defined in Eq. (3.24) as: $\mathbf{P} = \mathbf{P}_2^{1/2}$.

The second type of contributions to $\boldsymbol{\epsilon}^{\uparrow}$, $\boldsymbol{\epsilon}_-^{\uparrow}$, comes from the part of the field that is initially radiated along the negative z-direction. Since the point of evaluation equals $z = 0^+$, the first contribution to $\boldsymbol{\epsilon}_-^{\uparrow}$ is not $\boldsymbol{\mathcal{A}}$, as it was for $\boldsymbol{\epsilon}_+^{\uparrow}$, since the downwards radiated field comes into existence at $z = 0^-$. In turn, the first contribution is the part of the field that has been propagated from $z = 0^-$ to the interface between layers 1 and 2, reflected at this interface and propagated back to $z = 0^+$. The second contribution is the same as the first contribution, but includes the effects of one additional round trip. The third contribution makes two additional round trips etc. Hence:

$$\begin{aligned}\boldsymbol{\epsilon}_-^{\uparrow} &= \mathbf{R}_{\text{bot}}\boldsymbol{\mathcal{A}} + (\mathbf{R}_{\text{bot}}\mathbf{R}_{\text{top}}\mathbf{R}_{\text{bot}})\boldsymbol{\mathcal{A}} + (\mathbf{R}_{\text{bot}}\mathbf{R}_{\text{top}})^2\mathbf{R}_{\text{bot}}\boldsymbol{\mathcal{A}}\ldots \\ &= \sum_{j=0}^{\infty}(\mathbf{R}_{\text{bot}}\mathbf{R}_{\text{top}})^j\mathbf{R}_{\text{bot}}\boldsymbol{\mathcal{A}}. \end{aligned} \tag{C.23}$$

The contribution vector $\boldsymbol{\epsilon}^{\uparrow}$ is then given as the sum of $\boldsymbol{\epsilon}_+^{\uparrow}$ and $\boldsymbol{\epsilon}_-^{\uparrow}$:

$$\begin{aligned}\boldsymbol{\epsilon}^{\uparrow} \equiv \boldsymbol{\epsilon}_+^{\uparrow} + \boldsymbol{\epsilon}_-^{\uparrow} &= \sum_{j=0}^{\infty}(\mathbf{R}_{\text{bot}}\mathbf{R}_{\text{top}})^j\boldsymbol{\mathcal{A}} + \sum_{j=0}^{\infty}(\mathbf{R}_{\text{bot}}\mathbf{R}_{\text{top}})^j\mathbf{R}_{\text{bot}}\boldsymbol{\mathcal{A}} \\ &= \sum_{j=0}^{\infty}(\mathbf{R}_{\text{bot}}\mathbf{R}_{\text{top}})^j(\mathbf{I} + \mathbf{R}_{\text{bot}})\boldsymbol{\mathcal{A}} \\ &= (\mathbf{I} - \mathbf{R}_{\text{bot}}\mathbf{R}_{\text{top}})^{-1}(\mathbf{I} + \mathbf{R}_{\text{bot}})\boldsymbol{\mathcal{A}}. \end{aligned} \tag{C.24}$$

Following the same procedure, $\boldsymbol{\epsilon}^{\downarrow}$ is determined, and the resulting expressions are stated below:

$$\begin{aligned}\boldsymbol{\epsilon}^{\downarrow} \equiv \boldsymbol{\epsilon}_+^{\downarrow} + \boldsymbol{\epsilon}_-^{\downarrow} &= \sum_{j=0}^{\infty}(\mathbf{R}_{\text{top}}\mathbf{R}_{\text{bot}})^j\mathbf{R}_{\text{top}}\boldsymbol{\mathcal{A}} + \sum_{j=1}^{\infty}(\mathbf{R}_{\text{top}}\mathbf{R}_{\text{bot}})^j\boldsymbol{\mathcal{A}} \\ &= \sum_{j=0}^{\infty}(\mathbf{R}_{\text{top}}\mathbf{R}_{\text{bot}})^j(\mathbf{R}_{\text{top}} + \mathbf{I})\boldsymbol{\mathcal{A}} - \boldsymbol{\mathcal{A}} \\ &= (\mathbf{I} - \mathbf{R}_{\text{top}}\mathbf{R}_{\text{bot}})^{-1}(\mathbf{R}_{\text{top}} + \mathbf{I})\boldsymbol{\mathcal{A}} - \boldsymbol{\mathcal{A}} \\ &= (\mathbf{I} - \mathbf{R}_{\text{top}}\mathbf{R}_{\text{bot}})^{-1}(\mathbf{R}_{\text{top}} + \mathbf{I} - (\mathbf{I} - \mathbf{R}_{\text{top}}\mathbf{R}_{\text{bot}}))\boldsymbol{\mathcal{A}} \\ &= (\mathbf{I} - \mathbf{R}_{\text{top}}\mathbf{R}_{\text{bot}})^{-1}\mathbf{R}_{\text{top}}(\mathbf{I} + \mathbf{R}_{\text{bot}})\boldsymbol{\mathcal{A}}. \end{aligned} \tag{C.25}$$

Finally, it is noted that choosing to evaluate the field in $z = 0^-$ rather than in $z = 0^+$ would produce the same results, due to the point-symmetry of the current distribution.

C.8 Convergence Studies for SER Calculations in Three-Layer Structure

This appendix examines the convergence of the power emitted from a dipole in a closed three-layer geometry. This power is given by Eq. (3.46), and convergence is examined with respect to N, the number of included modes.

The convergence studies are carried out for the L_x-range given in Eq. (3.47). In principle, the number of modes should be determined for all values of L_x in Eq. (3.47),

but this procedure is from a computational point of view utopian. Instead, it will be used that the largest number of modes is needed for the largest value of L_x, namely $L_x = 30\,\mu$m. The power ratio, α, is determined for the following values of N:

$$N \in [50, 55, \ldots, 250]. \tag{C.26}$$

To examine the convergence in different n_g-scenarios, four n_g-values are investigated, specifically $n_g = 1.1, 1.5, 2.0, 2.5$. The plot of the appertaining power ratios as functions of the number of modes can be seen in Fig. C.2.

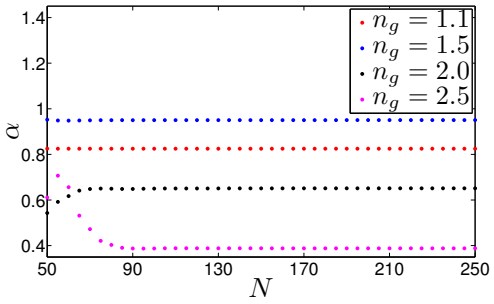

Figure C.2 Convergence study for the number of modes, N, to be included in calculating the power ratio, α, in the three-layer geometry. The refractive index in the guide in the second layer is a parameter.

Finally, the smallest value of N ensuring that the power ratio, for any n_g, deviates less than $\delta\alpha = 10^{-3}$ from a "true" value, is determined. Since no true value is known, the "true" value will be defined as α calculated with 250 modes. The minimum N is therefore determined as:

$$N = \max_i \left(\min_{N_i} \left(|\alpha_i(N_i) - \alpha_i(250)| < 10^{-3} \right) \right), \quad i = 1, 2, 3, 4, \tag{C.27}$$

where the values of i correspond to the four values of n_g. The choice of $\delta\alpha$ is arbitrary, but using the knowledge from the results from the single-layer geometries (p. 34-36), an error on α that is less than one permille is acceptable. Applying the procedure outlined in Eq. (C.27) to the results in Fig. C.2 gives:

$$N = 85. \tag{C.28}$$

Hence, it is estimated that satisfactory convergence should be obtained for $N \geq 85$ in the L_x-range defined in Eq. (3.47) when n_g is within the range $[1.1, 2.5]$.

Appendix D

Chapter 4

D.1 Boundary Condition Matrices

The BC-matrix for the jth guided mode in the open waveguide layer, defined in Section 4.2, is:

$$\mathbf{A}_j = \begin{bmatrix} 1 & -\exp(-ih_j^{[2]}D) & -1 & 0 \\ -h_j^{[1]} & h_j^{[2]}\exp(-ih_j^{[2]}D) & -h_j^{[2]} & 0 \\ 0 & 1 & \exp(ih_j^{[2]}D) & -1 \\ 0 & -h_j^{[2]} & h_j^{[2]}\exp(ih_j^{[2]}D) & -h_j^{[3]} \end{bmatrix}. \tag{D.1}$$

The BC-matrix for the radiation mode with x propagation constant ρ in the open waveguide layer, defined in Section 4.2, is:

$$\mathbf{A}(\rho) = \begin{bmatrix} \mathrm{e}^{i\rho\frac{D}{2}} & \mathrm{e}^{-i\rho\frac{D}{2}} & -\mathrm{e}^{i\rho_{\mathrm{co}}\frac{D}{2}} & -\mathrm{e}^{-i\rho_{\mathrm{co}}\frac{D}{2}} & 0 & 0 \\ -\rho\mathrm{e}^{i\rho\frac{D}{2}} & \rho\mathrm{e}^{-i\rho\frac{D}{2}} & \rho_{\mathrm{co}}\mathrm{e}^{-i\rho_{\mathrm{co}}\frac{D}{2}} & -\rho_{\mathrm{co}}\mathrm{e}^{-i\rho_{\mathrm{co}}\frac{D}{2}} & 0 & 0 \\ 0 & 0 & \mathrm{e}^{-i\rho_{\mathrm{co}}\frac{D}{2}} & \mathrm{e}^{i\rho_{\mathrm{co}}\frac{D}{2}} & -\mathrm{e}^{-i\rho\frac{D}{2}} & -\mathrm{e}^{i\rho\frac{D}{2}} \\ 0 & 0 & -\rho_{\mathrm{co}}\mathrm{e}^{-i\rho_{\mathrm{co}}\frac{D}{2}} & \rho_{\mathrm{co}}\mathrm{e}^{i\rho_{\mathrm{co}}\frac{D}{2}} & \rho\mathrm{e}^{-i\rho\frac{D}{2}} & -\rho\mathrm{e}^{i\rho\frac{D}{2}} \end{bmatrix}. \tag{D.2}$$

D.2 Normalization of Radiation Modes in Uniform Layer

In this appendix, the normalization constant and orthogonality properties of the uniform layer radiation modes are derived. Specifically, this is done by evaluating the integral $\int_{-\infty}^{\infty}\check{\phi}_k(x,s)\check{\phi}_l(x,s')^*\mathrm{d}x,\ k,l=1,2$. Rather than using the piecewise definition of the radiation modes in Eqs. (4.2), a single generic form may be given as:

$$\check{\phi}_l(x,s) = \exp\left[(-1)^l isx\right], \tag{D.3}$$

where for simplicity the field coefficient is assumed equal to unity. Inserting this form into the integral produces:

$$\begin{aligned}\int_{-\infty}^{\infty}\check{\phi}_k(x,s)\check{\phi}_l(x,s')^*\,\mathrm{d}x &= \int_{-\infty}^{\infty}\exp\left[(-1)^k isx\right]\exp\left[-(-1)^l is'x\right]\,\mathrm{d}x \\ &= \int_{-\infty}^{\infty}\exp\left[ix\left((-1)^k s-(-1)^l s'\right)\right]\,\mathrm{d}x \\ &= 2\pi\delta((-1)^k s-(-1)^l s'),\end{aligned} \tag{D.4}$$

where the last equal sign follows from the definition of the Dirac delta function in Eq. (4.18). Since s and s' denote propagation constants for the radiation mode, they are both positive. Consequently, the argument of the Dirac delta function can only equal zero when $l = k$. Using this, the above expression can be reduced by introduction of the Kronecker delta, δ_{kl}, such that:

$$\int_{-\infty}^{\infty} \check{\phi}_k(x,s)\check{\phi}_l(x,s')^* \,\mathrm{d}x = 2\pi\delta_{kl}\delta(s-s'), \tag{D.5}$$

from which it is seen that the normalization constant equals $\mathcal{N} = 2\pi$. Normalized radiation modes are thus given by:

$$\begin{aligned}\phi_l(x,s) &= \frac{1}{\sqrt{\mathcal{N}}}\check{\phi}_l(x,s) \\ &= \frac{1}{\sqrt{2\pi}} \begin{cases} \exp\left(-isx\right), & l = 1, \\ \exp\left(isx\right), & l = 2. \end{cases}\end{aligned} \tag{D.6}$$

Furthermore, from Eq. (D.5), it can be concluded that all uniform layer radiation modes are mutually orthogonal.

D.3 Normalization of Guided Modes in Waveguide Layer

In this appendix, the normalization constant of the jth guided mode in a waveguide layer, $\mathcal{N}_j \equiv \int_{-\infty}^{\infty} |U_j(x)|^2 \,\mathrm{d}x$, used in Section 4.3, is calculated. Firstly, the integral is split into three integrals according to the piecewise definition of $U_j(x)$ in Eq. (4.9):

$$\begin{aligned}\int_{-\infty}^{\infty} |U_j(x)|^2 \,\mathrm{d}x &= \int_{-\infty}^{-\frac{D}{2}} \left|U_j^{[1]}(x)\right|^2 \,\mathrm{d}x + \int_{-\frac{D}{2}}^{\frac{D}{2}} \left|U_j^{[2]}(x)\right|^2 \,\mathrm{d}x + \int_{\frac{D}{2}}^{\infty} \left|U_j^{[3]}(x)\right|^2 \,\mathrm{d}x \\ &= \int_{-\infty}^{-\frac{D}{2}} \left|a_j^{[1]} \exp\left(-ih_j^{[1]}\left(x+\frac{D}{2}\right)\right)\right|^2 \,\mathrm{d}x \\ &\quad + \int_{-\frac{D}{2}}^{\frac{D}{2}} \left|a_j^{[2]} \exp\left(-ih_j^{[2]}\left(x-\frac{D}{2}\right)\right) + b_j^{[2]} \exp\left(ih_j^{[2]}\left(x+\frac{D}{2}\right)\right)\right|^2 \,\mathrm{d}x \\ &\quad + \int_{\frac{D}{2}}^{\infty} \left|b_j^{[3]} \exp\left(ih_j^{[3]}\left(x-\frac{D}{2}\right)\right)\right| \,\mathrm{d}x \\ &\equiv \mathcal{I}_j^{[1]} + \mathcal{I}_j^{[2]} + \mathcal{I}_j^{[3]}.\end{aligned} \tag{D.7}$$

The integrals $\mathcal{I}_j^{[1]}$ and $\mathcal{I}_j^{[3]}$ can be evaluated using that the propagation constants $h_j^{[1,3]}$ are positive imaginary for guided modes:

$$\begin{aligned}
\mathcal{I}_j^{[1]} &= \left|a_j^{[1]}\right|^2 \int_{-\infty}^{-\frac{D}{2}} \left|\exp\left(\operatorname{Im}\left(h_j^{[1]}\right)\left(x+\frac{D}{2}\right)\right)\right|^2 \mathrm{d}x \\
&= \left|a_j^{[1]}\right|^2 \int_{-\infty}^{-\frac{D}{2}} \exp\left(2\operatorname{Im}\left(h_j^{[1]}\right)\left(x+\frac{D}{2}\right)\right) \mathrm{d}x \\
&= \frac{\left|a_j^{[1]}\right|^2}{2\operatorname{Im}\left(h_j^{[1]}\right)} \left[\exp\left(2\operatorname{Im}\left(h_j^{[1]}\right)\left(x+\frac{D}{2}\right)\right)\right]_{-\infty}^{-\frac{D}{2}} \\
&= \frac{\left|a_j^{[1]}\right|^2}{2\operatorname{Im}\left(h_j^{[1]}\right)}.
\end{aligned} \tag{D.8a}$$

In a similar manner, the integral $\mathcal{I}_j^{[3]}$ is determined as:

$$\mathcal{I}_j^{[3]} = \frac{\left|b_j^{[3]}\right|^2}{2\operatorname{Im}\left(h_j^{[3]}\right)}. \tag{D.8b}$$

In the case of symmetry, that is, when the refractive indices in zones 1 and 3 are equal, the propagation constants fulfill $h_j^{[1]} = h_j^{[3]}$, and the absolute value of the field coefficients are then identical, $\left|a_j^{[1]}\right| = \left|b_j^{[3]}\right|$, such that $\mathcal{I}_j^{[1]} = \mathcal{I}_j^{[3]}$. The integral $\mathcal{I}_j^{[2]}$ can be evaluated in the following manner where it is used that $h_j^{[2]}$ is real:

$$\begin{aligned}
\mathcal{I}_j^{[2]} &= \int_{-\frac{D}{2}}^{\frac{D}{2}} \left[a_j^{[2]}\mathrm{e}^{-ih_j^{[2]}\left(x-\frac{D}{2}\right)} + b_j^{[2]}\mathrm{e}^{ih_j^{[2]}\left(x+\frac{D}{2}\right)}\right]\left[a_j^{[2]}\mathrm{e}^{-ih_j^{[2]}\left(x-\frac{D}{2}\right)} + b_j^{[2]}\mathrm{e}^{ih_j^{[2]}\left(x+\frac{D}{2}\right)}\right]^* \mathrm{d}x \\
&= \int_{-\frac{D}{2}}^{\frac{D}{2}} \left|a_j^{[2]}\right|^2 + \left|b_j^{[2]}\right|^2 + a_j^{[2]}\left(b_j^{[2]}\right)^* \mathrm{e}^{-2ih_j^{[2]}x} + \left(a_j^{[2]}\right)^* b_j^{[2]}\mathrm{e}^{2ih_j^{[2]}x}\,\mathrm{d}x \\
&= D\left(\left|a_j^{[2]}\right|^2 + \left|b_j^{[2]}\right|^2\right) + \int_{-\frac{D}{2}}^{\frac{D}{2}} 2\operatorname{Re}\left(a_j^{[2]}\left(b_j^{[2]}\right)^*\right)\cos\left(2h_j^{[2]}x\right)\,\mathrm{d}x \\
&= D\left(\left|a_j^{[2]}\right|^2 + \left|b_j^{[2]}\right|^2\right) + \operatorname{Re}\left(a_j^{[2]}\left(b_j^{[2]}\right)^*\right)\frac{1}{h_j^{[2]}}\left[\sin\left(2h_j^{[2]}x\right)\right]_{-\frac{D}{2}}^{\frac{D}{2}} \\
&= D\left(\left|a_j^{[2]}\right|^2 + \left|b_j^{[2]}\right|^2\right) + 2\operatorname{Re}\left(a_j^{[2]}\left(b_j^{[2]}\right)^*\right)\frac{\sin\left(h_j^{[2]}D\right)}{h_j^{[2]}}.
\end{aligned} \tag{D.8c}$$

Adding the sub-integrals $\mathcal{I}_j^{[1]}$, $\mathcal{I}_j^{[2]}$ and $\mathcal{I}_j^{[3]}$ from Eqs. (D.8) gives $\int_{-\infty}^{\infty} |U_j(x)|^2\,\mathrm{d}x$:

$$\begin{aligned}
\int_{-\infty}^{\infty} |U_j(x)|^2\,\mathrm{d}x = &\frac{\left|a_j^{[1]}\right|^2}{2\operatorname{Im}\left(h_j^{[1]}\right)} + \frac{\left|b_j^{[3]}\right|^2}{2\operatorname{Im}\left(h_j^{[3]}\right)} \\
&+ D\left(\left|a_j^{[2]}\right|^2 + \left|b_j^{[2]}\right|^2\right) + 2\operatorname{Re}\left(a_j^{[2]}\left(b_j^{[2]}\right)^*\right)\frac{\sin\left(h_j^{[2]}D\right)}{h_j^{[2]}}
\end{aligned} \tag{D.9}$$

D.4 Repetition Length

This appendix serves to introduce the repetition length, L_{rep}, that is the length over which the electric field in an open and uniform layer repeats itself when approximated by a Riemann sum. The electric field in such a layer may be expressed as in Eq. (4.25):

$$E(x,z) = \int_0^\infty A_l(s)\exp(\mp i\gamma(s)z)\big[\exp(-ixs) + \exp(+ixs)\big]\,\mathrm{d}s. \tag{D.10}$$

The integral over s may be numerically approximated by use of a Riemann sum in the following way:

$$E(x,z) \simeq \sum_{j=1}^{\#} A_l(j\Delta s)\exp(\mp i\gamma(j\Delta s)z)\big[\exp(-ixj\Delta s) + \exp(+ixj\Delta s)\big]\Delta s, \tag{D.11}$$

where Δs is a fixed s-step length: $\Delta s \equiv |s_{j+1} - s_j|$ for any $j = 1, 2, \ldots, \# - 1$. Since $\exp(\mp isx) = \exp(\mp i(sx + 2\pi))$, this and the approximate field expression in Eq. (D.11) can be applied to determine the length along x over which the field repeats itself:

$$L_{\text{rep}} = \frac{2\pi}{\Delta s}. \tag{D.12}$$

From this, it is apparent that in the limit $\Delta s \to 0$, which is in fact the definition of the Riemann integral, the field does not repeat itself as would be expected. However, for finite Δs, and thus in practice for all numerical implementations, the approximation of the field in the open geometry imposes a repetition of the field, whose period, L_{rep}, is dependent on the discretization of s through Eq. (D.12). The s-step length, Δs, is related to the number of subintervals, #, through:

$$\Delta s = \frac{nk_0}{\#}, \tag{D.13}$$

where the integration range has been assumed of width nk_0. Combining Eqs. (D.12) and (D.13) gives:

$$L_{\text{rep}} = \frac{2\pi\#}{nk_0}. \tag{D.14}$$

Appendix E

Chapter 5

E.1 Derivation of Fredholm Equation for Illumination by Fundamental Mode

This appendix presents a derivation of the integral equation that governs the mode coupling at the interface between the waveguide layer and the uniform layer when the waveguide layer is illuminated by the fundamental mode. The derivation largely follows the procedure outlined in [Capsalis].

First, the reflection and transmission coefficient expressions in Eqs. (5.1) are derived by use of the continuity condition at $z = 0$. Evaluating $E_1(x, z)$ and $E_2(x, z)$ at $z = 0$ and equating produces:

$$U_1(x)\,[1 + R_1] + \sum_{m=1}^{2} \int_0^\infty R(\rho)\psi_m(x, \rho)\,\mathrm{d}\rho = \sum_{l=1}^{\infty} \int_0^\infty T(s)\phi_l(x, s)\,\mathrm{d}s = \Phi(x). \quad \text{(E.1)}$$

To derive the reflection coefficient R_1, the first and third members of Eq. (E.1) are multiplied by $U_1(x)^*$ and integrated across the entire x-axis:

$$[1 + R_1] \int_{-\infty}^{\infty} U_1(x)U_1(x)^*\,\mathrm{d}x + \int_{-\infty}^{\infty} \sum_{m=1}^{2} \int_0^\infty R(\rho)\psi_m(x, \rho)\,\mathrm{d}\rho\, U_1(x)^*\,\mathrm{d}x = \int_{-\infty}^{\infty} \Phi(x)U_1(x)^*\,\mathrm{d}x. \quad \text{(E.2)}$$

Interchanging the order of integration and applying the orthonormality relations in Eqs. (4.24a) and (4.24d) reduces the equations to:

$$R_1 = -1 + \int_{-\infty}^{\infty} \Phi(x)U_1(x)^*\,\mathrm{d}x. \quad \text{(E.3)}$$

Similarly, multiplying the first and third members of Eq. (E.1) with $\psi_k(x, \rho')^*$ and integrating across the x-axis produces:

$$[1 + R_1] \int_{-\infty}^{\infty} U_1(x)\psi_k(x, \rho')^*\,\mathrm{d}x + \int_{-\infty}^{\infty} \sum_{m=1}^{2} \int_0^\infty R(\rho)\psi_m(x, \rho)\,\mathrm{d}\rho\, \psi_k(x, \rho')^*\,\mathrm{d}x = \int_{-\infty}^{\infty} \Phi(x)\psi_k(x, \rho')^*\,\mathrm{d}x. \quad \text{(E.4)}$$

Again, interchanging the order of integration and applying the orthonormality relations in Eqs. (4.24b) and (4.24d) produces:

$$\sum_{m=1}^{2}\int_0^\infty R(\rho)\delta_{mk}\delta(\rho-\rho')\,\mathrm{d}\rho = \int_{-\infty}^{\infty}\Phi(x)\psi_k(x,\rho')^*\,\mathrm{d}x$$
$$\Leftrightarrow R(\rho') = \int_{-\infty}^{\infty}\Phi(x)\psi_k(x,\rho')^*\,\mathrm{d}x, \tag{E.5}$$

Finally, by multiplying the second and third members of Eq. (E.1) with $\phi_k^*(x,s')$, integrating across the x-axis and applying the orthonormality relation from Eq. (4.24c), the transmission coefficients are obtained as:

$$T(s) = \int_{-\infty}^{\infty}\Phi(x)\phi_l(x,s)^*\,\mathrm{d}x, \tag{E.6}$$

for $l = 1, 2$.

The second z-BC, differentiability at $z = 0$, can be applied to $E_1(x,z)$ and $E_2(x,z)$ by assuming that the operation of differentiating under the integral sign is valid. Carrying out this differentiation produces the following relation:

$$U_1(x)\beta_1\left[-1+R_1\right] + \sum_{m=1}^{2}\int_0^\infty \beta(\rho)R(\rho)\psi_m(x,\rho)\,\mathrm{d}\rho + \sum_{l=1}^{2}\int_0^\infty \gamma(s)T(s)\phi_l(x,s)\,\mathrm{d}s = 0. \tag{E.7}$$

Inserting the relations obtained for R_1, $R(\rho)$ and $T(s)$ from Eqs. (E.3), (E.5) and (E.6), respectively, into the above expression then produces a Fredholm equation of the first kind:

$$\begin{aligned} &U_1(x)\beta_1\left[-2+\int_{-\infty}^{\infty}\Phi(x')U_1(x')^*\,\mathrm{d}x'\right] \\ &+\sum_{m=1}^{2}\int_0^\infty \psi_m(x,\rho)\beta(\rho)\int_{-\infty}^{\infty}\Phi(x')\psi_m(x',\rho)^*\,\mathrm{d}x'\,\mathrm{d}\rho \\ &+\sum_{l=1}^{2}\int_0^\infty \phi_l(x,s)\gamma(s)\int_{-\infty}^{\infty}\Phi(x')\phi_l(x',s)^*\,\mathrm{d}x'\,\mathrm{d}s = 0. \end{aligned} \tag{E.8}$$

This equation can be expressed more compactly as:

$$\int_{-\infty}^{\infty}\Phi(x')K_1(x,x')\,\mathrm{d}x' = 2U_1(x)\beta_1, \tag{E.9}$$

where $K_1(x,x')$ denotes the kernel of the integral equation:

$$\begin{aligned} K_1(x,x') = \beta_1 U_1(x)U_1(x')^* &+ \sum_{m=1}^{2}\int_0^\infty \beta(\rho)\psi_m(x,\rho)\psi_m(x',\rho)^*\,\mathrm{d}\rho \\ &+\sum_{l=1}^{2}\int_0^\infty \gamma(s)\phi_l(x,s)\phi_l(x',s)^*\,\mathrm{d}s. \end{aligned} \tag{E.10}$$

Solutions to Fredholm equations of the first kind are not trivially found [Baker, p. 40], and conversion into a Fredholm equation of the second kind is consequently desired. This

can be carried out by creative use of the completeness relations in Eqs. (4.24e) and (4.24f). Specifically, the completeness relations can be rewritten as the following zero-identities:

$$0 = k_0 n_1 \left[-U_1(x)U_1(x')^* - \sum_{m=1}^{2} \int_0^\infty \psi_m(x,\rho)\psi_m(x',\rho)^* \,\mathrm{d}\rho + \delta(x-x') \right], \tag{E.11a}$$

$$0 = k_0 n_0 \left[-\sum_{l=1}^{2} \int_0^\infty \phi_l(x,s)\phi_l(x',s)^* \,\mathrm{d}s + \delta(x-x') \right]. \tag{E.11b}$$

To ensure that the terms in these zero-identities have meaningful dimensions and values compared to the terms in the kernel, $K_1(x,x')$, the zero identities have been multiplied by $k_0 n_1$ and $k_0 n_0$, respectively. The choice of n_1 versus n_0 relates directly to the definitions of ρ and s. Adding these zero-identities to $K_1(x,x')$ and applying the properties of the Dirac delta function produces a Fredholm equation of the second kind in the aperture field:

$$\Phi(x) = \Phi_0(x) + \lambda \int_{-\infty}^{\infty} \Phi(x')K_2(x,x') \,\mathrm{d}x'. \tag{E.12}$$

where the zeroth order aperture field, $\Phi_0(x)$, the integral prefactor, λ, and the kernel, $K_2(x,x') \equiv K(x,x')$ are presented in Eqs. (5.3b)-(5.3d).

E.2 Overlap Integral: $\langle U_1, \phi_l(s)\rangle_{L^2}$

The overlap integral $\langle U_1, \phi_l(s)\rangle_{L^2}$ is defined through:

$$\langle U_1, \phi_l(s)\rangle_{L^2} = \int_{-\infty}^{\infty} U_1(x)\phi_l(x,s)^* \,\mathrm{d}x. \tag{E.13}$$

The uniform layer radiation modes, $\phi_l(x,s)$, are given in Eq. (4.19), and by use of Euler's formula they may be recast in terms of cosines and sines:

$$\phi_l(x,s) = \frac{1}{\sqrt{2\pi}} \begin{cases} \cos(sx) - i\sin(sx), & l = 1, \\ \cos(sx) + i\sin(sx), & l = 2. \end{cases} \tag{E.14}$$

Since $U_1(x)$ is an even function, the integral over the sine-terms vanish whereby the overlap integral reduces to:

$$\langle U_1, \phi_l(s)\rangle_{L^2} = \frac{1}{\sqrt{2\pi}} \int_{-\infty}^{\infty} U_1(x)\cos(sx) \,\mathrm{d}x. \tag{E.15}$$

From the above, it is clear that the overlap integral is independent of l. Inserting the expression for $U_1(x)$ from Eq. (4.9), the overlap integral may be split into three sub-integrals:

$$\begin{aligned} \langle U_1, \phi_l(s)\rangle_{L^2} = \frac{1}{\sqrt{2\pi}} \Bigg\{ & \int_{-\infty}^{-\frac{D}{2}} a_j^{[1]} \mathrm{e}^{-ih_j^{[1]}\left(x+\frac{D}{2}\right)} \cos(sx) \,\mathrm{d}x \\ & + \int_{-\frac{D}{2}}^{\frac{D}{2}} \left[a_j^{[2]} \mathrm{e}^{-ih_j^{[2]}\left(x-\frac{D}{2}\right)} + b_j^{[2]} \mathrm{e}^{ih_j^{[2]}\left(x+\frac{D}{2}\right)} \right] \cos(sx) \,\mathrm{d}x \\ & + \int_{\frac{D}{2}}^{\infty} b_j^{[3]} \mathrm{e}^{ih_j^{[3]}\left(x-\frac{D}{2}\right)} \cos(sx) \,\mathrm{d}x \Bigg\} \end{aligned} \tag{E.16}$$

The evaluation of these integrals are straightforward using the following integral-identity [Schaums, Eq. 17.25.11]:

$$\int \mathrm{e}^{cx}\cos(dx)\,\mathrm{d}x = \frac{\mathrm{e}^{cx}\left[c\cos(dx)+d\sin(dx)\right]}{c^2+d^2}, \tag{E.17}$$

where c and d are constants. Applying this integral-identity and the fact that $h_j^{[1]}$ and $h_j^{[3]}$ are purely imaginary produces the following result:

$$\begin{aligned}\langle U_1,\phi_l(s)\rangle_{L^2} = \frac{1}{\sqrt{2\pi}}\Bigg\{ &-\frac{a_j^{[1]}}{s^2-\left(h_j^{[1]}\right)^2}\left[ih_j^{[1]}\cos\left(s\tfrac{D}{2}\right)+s\sin\left(s\tfrac{D}{2}\right)\right]\\ &+\frac{2\left(a_j^{[2]}+b_j^{[2]}\right)\mathrm{e}^{ih_j^{[2]}D/2}}{s^2-\left(h_j^{[2]}\right)^2}\left[s\cos\left(h_j^{[2]}\tfrac{D}{2}\right)\sin\left(s\tfrac{D}{2}\right)\right.\\ &\left.-h_j^{[2]}\sin\left(h_j^{[2]}\tfrac{D}{2}\right)\cos\left(s\tfrac{D}{2}\right)\right]\\ &-\frac{b_j^{[3]}}{s^2-\left(h_j^{[3]}\right)^2}\left[ih_j^{[3]}\cos\left(s\tfrac{D}{2}\right)+s\sin\left(s\tfrac{D}{2}\right)\right]\Bigg\}.\end{aligned} \tag{E.18}$$

Since the guided mode $U_1(x)$ is even, the cladding coefficients are equal, $a_j^{[1]} = b_j^{[3]}$. Similarly, the core coefficients are equal, $a_j^{[2]} = b_j^{[2]}$. Finally, the propagation constants in the cladding region are also identical, that is, $h_j^{[1]} = h_j^{[3]}$. Hence, in the case of a symmetric waveguide, the overlap integral reduces to:

$$\begin{aligned}\langle U_1,\phi_l(s)\rangle_{L^2} =&\frac{1}{\sqrt{2\pi}}\Bigg\{-\frac{2a_j^{[1]}}{s^2-\left(h_j^{[1]}\right)^2}\left[ih_j^{[1]}\cos\left(s\tfrac{D}{2}\right)+s\sin\left(s\tfrac{D}{2}\right)\right]\\ &+\frac{4a_j^{[2]}\mathrm{e}^{ih_j^{[2]}D/2}}{s^2-\left(h_j^{[2]}\right)^2}\left[s\cos\left(h_j^{[2]}\tfrac{D}{2}\right)\sin\left(s\tfrac{D}{2}\right)-h_j^{[2]}\sin\left(h_j^{[2]}\tfrac{D}{2}\right)\cos\left(s\tfrac{D}{2}\right)\right]\Bigg\}.\end{aligned} \tag{E.19}$$

E.3 Overlap Integral: $\langle \psi_m(\rho), \phi_l(s)\rangle_{L^2}$

In this appendix, expressions for the overlap integral between a waveguide layer radiation mode, $\psi_m(x,\rho)$, and a uniform layer radiation mode, $\phi_l(x,\rho)$, are derived. This overlap integral, $\langle\psi_m(\rho),\phi_l(s)\rangle_{L^2}$, plays an important role in the determination of the various reflection and transmission coefficients that are introduced for the two-layer open geometry in Chapter 5. Before the expressions are derived, two improper integrals that are encountered in the determination of these expressions are presented.

$\delta^+(x)$ and $\delta^-(x)$

In the derivation of expressions for $\langle \psi_m(\rho), \phi_l(s) \rangle_{L^2}$, the following semi-infinite integrals appear:

$$\delta^+(k) \equiv \frac{1}{2\pi} \int_0^\infty \exp(ikx)\, \mathrm{d}x, \tag{E.20a}$$

$$\delta^-(k) \equiv \frac{1}{2\pi} \int_{-\infty}^0 \exp(ikx)\, \mathrm{d}x. \tag{E.20b}$$

These integrals are termed $\delta^+(k)$ and $\delta^-(k)$ since by the (weak) definition of the Dirac delta function in Eq. (4.18) their sum equals the Dirac delta function, $\delta(k) = \delta^+(k) + \delta^-(k)$.

As the two integrals are each other's mirrors through:

$$\delta^-(k) = \frac{1}{2\pi} \int_{-\infty}^0 \exp(ikx)\, \mathrm{d}x = \frac{1}{2\pi} \int_0^\infty \exp(-ikx)\, \mathrm{d}x = \delta^+(-k), \tag{E.21}$$

focus in the following is put on expressing $\delta^+(k)$. Expanding $\delta^+(k)$ by use of Euler's formula for the complex exponential yields:

$$\delta^+(k) \equiv \frac{1}{2\pi} \left\{ \int_0^\infty \cos(kx)\, \mathrm{d}x + i \int_0^\infty \sin(kx)\, \mathrm{d}x \right\}. \tag{E.22}$$

Using the definition of $\delta(k)$ in Eq. (4.18) and the fact that cosine is an even function and sine an odd functions gives:

$$\begin{aligned} \delta(k) &= \frac{1}{2\pi} \left\{ \int_{-\infty}^\infty \cos(kx)\, \mathrm{d}x + i \int_{-\infty}^\infty \sin(kx)\, \mathrm{d}x \right\} \\ &= \frac{1}{\pi} \int_0^\infty \cos(kx)\, \mathrm{d}x, \\ &\Updownarrow \\ \int_0^\infty \cos(kx)\, \mathrm{d}x &= \pi\delta(k). \end{aligned} \tag{E.23}$$

Expressing the semi-infinite sine-integral in Eq. (E.22) is less straightforward. Initially, the sine-integral is rewritten by use of the trigonometric identity $\sin(x) = \cos(x - \pi/2)$, and then transformed by the substitution $x = y + \pi/(2k)$:

$$\begin{aligned} \int_0^\infty \sin(kx)\, \mathrm{d}x &= \int_0^\infty \cos\left(kx - \tfrac{\pi}{2}\right)\, \mathrm{d}x \\ &= \int_{-\frac{\pi}{2k}}^\infty \cos\left(ky\right)\, \mathrm{d}y \qquad \text{(E.24)} \\ &= \int_{-\frac{\pi}{2k}}^0 \cos\left(ky\right)\, \mathrm{d}y + \int_0^\infty \cos\left(ky\right)\, \mathrm{d}y \\ &= \int_{-\frac{\pi}{2k}}^0 \cos\left(ky\right)\, \mathrm{d}y + \pi\delta(k), \qquad \text{(E.25)} \end{aligned}$$

where the last equal sign follows from the relation in Eq. (E.23). Further evaluation of the expression must take into account two cases: $k \neq 0$ and $k = 0$. For $k \neq 0$, the first

term in Eq. (E.25) is:

$$\int_{-\frac{\pi}{2k}}^{0} \cos(ky)\ \mathrm{d}y = \frac{1}{k}, \tag{E.26}$$

and the Delta function is not evaluated at $k = 0$ which then gives:

$$\int_0^\infty \sin(kx)\,\mathrm{d}x = \frac{1}{k}, \qquad k \neq 0. \tag{E.27}$$

When $k = 0$ that integrand of the original integral, $\sin(kx)$, vanishes, and hence:

$$\int_0^\infty \sin(kx)\,\mathrm{d}x = 0, \qquad k = 0. \tag{E.28}$$

Remembering that the sine integral represents a distribution to be evaluated under a k-integral, the expression is conveniently expressed as:

$$\int_0^\infty \sin(kx)\,\mathrm{d}x = PV\left(\frac{1}{k}\right), \tag{E.29}$$

where PV denotes the Cauchy principal value. This effectively ensures that any discontinuity of the integrand, in this case $1/k$, is skipped upon evaluation under a k-integral. For simplicity, the explicit Cauchy principal value is omitted, but it must be stressed that integrations must avoid evaluation in $k = 0$. It is noted that the result is in agreement with the use in [Vats].

Combining the results for the cosine and sine integrals and inserting in Eq. (E.22) then yield an explicit expression for $\delta^+(k)$:

$$\delta^+(k) = \frac{\delta(k)}{2} + \frac{i}{2\pi k}. \tag{E.30a}$$

By the property in Eq. (E.21), this gives the following expression for $\delta^-(k)$:

$$\delta^-(k) = \frac{\delta(k)}{2} - \frac{i}{2\pi k}, \tag{E.30b}$$

where it has been used that the Dirac delta function is an even function, $\delta(k) = \delta(-k)$.

Derivation of $\langle \boldsymbol{\psi_m}, \boldsymbol{\phi_l} \rangle_{\boldsymbol{L^2}}$

Explicit expressions for the overlap integral, or inner product, of a waveguide layer radiation mode, $\psi_m(x, \rho)$, and a uniform layer radiation mode, $\phi_l(x, s)$, are in this section derived. The inner product is defined as:

$$\langle \psi_m(\rho), \phi_l(s) \rangle_{L^2} = \int_{-\infty}^{\infty} \psi_m(x, \rho)\phi_l(x, s)^*\,\mathrm{d}x, \tag{E.31}$$

where $\phi_l(x, s)$ and $\psi_m(x, \rho)$ are defined in Eqs. (4.19) and (4.23). In the following, the inner product is expressed for arbitrary m and l. The field coefficients of $\psi_m(x, \rho)$ are assumed chosen such that the modes are normalized.

Due to the piecewise definition of $\psi_m(x,\rho)$, the inner product is expressed as follows:

$$\begin{aligned}\langle\psi_m(\rho),\phi_l(s)\rangle_{L^2} = \frac{1}{\sqrt{2\pi}}\Bigg\{ &\int_{-\infty}^{-D/2}\left[a^{[1]}\exp(-i\rho x)+b^{[1]}\exp(i\rho x)\right]\exp(-i(-1)^l sx)\,\mathrm{d}x\\ &+\int_{-D/2}^{D/2}\left[a^{[2]}\exp(-i\rho_{\mathrm{co}}x)+b^{[2]}\exp(i\rho_{\mathrm{co}}x)\right]\exp(-i(-1)^l sx)\,\mathrm{d}x\\ &+\int_{D/2}^{\infty}\left[a^{[3]}\exp(-i\rho x)+b^{[3]}\exp(i\rho x)\right]\exp(-i(-1)^l sx)\,\mathrm{d}x\Bigg\} \quad \text{(E.32)}\\ \equiv \frac{1}{\sqrt{2\pi}}&\Big[\mathrm{I}_{m,l}(\rho,s)+\mathrm{II}_{m,l}(\rho,s)+\mathrm{III}_{m,l}(\rho,s)\Big]. \quad \text{(E.33)}\end{aligned}$$

For the sake of clarity, each of the above integrals are treated separately:

$$\begin{aligned}\mathrm{I}_{m,l}(\rho,s) \equiv &\int_{-\infty}^{-D/2}\left[a^{[1]}\exp(-i\rho x)+b^{[1]}\exp(i\rho x)\right]\exp(-i(-1)^l sx)\,\mathrm{d}x\\ &= a^{[1]}\int_{-\infty}^{0}\exp(ix(-\rho-(-1)^l s))\,\mathrm{d}x + b^{[1]}\int_{-\infty}^{0}\exp(ix(\rho-(-1)^l s))\,\mathrm{d}x\\ &\quad - a^{[1]}\int_{-D/2}^{0}\exp(ix(-\rho-(-1)^l s))\,\mathrm{d}x - b^{[1]}\int_{-D/2}^{0}\exp(ix(\rho-(-1)^l s))\,\mathrm{d}x\\ &= 2\pi a^{[1]}\delta^-(-\rho-(-1)^l s)+2\pi b^{[1]}\delta^-(\rho-(-1)^l s)+\tau^{(\mathrm{I})}_{m,l}(\rho,s), \quad \text{(E.34)}\end{aligned}$$

where the definition of $\delta^-(k)$ from Eq. (E.20b) has been used, and where the following shorthand notation has been used for the proper integrals:

$$\begin{aligned}\tau^{(\mathrm{I})}_{m,l}(\rho,s) \equiv &-a^{[1]}\int_{-D/2}^{0}\exp(ix(-\rho-(-1)^l s))\,\mathrm{d}x - b^{[1]}\int_{-D/2}^{0}\exp(ix(\rho-(-1)^l s))\,\mathrm{d}x\\ &= -\frac{ia^{[1]}}{\rho+(-1)^l s}\left[1-\exp\left(i\left(\rho+(-1)^l s\right)\frac{D}{2}\right)\right]\\ &\quad +\frac{ib^{[1]}}{\rho-(-1)^l s}\left[1-\exp\left(i\left(-\rho+(-1)^l s\right)\frac{D}{2}\right)\right]. \quad \text{(E.35)}\end{aligned}$$

An expression for the second integral in Eq. (E.32) is:

$$\begin{aligned}\mathrm{II}_{m,l}(\rho,s) \equiv &\int_{-D/2}^{D/2}\left[a^{[2]}\exp(-i\rho_{\mathrm{co}}x)+b^{[2]}\exp(i\rho_{\mathrm{co}}x)\right]\exp(-i(-1)^l sx)\,\mathrm{d}x\\ &= a^{[2]}\int_{-D/2}^{D/2}\exp(-ix(\rho_{\mathrm{co}}+(-1)^l s))\,\mathrm{d}x + b^{[2]}\int_{-D/2}^{D/2}\exp(ix(\rho_{\mathrm{co}}-(-1)^l s))\,\mathrm{d}x\\ &= \frac{2a^{[2]}}{\rho_{\mathrm{co}}+(-1)^l s}\sin\left((\rho_{\mathrm{co}}+(-1)^l s)\frac{D}{2}\right)+\frac{2b^{[2]}}{\rho_{\mathrm{co}}-(-1)^l s}\sin\left((\rho_{\mathrm{co}}-(-1)^l s)\frac{D}{2}\right). \quad \text{(E.36)}\end{aligned}$$

Finally, the third integral in Eq. (E.32) is expressed:

$$\begin{aligned}
\mathrm{III}_{m,l}(\rho,s) \equiv & \int_{D/2}^{\infty} \left[a^{[3]}\exp(-i\rho x) + b^{[3]}\exp(i\rho x)\right]\exp(-i(-1)^l s x)\,\mathrm{d}x \\
= & \, a^{[3]}\int_0^{\infty}\exp(ix(-\rho-(-1)^l s))\,\mathrm{d}x + b^{[3]}\int_0^{\infty}\exp(ix(\rho-(-1)^l s))\,\mathrm{d}x \\
& - a^{[3]}\int_0^{D/2}\exp(ix(-\rho-(-1)^l s))\,\mathrm{d}x - b^{[3]}\int_0^{D/2}\exp(ix(\rho-(-1)^l s))\,\mathrm{d}x \\
= & \, 2\pi a^{[3]}\delta^+(-\rho-(-1)^l s) + 2\pi b^{[3]}\delta^+(\rho-(-1)^l s) + \tau^{(\mathrm{III})}_{m,l}(\rho,s), \qquad \text{(E.37)}
\end{aligned}$$

where the definition of $\delta^+(k)$ from Eq. (E.20a) and the following shorthand notation for the proper integrals have been used:

$$\begin{aligned}
\tau^{(\mathrm{III})}_{m,l}(\rho,s) \equiv & -a^{[3]}\int_0^{D/2}\exp(ix(-\rho-(-1)^l s))\,\mathrm{d}x - b^{[3]}\int_0^{D/2}\exp(ix(\rho-(-1)^l s))\,\mathrm{d}x \\
= & -\frac{ia^{[3]}}{\rho+(-1)^l s}\left[\exp\left(-i\left(\rho+(-1)^l s\right)\frac{D}{2}\right)-1\right] \\
& + \frac{ib^{[3]}}{\rho-(-1)^l s}\left[\exp\left(i\left(\rho-(-1)^l s\right)\frac{D}{2}\right)-1\right]. \qquad \text{(E.38)}
\end{aligned}$$

Having expressed the three sub-integrals that constitute $\langle\psi_m,\phi_l\rangle_{L^2}$ these may be collected to express the inner product:

$$\begin{aligned}
\langle\psi_m(\rho),\phi_l(s)\rangle_{L^2} \equiv & \frac{1}{\sqrt{2\pi}}\Big[\mathrm{I}_{m,l}(\rho,s)+\mathrm{II}_{m,l}(\rho,s)+\mathrm{III}_{m,l}(\rho,s)\Big] \\
= & \frac{1}{\sqrt{2\pi}}\Bigg\{2\pi\Big[a^{[1]}\delta^-(-\rho-(-1)^l s)+b^{[1]}\delta^-(\rho-(-1)^l s) \\
& + a^{[3]}\delta^+(-\rho-(-1)^l s)+b^{[3]}\delta^+(\rho-(-1)^l s)\Big] \\
& + \tau_{m,l}(\rho,s)+\mathrm{II}_{m,l}(\rho,s)\Bigg\}, \qquad \text{(E.39)}
\end{aligned}$$

with:

$$\tau_{m,l}(\rho,s) \equiv \tau^{(\mathrm{I})}_{m,l}(\rho,s) + \tau^{(\mathrm{III})}_{m,l}(\rho,s). \qquad \text{(E.40)}$$

Applying the expressions for $\delta^+(k)$ and $\delta^-(k)$ from Eqs. (E.30) further gives:

$$\begin{aligned}
\langle\psi_m(\rho),\phi_l(s)\rangle_{L^2} = & \frac{1}{\sqrt{2\pi}}\Bigg\{2\pi\Bigg[a^{[1]}\left(\frac{\delta(\rho+(-1)^l s)}{2}+\frac{i}{2\pi(\rho+(-1)^l s)}\right) \\
& + b^{[1]}\left(\frac{\delta(\rho-(-1)^l s)}{2}-\frac{i}{2\pi(\rho-(-1)^l s)}\right) \\
& + a^{[3]}\left(\frac{\delta(\rho+(-1)^l s)}{2}-\frac{i}{2\pi(\rho+(-1)^l s)}\right) \\
& + b^{[3]}\left(\frac{\delta(\rho-(-1)^l s)}{2}+\frac{i}{2\pi(\rho-(-1)^l s)}\right)\Bigg] \\
& + \tau_{m,l}(\rho,s)+\mathrm{II}_{m,l}(\rho,s)\Bigg\}. \qquad \text{(E.41)}
\end{aligned}$$

The expression in Eq. (E.41) is the final, general and explicit expression for $\langle\psi_m(\rho),\phi_l(s)\rangle_{L^2}$. In the following, it is argued how the expression may be reduced when considering a specific l.

The inner product only occurs under ρ- and s-integrals, see e.g. Eq. (5.12), and both s and ρ are positive. Therefore, the Dirac delta functions, with sums and subtractions of ρ and s as arguments, are only acting operators if the arguments can equal zero in the integration range, that is, only when ρ and s are of opposite signs. Consequently, the terms $\delta(\rho+s)$ and $\delta(-\rho-s)$ can be omitted. Using this, $\langle\psi_m(\rho),\phi_1(s)\rangle_{L^2}$ and $\langle\psi_m(\rho),\phi_2(s)\rangle_{L^2}$ may be expressed as:

$$\begin{aligned}\langle\psi_m(\rho),\phi_1(s)\rangle_{L^2} = \frac{1}{\sqrt{2\pi}}\Bigg\{ & a^{[1]}\left(\pi\delta(\rho-s)+\frac{i}{\rho-s}\right)-\frac{ib^{[1]}}{\rho+s} \\ & + a^{[3]}\left(\pi\delta(\rho-s)-\frac{i}{\rho-s}\right)+\frac{ib^{[3]}}{\rho+s}+\tau_{m,1}(\rho,s)+\mathrm{II}_{m,1}(\rho,s)\Bigg\},\end{aligned} \tag{E.42a}$$

$$\begin{aligned}\langle\psi_m(\rho),\phi_2(s)\rangle_{L^2} = \frac{1}{\sqrt{2\pi}}\Bigg\{ & \frac{ia^{[1]}}{\rho+s}+b^{[1]}\left(\pi\delta(\rho-s)-\frac{i}{\rho-s}\right) \\ & - \frac{ia^{[3]}}{\rho+s}+b^{[3]}\left(\pi\delta(\rho-s)+\frac{i}{\rho-s}\right)+\tau_{m,2}(\rho,s)+\mathrm{II}_{m,2}(\rho,s)\Bigg\}.\end{aligned} \tag{E.42b}$$

As stated above, $\langle\psi_m(\rho),\phi_l(s)\rangle_{L^2}$ is evaluated under ρ- and s-integrals, and therefore it is fruitful to collect the terms containing the Delta function, $\delta(\rho-s)$, and the terms not containing the Delta function, separately. That is, to express the overlap integral in the form:

$$\langle\psi_m(\rho),\phi_l(s)\rangle_{L^2} = G_{m,l}(\rho)\delta(\rho-s)+H_{m,l}(\rho,s), \tag{E.43}$$

where:

$$G_{m,1}(\rho) = \sqrt{\frac{\pi}{2}}\left(a^{[1]}+a^{[3]}\right), \tag{E.44a}$$

$$H_{m,1}(\rho,s) = \frac{1}{\sqrt{2\pi}}\left\{ i\left[\frac{a^{[1]}-a^{[3]}}{\rho-s}+\frac{b^{[3]}-b^{[1]}}{\rho+s}\right]+\tau_{m,1}(\rho,s)+\mathrm{II}_{m,1}(\rho,s)\right\}, \tag{E.44b}$$

$$G_{m,2}(\rho) = \sqrt{\frac{\pi}{2}}\left(b^{[1]}+b^{[3]}\right), \tag{E.44c}$$

$$H_{m,2}(\rho,s) = \frac{1}{\sqrt{2\pi}}\left\{ i\left[\frac{a^{[1]}-a^{[3]}}{\rho+s}+\frac{b^{[3]}-b^{[1]}}{\rho-s}\right]+\tau_{m,2}(\rho,s)+\mathrm{II}_{m,2}(\rho,s)\right\}. \tag{E.44d}$$

It should be noted that a defining feature of all inner products can be used to find the reversed inner product $\langle\phi_l(s),\psi_m(\rho)\rangle_{L^2}$ via the inner product $\langle\psi_m(\rho),\phi_l(s)\rangle_{L^2}$ [Christensen2, Definition 4.1.1]:

$$\langle\phi_l(s),\psi_m(\rho)\rangle_{L^2} = \langle\psi_m(\rho),\phi_l(s)\rangle^*_{L^2}. \tag{E.45}$$

E.4 Derivation of Fredholm Equation for Illumination by Radiation Mode

This appendix derives an integral equation for the aperture field at $z = 0$, $\Theta_{\hat{m}}(x, \hat{\rho})$, due to illumination by a radiation mode in the open geometry presented in Fig. 5.1. To arrive at this equation, the reflection and transmission coefficients, defined by the field expansions in Eqs. (5.9), are firstly expressed in terms of the aperture field.

The demand of continuity of the field at $z = 0$ gives the following equation:

$$\begin{aligned}&\psi_{\hat{m}}(x, \hat{\rho}) + \mathcal{R}_{1,\hat{m}}(\hat{\rho})U_1(x) + \sum_{m=1}^{2}\int_0^\infty \mathcal{R}_{m,\hat{m}}(\rho, \hat{\rho})\psi_m(x, \rho)\,\mathrm{d}\rho \\ &= \sum_{l=1}^{2}\int_0^\infty \mathcal{T}_{l,\hat{m}}(s, \hat{\rho})\phi_l(x, s)\,\mathrm{d}s = \Theta_{\hat{m}}(x, \hat{\rho}).\end{aligned} \tag{E.46}$$

The first and third members of Eq. (E.46) are multiplied by $U_1(x)^*$ and integrated over all x:

$$\begin{aligned}&\int_{-\infty}^{\infty}\psi_{\hat{m}}(x, \hat{\rho})U_1(x)^*\,\mathrm{d}x + \mathcal{R}_{1,\hat{m}}(\hat{\rho})\int_{-\infty}^{\infty}U_1(x)U_1(x)^*\,\mathrm{d}x \\ &+ \int_{-\infty}^{\infty}\sum_{m=1}^{2}\int_0^\infty \mathcal{R}_{m,\hat{m}}(\rho, \hat{\rho})\psi_m(x, \rho)\,\mathrm{d}\rho\, U_1(x)^*\,\mathrm{d}x = \int_{-\infty}^{\infty}\Theta_{\hat{m}}(x, \hat{\rho})U_1(x)^*\,\mathrm{d}x.\end{aligned} \tag{E.47}$$

Interchanging the order of integration and using the orthonormality relations in Eqs. (4.24a) and (4.24d) gives an expression for $\mathcal{R}_{1,\hat{m}}(\hat{\rho})$:

$$\mathcal{R}_{1,\hat{m}}(\hat{\rho}) = \int_{-\infty}^{\infty}\Theta_{\hat{m}}(x, \hat{\rho})U_1(x)^*\,\mathrm{d}x. \tag{E.48}$$

Multiplying next the first and third members of Eq. (E.46) with $\psi_k(x, \rho')^*$ and integrating over all x produces:

$$\begin{aligned}&\int_{-\infty}^{\infty}\psi_{\hat{m}}(x, \hat{\rho})\psi_k(x, \rho')^*\,\mathrm{d}x + \mathcal{R}_{1,\hat{m}}(\hat{\rho})\int_{-\infty}^{\infty}U_1(x)\psi_k(x, \rho')^*\,\mathrm{d}x \\ &+ \int_{-\infty}^{\infty}\sum_{m=1}^{2}\int_0^\infty \mathcal{R}_{m,\hat{m}}(\rho, \hat{\rho})\psi_m(x, \rho)\,\mathrm{d}\rho\,\psi_k(x, \rho')^*\,\mathrm{d}x = \int_{-\infty}^{\infty}\Theta_{\hat{m}}(x, \hat{\rho})\psi_k(x, \rho')^*\,\mathrm{d}x.\end{aligned} \tag{E.49}$$

Again, interchanging the order of integration and applying the orthogonality relations in Eqs. (4.24b) and (4.24d), allows simplification of the equation as follows:

$$\begin{aligned}\delta_{\hat{m}k}\delta(\hat{\rho} - \rho') + \mathcal{R}_{k,\hat{m}}(\rho', \hat{\rho}) &= \int_{-\infty}^{\infty}\Theta_{\hat{m}}(x, \hat{\rho})\psi_k(x, \rho')^*\,\mathrm{d}x \\ &\Updownarrow \\ \mathcal{R}_{k,\hat{m}}(\rho', \hat{\rho}) &= \int_{-\infty}^{\infty}\Theta_{\hat{m}}(x, \hat{\rho})\psi_k(x, \rho')^*\,\mathrm{d}x - \delta_{\hat{m}k}\delta(\hat{\rho} - \rho').\end{aligned} \tag{E.50}$$

Finally, the second and third members of Eq. (E.46) are multiplied with $\phi_k(x, s')^*$ and integrated over all x. The order of integration is changed, and using this and the

orthogonality relation in Eq. (4.24c) gives an expression for the transmission coefficients:

$$\mathcal{T}_{k,\hat{m}}(s',\hat{\rho}) = \int_{-\infty}^{\infty} \Theta_{\hat{m}}(x,\hat{\rho})\phi_k(x,s')^* \,\mathrm{d}x. \tag{E.51}$$

To derive an integral equation for $\Theta_{\hat{m}}(x,\hat{\rho})$, the demand of differentiability at $z=0$ is applied. To this end, it is assumed that integration with respect to z of the field expressions in Eqs. (5.9) can be carried out under the integrals:

$$\begin{aligned} &-\beta(\hat{\rho})\psi_{\hat{m}}(x,\hat{\rho}) + \beta_1\mathcal{R}_{1,\hat{m}}(\hat{\rho})U_1(x) + \sum_{m=1}^{2}\int_0^{\infty}\beta(\rho)\mathcal{R}_{m,\hat{m}}(\rho,\hat{\rho})\psi_m(x,\rho)\,\mathrm{d}\rho \\ &= -\sum_{l=1}^{2}\int_0^{\infty}\gamma(s)\mathcal{T}_{l,\hat{m}}(s,\hat{\rho})\phi_l(x,s)\,\mathrm{d}s. \end{aligned} \tag{E.52}$$

Insertion of the expressions for $\mathcal{R}_{1,\hat{m}}(\hat{\rho})$, $\mathcal{R}_{m,\hat{m}}(\rho,\hat{\rho})$, and $\mathcal{T}_{l,\hat{m}}(s,\hat{\rho})$ from Eqs. (E.48), (E.50) and (E.51), respectively, into Eq. (E.52) yields a Fredholm equation of the first kind:

$$\begin{aligned} 2\beta(\hat{\rho})\psi_{\hat{m}}(x,\hat{\rho}) = \int_{-\infty}^{\infty}\Theta_{\hat{m}}(x',\hat{\rho})\Bigg[&\beta_1 U_1(x)U_1(x')^* + \sum_{m=1}^{2}\int_0^{\infty}\beta(\rho)\psi_m(x,\rho)\psi_m(x',\rho)^*\,\mathrm{d}\rho \\ &+ \sum_{l=1}^{2}\int_0^{\infty}\gamma(s)\phi_l(x,s)\phi_l(x',s)^*\,\mathrm{d}s\Bigg]\,\mathrm{d}x, \end{aligned} \tag{E.53}$$

which may be expressed more compactly:

$$2\beta(\hat{\rho})\psi_{\hat{m}}(x,\hat{\rho}) = \int_{-\infty}^{\infty}\Theta_{\hat{m}}(x',\hat{\rho})\mathcal{K}_1(x,x')\,\mathrm{d}x, \tag{E.54}$$

with the kernel:

$$\begin{aligned} \mathcal{K}_1(x,x') = \beta_1 U_1(x)U_1(x')^* &+ \sum_{m=1}^{2}\int_0^{\infty}\beta(\rho)\psi_m(x,\rho)\psi_m(x',\rho)^*\,\mathrm{d}\rho \\ &+ \sum_{l=1}^{2}\int_0^{\infty}\gamma(s)\phi_l(x,s)\phi_l(x',s)^*\,\mathrm{d}s. \end{aligned} \tag{E.55}$$

To obtain a second order Fredholm equation, the following zero-identities, obtained using the completeness relations in Eqs. (4.24e) and (4.24f):

$$0 = k_0 n_1\left(\delta(x-x') - U_1(x)U_1(x)^* - \sum_{m=1}^{2}\int_0^{\infty}\psi_m(x,\rho)\psi_m(x',\rho)^*\,\mathrm{d}\rho\right), \tag{E.56a}$$

$$0 = k_0 n_0\left(\delta(x-x') - \sum_{l=1}^{2}\int_0^{\infty}\phi_l(x,s)\phi_l(x',s)^*\,\mathrm{d}s\right), \tag{E.56b}$$

are added to $\mathcal{K}_1(x,x')$, and manipulations of Eq. (E.54) then gives a second order Fredholm equation:

$$\Theta_{\hat{m}}(x,\hat{\rho}) = \Theta_{0,\hat{m}}(x,\hat{\rho}) + \lambda\int_{-\infty}^{\infty}\Theta_{\hat{m}}(x',\hat{\rho})\mathcal{K}(x,x')\,\mathrm{d}x', \tag{E.57}$$

where $\Theta_{0,\hat{m}}(x,\hat{\rho})$ and $\mathcal{K}(x,x')$ are defined in Eqs. (5.11).

E.5 Expressions for Reflection and Transmission Coefficients

In this appendix, expressions for the reflection coefficients for the radiation modes for illumination by the guided mode, $R^{(1)}(\rho)$, and for the reflection and transmission coefficients for illumination by a radiation mode, $\mathcal{R}_{1,\hat{m}}$, $\mathcal{R}_{m,\hat{m}}(\rho,\hat{\rho})$ and $\mathcal{T}_{l,\hat{m}}(s,\hat{\rho})$, introduced in Chapter 5, are derived using the expression for $\langle\psi_m(\rho),\phi_l(s)\rangle_{L^2}$, presented in Appendix E.3. This overlap integral can essentially be expressed on the form:

$$\langle\psi_m(\rho),\phi_l(s)\rangle_{L^2} = G_{m,l}(\rho)\delta(\rho-s) + H_{m,l}(\rho,s), \tag{E.58}$$

where $G_{m,l}(\rho)$ and $H_{m,l}(\rho,s)$ are defined in Eqs. (E.44).

Illumination by Fundamental Mode

Firstly, $R^{(1)}(\rho)$, given in Eq. (5.8b), is expressed in terms of the result in Eq. (E.58):

$$\begin{aligned} R^{(1)}(\rho) = & -c\sum_{l=1}^{2}\Bigg\{G_l(\rho)^*\left[\gamma(\rho)-k_0n_0\right]\langle U_1,\phi_l(\rho)\rangle_{L^2} \\ & + \int_0^\infty H_l(\rho,s)^*\left[\gamma(s)-k_0n_0\right]\langle U_1,\phi_l(s)\rangle_{L^2}\,\mathrm{d}s\Bigg\}, \end{aligned} \tag{E.59}$$

where the m-dependence of $G_{m,l}(\rho)$ and $H_{m,l}(\rho,s)$ has been omitted since $R_1^{(1)}(\rho) = R_2^{(1)}(\rho) = R^{(1)}(\rho)$.

Illumination by Radiation Mode

Using the expression in Eq. (E.58), the reflection and transmission coefficients for illumination by a radiation mode, see Eqs. (5.14), may be expressed as follows:

$$\begin{aligned} \mathcal{R}_{1,\hat{m}}^{(1)}(\hat{\rho}) = & -\mathcal{C}\sum_{l=1}^{2}\Bigg\{G_{\hat{m},l}(\hat{\rho})\langle\phi_l(\hat{\rho}),U_1\rangle_{L^2}(\gamma(\hat{\rho})-k_0n_0) \\ & + \int_0^\infty H_{\hat{m},l}(\hat{\rho},s)\langle\phi_l(s),U_1\rangle_{L^2}(\gamma(s)-k_0n_0)\,\mathrm{d}s\Bigg\}, \end{aligned} \tag{E.60a}$$

$$\begin{aligned} \mathcal{R}_{m,\hat{m}}^{(1)}(\rho,\hat{\rho}) = & \,\delta_{m\hat{m}}\delta(\rho-\hat{\rho})\left\{C[k_0(2n_1+n_0)-\beta(\hat{\rho})]-1\right\} \\ & -\mathcal{C}\sum_{l=1}^{2}\Bigg\{G_{\hat{m},l}(\hat{\rho})H_{m,l}(\rho,\hat{\rho})^*\left[\gamma(\hat{\rho})-k_0n_0\right] \\ & + G_{m,l}(\rho)^*H_{\hat{m},l}(\hat{\rho},\rho)\left[\gamma(\rho)-k_0n_0\right] \\ & + G_{\hat{m},l}(\hat{\rho})G_{m,l}(\rho)^*\delta(\rho-\hat{\rho})\left[\gamma(\hat{\rho})-k_0n_0\right] \\ & + \int_0^\infty H_{\hat{m},l}(\hat{\rho},s)H_{m,l}(\rho,s)^*\left[\gamma(s)-k_0n_0\right]\,\mathrm{d}s\Bigg\}, \end{aligned} \tag{E.60b}$$

$$\mathcal{T}_{l,\hat{m}}^{(1)}(s,\hat{\rho}) = \mathcal{C}\left[G_{\hat{m},l}(\hat{\rho})\delta(\hat{\rho}-s) + H_{\hat{m},l}(\hat{\rho},s)\right]\left[2k_0(n_0+n_1)-\beta(\hat{\rho})-\gamma(s)\right]. \tag{E.60c}$$

Bibliography

[Asmar] N. H. Asmar, *Partial Differential Equations with Fourier Series and Boundary Value Problems*, (Pearson Prentice Hall, Second Edition, 2005).

[Baker] C.T.H. Baker, *The numerical treatment of integral equations*, (Oxford University Press, First Edition, 1977).

[Bienstman] P. Bienstman, *Rigorous and efficient modelling of wavelength scale photonic components*, (Ph.D. thesis, Universiteit Gent, Department of Information Technology, 2001).

[Bransden] B.H. Bransden and C.J. Joachain, *Quantum Mechanics*, (Pearson Prentice Hall, Second Edition, 2000).

[Capsalis] C.N. Capsalis *et al.*, *Scattering from an Abruptly Terminated Dielectric-Slab Waveguide*, (Journal of Lightwave Technology, Vol. LT-3, No. 2, April 1985).

[Christensen1] O. Christensen, *Differentialligninger og uendelige rækker*, (DTU Mathematics, First Edition, June 2006).

[Christensen2] O. Christensen, *Functions, Spaces, and Expansions*, (DTU Mathematics, First Edition, January 2009).

[Claudon] J. Claudon *et al.*, *A highly efficient single-photon source based on a quantum dot in a photonic nanowire*, (Nature Photonics, Vol. 4, March 2010).

[Gregersen1] N. Gregersen, *Development of an electromagnetic field modeling tool*, (compendium from Niels Gregersen)

[Gregersen2] N. Gregersen *et al.*, *Numerical and Experimental Study of the Q factor of High Q-Micropillar Cavities*, (IEEE Journal of Quantum Electronics, accepted for publication).

[Gregersen3] N. Gregersen, *Optical Methods for Characterization of Surface Structures on a Nanometer Scale*, (Ph.D. thesis, Technical University of Denmark, COM DTU, 2006).

[Griffiths] D. J. Griffiths, *Introduction to Electrodynamics*, (Prentice Hall, Third Edition, 1999).

[Novotny] L. Novotny and B. Hecht, *Principles of Nano-Optics*, (Cambridge University Press, First Edition, 2006).

[Pedrotti] F.L. Pedrotti *et al.*, *Introduction to Optics*, (Pearson Prentice Hall, Third Edition, 2007).

[Purcell] E.M. Purcell, *Spontaneous Emission Probabilities at Radio Frequencies*, (Physical Review, Vol. 69, 1946).

[Reithmaier] J.P. Reithmaier *et al.*, *Strong coupling in a single quantum dot-semiconductor microcavity system*, (Nature, Vol. 432, 11 November 2004)

[Sammut] R.A. Sammut, *Orthogonality and normalization of radiation modes in dielectric waveguides*, (J. Opt. Soc. Am, Vol. 72, No. 10, October 1982).

[Schaums] M.R. Spiegel *et al.*, *Schaum's Outline of Mathematical Handbook of Formulas and Tables*, (McGraw-Hill, Third Edition, 2009).

[Snyder] H. W. Snyder and J. D. Love, *Optical Waveguide Theory*, (Kluwer Academic Publishers, First Edition, 1983).

[Tigelis] I.G. Tigelis and A.B. Manenkov, *Scattering from an abruptly terminated asymmetrical slab waveguide*, (J. Opt. Soc. Am. A, Vol. 16, No. 3, March 1999).

[Tocci] M.D. Tocci *et al.*, *Measurement of spontaneous-emission enhancement near the one-dimensional photonic band edge of semiconductor heterostructures*, (Physical Review A, Vol. 53, No. 4, April 1996).

[Vahala] K.J. Vahala, *Optical microcavities*, (Nature, Vol. 424, 14 August 2003).

[Vats] N. Vats *et al.*, *Theory of fluorescence in photonic crystals*, (Physical Review A, Vol. 65, March 2002).